

NVH Analysis Techniques for Design and Optimization of Hybrid and Electric Vehicles

Chapter 4

Numerical Approaches for the NVH study of Electric and Hybrid Electric vehicles

Paul Borza¹ and Sofia Sanchez Mateo²

¹Electronics and Computers Department, Transilvania University of Brasov, Politehnicii Street 1, Brasov 500024, Romania, borzapn@unitbv.ro,

²Mechanical Engineering and Energy Department, Miguel Hernandez University of Elche, Av de la Universidad, S/N - 03202, Elche, Spain, sofia.sanchez@graduado.umh.es,

Abstract. This chapter is dedicated to an overview of models and methodologies used for the numerical analysis of noise, vibration, and harshness of the mechanical systems, with a focus to EV's. After a short general introduction, the annexed sections compile relevant studies performed at TU1105 partner organisations with the aim to show some relevant and high-potential recent developments in the field.

1 Introduction

Noise, Vibration & Harshness (NVH) describes the dynamic behaviour of vehicles in the whole frequency range. It comprises the sensible low frequency vibrations of structures, the sensible and audible range of perceived acoustical comfort (harshness), as well as the audible high frequency range of noise limited by the perception ability of the human ear (20 Hz – 20000 kHz).

Due to the complexity of the NVH attribute, typically automotive engineers rely on the use of numerical models for NVH analysis and design. The most widely used numerical methods are the Finite Element Method (FEM) and the Boundary Element Method (BEM). Both of them can be used for structural and acoustic analysis but typically, FEM is used for structural and bounded acoustic problems whereas BEM is used for (unbounded) acoustical problems. They are mainly applicable for low frequency analysis. For high-frequency analysis, other methodologies such as Statistical Energy Analysis is often used. To analyse low-frequency mechanical motion of vehicle systems (such as suspensions), other time-domain integration based schemes such as Multi-Body analysis or 1D System Simulation can be deployed.

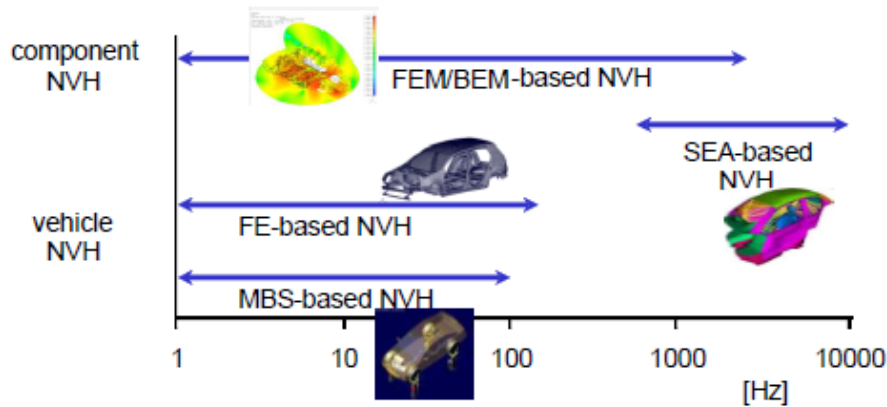


Fig. 1. Simulation methods and their application range **Erreur ! Source du renvoi introuvable.**

2 Methodologies and numerical contributions to the study of EVs

According to the objective of this chapter, several issues related to NVH numerical methods have been studied and analysed in detail. If we look how these methods find their application in the various challenges related to the NVH behaviour of (H)EV, the Source-Transfer-Receiver approach, well known from experimental analysis, modelling and refinement, can be adopted as well to identify and address the numerical modelling challenges [2].

Fig. 2 shows the main topics of this chapter. Each input is presented as an individual annex, according to the following structure:

- 4A. Vibro-acoustic metamaterial developments combining low-mass structural solutions with high vibro-acoustic insulation performance.
- 4B. Development of equations of motion based on Lagrange formulation, applied for the modal analysis of mechanical systems.
- 4C. Using of BEM simulation approaches for sound field prediction of EVs and alerting systems.
- 4D. Equivalent material modelling of sandwich beam assemblies: propagating and evanescent wave considerations.
- 4E. Modelling the NVH and thermal behaviour of electric motors using a combination of electromagnetic FEM, 1D system simulation, structural FEM and Acoustic BEM.

4F. Using FEM and BEM methods to design an optimal warning sound system to protect Vulnerable Road Users.

4G. Using FEM material modelling for the vibrational analysis of inertial dampers of EVs, application to damage detection using experimental modal identification

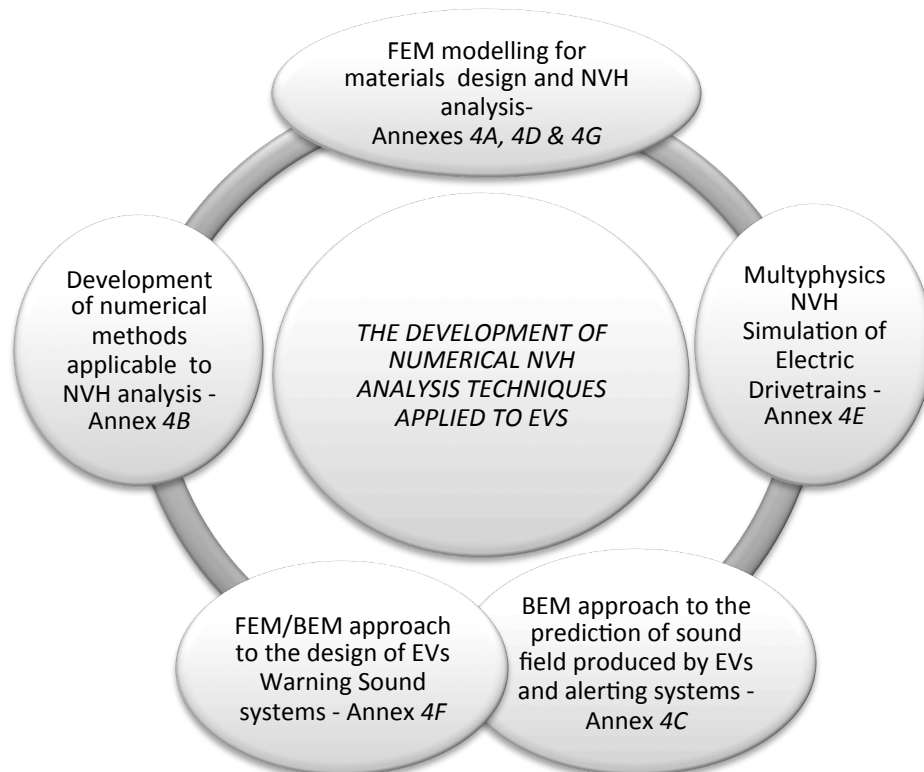


Fig.2. Main aspects of the numerical NVH study of Electric and Hybrid Electric Vehicles

3 Conclusions

Some important achievements have been presented in this chapter, as well as suggestions for future work. Concerning the contributions compiled and related to experimental approaches for the NVH analysis of EVs and HEVs, the main conclusions are:

- With the constant quest towards low mass vehicles, the need arises to develop and model lightweight materials and structures with enhanced NVH behaviour. *Annex 4A* discusses the developments regarding acoustic resonant metamaterials at KU

Leuven [3, 4]. By exploiting inherent dynamic properties of integrated material resonating elements, vibro-acoustic stopband behaviour can be created at low frequencies. This allows to combine lightweight solutions with good NVH properties and opens up possibilities to create dedicated solutions for a.o. electrified vehicles to contain and shape noise and vibration patterns.

- *Annex 4B* shows a numerical formulation based on Lagrange equations, useful for an optimized finite element analysis of vibration.
- *Annex 4C* addressed the potential of BEM for the prediction of the sound field generated by EVs and HVs and integrated alerting systems (AVAS) in an urban environment.
- *Annex 4D* studies the dynamic behaviour of a sandwich laminate structure. On the basis of a practical example, the equivalent loss factor was defined and applied to the equivalent material.
- The multiphysics simulation methodology presented in *Annex 4E* has been applied to the specific problem of an SRM (Switched Reluctance Motor). More detailed discussions can be found in [5 - 7]. Further refinement of the method, a better integration with the EMC simulations and a validation of experimental test cases is ongoing.
- The warning sound approach discussed in *Annex 4F* fits into the broader discussion of protecting vulnerable road users against low-speed incidents by electric Vehicles appearing unadvertedly. The FEM/BEM approach to validate the loudspeaker configuration is discussed here. The actual definition and generation of the sound and the pedestrian detection system are discussed elsewhere. [8 - 10].
- *Annex 4G* uses FEM for modelling the behaviour of composite materials that inertial dampers are made of. Vibrational analysis of such models, combined with experimental modal identification, is applied for damage detection.

4 References

- [1] Bierman, J. W., NVH Calculation Technologies, ika, Aachen University, e-COST TU 1105, Training School in Liege (2015)
- [2] H. Van der Auweraer, K. Janssens, A Source-Transfer-Receiver Approach to NVH Engineering of Hybrid/Electric Vehicles. SAE paper 2012-36-0646, Proc. SAE NVH Brazil, Florianopolis, Brazil, 2012
- [3] C. Claeys, B. Pluymers, P. Sas, W. Desmet. Design of a resonant metamaterial based acoustic enclosure. ISMA2014 - USD2014. Leuven, Belgium, 15-17 September 2014 (art.nr. 561) (pp. 3351-3358).
- [4] C. Claeys, E. Deckers, B. Pluymers, and W. Desmet, A lightweight vibro-acoustic metamaterial demonstrator: Numerical and experimental investigation, *Mechanical Systems and Signal* (2016), 70-71, 904-918.
- [5] J. Anthonis, F. Santos, V. Croitorescu, H. Van der Auweraer, "Multiscale Thermal and NVH Models for EV/HEV Integration of an SR-based Drivetrain", *Virtual Powertrain Conference*, Oct. 19-20, 2011, Pune, India

- [6] F.L.M. Dos Santos, J. Anthonis, F. Naclerio, J.J.C. Gyselinck, H. Van der Auweraer, and L.C.S. Goes, Multiphysics NVH Modeling: Simulation of a Switched Reluctance Motor for an Electric Vehicle, *IEEE Transactions on Industrial Electronics*, 61-1(2014), 469–76.
- [7] C.T. Faria, F.L.M. Dos Santos, F. Chauvicourt, S. Orlando: Noise emissions on switched reluctance motors: evaluation of different structural models, *Proceedings of EVS28*, Kintex, Korea, 2015
- [8] J. J. García , J. M. Barrios , D. Quinn , G. Baudet , T. Schmit , J. Chamard, “The expected impact of eVADER technology on the safety of vulnerable road users”, *Proc. ISMA 2014, Noise and Vibration Conference* (Leuven, Belgium, 15-17 September 2014
- [9] H. Van der Auweraer, D. Sabbatini, E. Sana, K. Janssens, “Analysis of Electric Vehicle Noise in View of VRU Safety”, in *Proceedings ICSV18*, Brazil, 10-14 July 2011
- [10] Van Genechten B., Vansant K. & Berkhoff A.P., Simulation-based design of a steerable acoustic warning device to increase (H)EV detectability while reducing urban noise pollution In *Proceedings of the TRA 2014*, Paris, France, 14-17 April 2014

Annex 4A

Design and validation of a metamaterial acoustic enclosure

Claus Claeys¹, Elke Deckers, Lucas Van Belle, Alireza Nateghi, Noé F. Melo, Luca Sangiuliano, Bert Pluymers and Wim Desmet

¹Dept. of Mechanical Engineering, KU Leuven, Belgium, claus.claeys@kuleuven.be

Abstract. Periodic structures, such as honeycomb core panels, combine excellent mechanical properties with a low mass, making them attractive for application in transport and machine design. However, the high stiffness to mass ratio of these lightweight panels may result in unsatisfactory dynamic behaviour in that it may impair the panels' ability to reduce noise and vibration levels.

Liu et al. demonstrated that inclusions of high density spheres with a rubber coating in a matrix material result in low frequency sound isolation breaking the mass law [1]. These locally resonant metamaterials require a high density of local resonators throughout the matrix material, either spread randomly or periodically.

This chapter describes a novel metamaterial concept based on sandwich structures with embedded resonant structures that exhibit vibro-acoustic stopband behaviour. A metamaterial encapsulation is designed and produced to showcase the potential of this type of metamaterials to improve acoustic insulation performance in targeted frequency ranges. As compared to classic encapsulations made from homogeneous panels, the acoustic insertion loss from the metamaterial is strongly increased within the stop band region of the metamaterial without increasing the mass and hardly increasing the volume

4A.1 Introduction

Increasing customer expectations and more restrictive legal requirements turn the acoustical behaviour of products into an important design criterion in the machine and transportation industry as well as in the construction and consumer goods sector. Ecological trends and the associated run for efficiency, however, increase the importance of lightweight design and reduce the applicability of classical (heavy) solutions to improve acoustic behaviour. In view of this challenging and often conflicting task of merging acoustical and lightweight requirements novel acoustic solutions are required. Ideally these novel solutions are easy to design and are characterised by a low mass and compact volume along with a high reliability at an affordable cost.

Vibro-acoustic metamaterials come to the fore as possible candidates for lightweight material systems with superior noise and vibration insulation, be it at least in some targeted and tuneable frequency ranges, referred to as stop bands. Contrary to photonic crystals, stop bands in metamaterials don't rely on periodicity or Bragg scattering and work on spatial scales much smaller than the wavelength [2]. The stop bands induced in metamaterials result from resonant cells arranged on a

subwavelength scale and can be described based on the Fano-type interference between incoming waves and the waves re-radiated by the resonant cells [3, 4]. Previous papers of the authors explain the working principles of stop bands based on resonant metamaterials and list the driving parameters for stop band design [5].

In this chapter an innovative metamaterial concept to improve acoustic behaviour is proposed; resonant structures are added to cavities of a periodic core sandwich structure to create stop band behaviour. The next section describes the rationale behind the proposed metamaterial concept, followed by a section describing the numerical prediction of the stop band behaviour of this concept. The following sections elaborate on the demonstrator design, measurements on this demonstrator and the validation with numerical simulations. The chapter ends with the conclusions.

4A.2 Metamaterial creation by inclusion of resonant structures

Metamaterials with stopband behaviour are obtained through the inclusion of resonant cells on a scale smaller than the structural wavelengths to be influenced [5]. Stop band behaviour can thus be achieved through the introduction of any system that introduces local resonant behaviour.

In view of applications, the goal is to find resonant systems which do not jeopardise other requirements; structural integrity, light weight, use in contaminated environment, fire-resistance... The kinds of resonant systems which are eligible heavily depend on the structure to which the resonant systems have to be added.

Inspiration for a high potential structure to introduce stop band behaviour is sought in the class of periodic lightweight structures, such as honeycomb core sandwich panels. They are becoming attractive for application in transport and machine design due to the combination of excellent mechanical properties with a low mass.

Fig. 1-A shows examples of sandwich structures; a core acts as spacer to create distance between the skins such that a light structure with excellent stiffness properties in bending is obtained. The core has as main role to create distance between the skins as well as to resist forces perpendicular to the structure while the skin is designed to show a high in plane strength; given the different requirements for both, often the skin is made of a different material as the core. Different core layouts are possible and two typical layouts are hexagonal or rectangular cores.

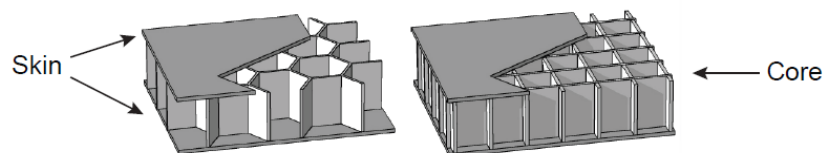


Fig. 1-A: Examples of sandwich structures; left a hexagonal core, right a rectangular core [6]

The internal cavities of these periodic core sandwich panels are an ideal host structure to include resonant systems. In such configuration the resonant systems can be freely designed for optimal acoustic behaviour in a targeted frequency zone while safeguarding the excellent mechanical properties of the sandwich panels. The only requirement for the resonant structures is the presence of a resonance mode; a huge number of designs could be proposed, leaving room for optimisation towards e.g. minimal weight, maximal attenuation or broadband attenuation.

For this investigation a straight forward design is chosen that resembles a mass-spring system; two thin legs are used to connect a heavy mass to a host structure (Fig. 2-A). The connection legs will determine the stiffness while the thick part of the resonator will determine the mass of this resonant structure.

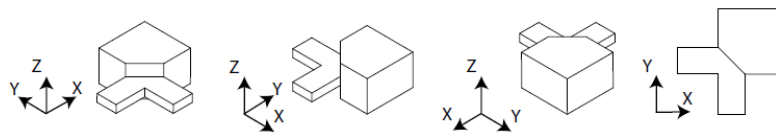


Fig. 2-A: Resonant structure used in this project to introduce stop band behaviour

Adding the resonant structures to the cavities of a periodic sandwich core (Fig. 3-A) will introduce a stop band, and thus improved acoustic behaviour, for frequencies in the vicinity of the resonance frequency of the resonant structure. Further analyses of how the resonant structures introduce stop band behaviour, is the topic of next section.

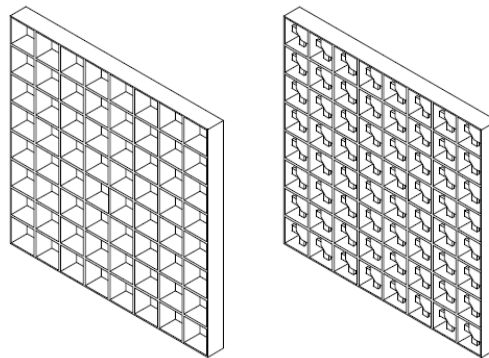


Fig. 3-A: Rectangular core without (left) and with (right) resonant structures

4A.3 Stop band prediction

From literature it is known that wave propagation through infinite periodic structures can be investigated through unit cell modelling [7] [8]. Based on an undamped Finite Element (FE) model of the unit cell and the application of periodicity boundary conditions, dispersion curves for freely propagating waves in an infinite periodic

structure can be derived. Frequency zones, for which no solutions are found, correspond to frequency zones without free wave propagation and thus a stop band region.

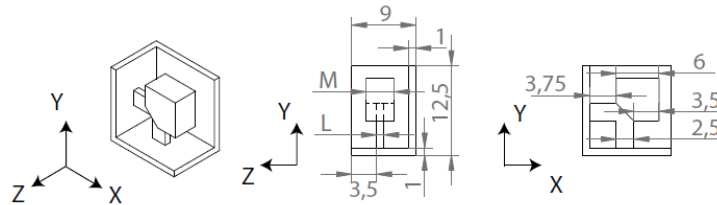


Fig. 4-A: Dimensions in millimeter of the unit cell of the enclosure. The resonator leg thickness (L) equals 1 mm, the resonator mass (M) equals 4 mm

Fig. 4-A shows the geometry of the unit cell that will be used to build a demonstrator. The resonant structure makes up 30% of the weight of the unit cell. Fig. 5-A depicts the FE model of this unit cell. Linear Quad4 elements are used to represent the resonant structure, core and skin. The resonator mass has a larger thickness than the connection legs; different properties are assigned to both element groups. The resonator mass element group is depicted in grey on the right side of Fig. 5-A.

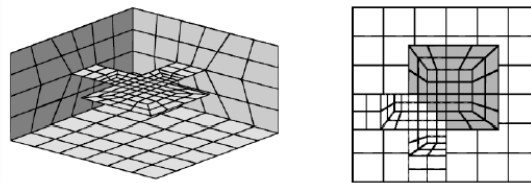


Fig. 5-A: FE model of the unit cell of the demonstrator. The grey elements in the top view (right) represent the resonator mass

Table 1-A: Material characteristics of the material of the unit cell in the numerical simulations

Name	Symbol	Value
Young's modulus	E	1.65 Mpa
Density	ρ	950 kg/m ³
Poisson's ratio	ν	0.4

The material characteristics of the acoustic enclosures are given in Table 1-A. The enclosures are made through Selective Laser Sintering (SLS) of Polyamide, the material and production characteristics are discussed in more detail in next section.

Since the main goal of the simulations is to get an indication whether stop band behaviour is present rather than obtaining a detailed model, isotropy and linear behaviour of the material are assumed.

The resonant structure is designed to have a pronounced low frequent bending mode followed by subsequent modes higher in frequency. Fig. 6-A shows the first two modes of the free unit cell which can be related to modes of the resonant structure. Left the bending mode is shown which occurs at a frequency of 1272 Hz, the next mode, shown at the right, occurs at 5052 Hz; this large shift in frequency between the modes allows to correlate stop band behaviour with a certain resonance mode. Convergence of the model was validated against a refined unit cell model of 6766 nodes and 6576 elements. The used model with 198 nodes and 168 elements has an accuracy of 1 % on the first mode and 1.5 % on the second mode.

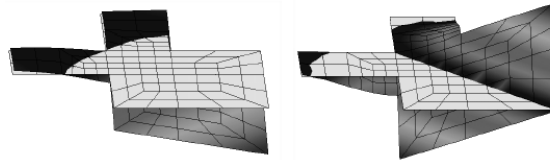


Fig. 6-A: Undeformed mesh (light) and the deformation of the first modes (dark) of the resonant structures. Left: bending mode at 1272 Hz. Right: torsional mode at 5052 Hz

The unit cell allows derivation of the dispersion curves of the demonstrator. Fig. 7-A shows the bending wave dispersion curves for the unit cell of the demonstrator in comparison to the dispersion curves of the host structure without resonant structures. The dispersion curves are similar except for a region around the resonance frequency of the resonant system for which no dispersion curves exists; a stop band opens up from 1065 Hz up to 1226 Hz. The shift with respect to the resonance frequency of the resonant structure (1272 Hz), is explained by the different boundary conditions of the unit cell during calculation of the resonance frequency.

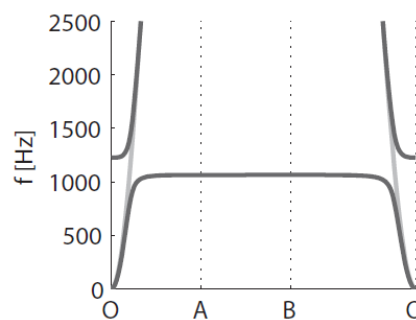


Fig. 7-A: Dispersion curves of the demonstrator (—) in comparison with the dispersion curves of the host structure (---)

4A.4 Demonstrator Example

To prove the potential of the introduced metamaterials concept to reduce acoustic transmission, an acoustic enclosure making use of resonant structures is designed. A variety of demonstrators can be thought of to determine the acoustic transmission characteristics of a material. In the choice for a suitable demonstrator, some determining factors are: unambiguous proof of concept, quantifiable effect and engineering relevance. To obtain an unambiguous proof of concept it is crucial to have as less unknown effects in the design as possible. Connections between different components by bolts or combining parts together by glueing, is a likely source of uncertainty; it is preferred to have a demonstrator built in one part such that these unknowns are reduced. It was chosen to design acoustic enclosures as boxes with one open side which can be placed over a small speaker. The acoustic transmission loss is then determined by comparing sound radiation with and without enclosure.

Producing acoustic enclosures in one part is hard to achieve with traditional manufacturing processes. Additive manufacturing is a production process which allows producing complex parts without the need of an expensive mould, making it a suitable production process for prototype design. Within the range of additive manufacturing processes, Selective Laser Sintering (SLS) is chosen to create the demonstrator. SLS is an additive manufacturing method where small powder particles are melted together by means of a laser. The melting of adjacent material particles is called sintering and by controlling the laser, a pattern can be sintered in a layer of material powder. Unlike other additive manufacturing methods, such as fused deposition modelling and stereolithography, the part being built is surrounded by unsintered powder at all times. This unsintered powder acts as a support for the next layers and facilitates building complex parts with jumps in geometry across the height of the part. This possibility of building complex parts is the main reason why SLS was chosen as production process.

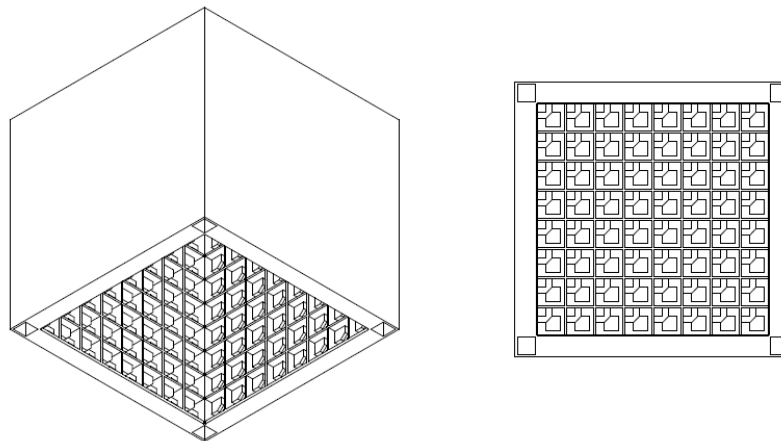


Fig. 8-A: Demonstrator design; side (left) and bottom (right) view

Fig. 8-A shows a side and bottom view of the demonstrator design. One side of the enclosure contains 8 x 8 unit cells. It should be noted that the corners of the demonstrator are hollow and no resonators are added. The size of the enclosure is a balance between obtaining a light demonstrator and still being relevant; the enclosure is designed such that the inner dimensions make up a cube of 100 x 100 x 100 mm. Fig. 9-A shows a produced version of this demonstrator.

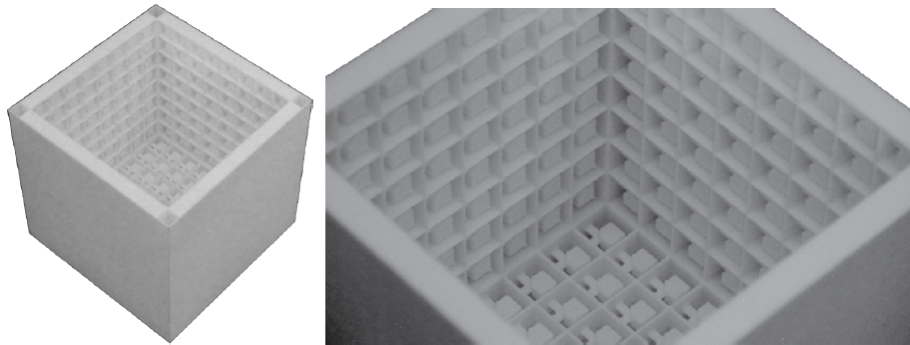


Fig. 9-A: Pictures of the demonstrator

4A.5 Measurement results

The test set-up consists of a small loudspeaker placed on a wooden plate (Fig. 10-A). The wooden plate is placed on an iron support in the centre of a semi-anechoic chamber. Between the wooden plate and the loudspeaker, a small trim-like piece of fabric is placed; the trim covers the cable of the loudspeaker which runs in a small split in the plate.

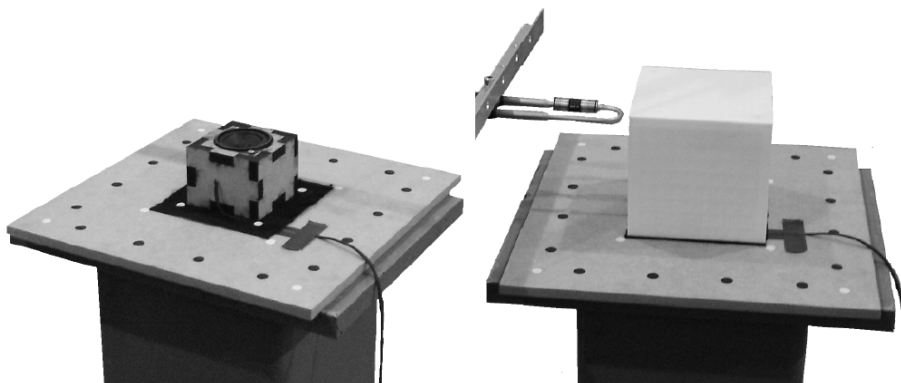


Fig. 10-A: Picture of the test set up (left) and an intensity measurement of an acoustic metamaterial enclosure on the test set up (right)

The sound power is evaluated on the surface of a surrounding box of 250 x 250 x 190 mm centred on the loudspeaker; the black dots on the wooden plate (Fig. 10-A) indicate the width and length of the surrounding box. The acoustic power is evaluated based on 5 intensity measurements, one on each side of the box, with a scanning intensity probe.

The insertion loss is defined as:

$$Insertion\ Loss = 10 \log_{10} \left(\frac{P_{without}}{P_{with}} \right) \quad \text{Eq. 1 - B}$$

where $P_{without}$ is the radiated acoustic power radiated through the imaginary evaluation box when the enclosure is not in place and P_{with} is the radiated acoustic power when the enclosure is in place. The use of insertion loss as metric has as added value that the results are not dependent on source spectrum.

Fig. 11-A compares the measured insertion loss of the metamaterial demonstrator to the measured insertion loss of a regular enclosure with the same mass but build from flat panels of 3.5 mm thickness. Between 700 and 1000 Hz the demonstrator enclosure clearly outperforms the regular enclosure. The frequency zone of improved acoustic behaviour is a bit lower in frequency than the stop band predicted by the design of the resonant structures.

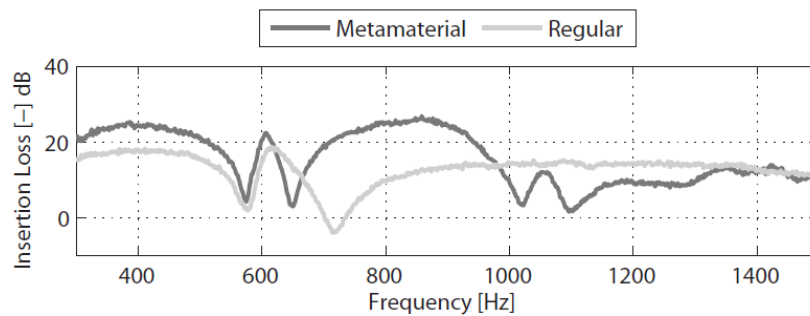


Fig. 11-A: Comparison between the measured insertion loss for the metamaterial demonstrator and a demonstrator with flat side panels and an equivalent weight to the metamaterial demonstrator.

Further investigation of the produced demonstrator explains the shift in frequency; through optical measurements of dedicated test samples of the demonstrator unit cell on a CNC Mitutoyo QuickVision Pro - 202 machine it was shown that the average geometry is smaller than the nominal geometry [6][9]. This shift in geometry should be taken into account in the numerical model; the shift from the nominal 1 and 4 mm to the measured 0.83 and 3.85 mm thickness for the connecting leg and resonator mass respectively leads to a shift in stop band frequencies from 1065 – 1226 Hz to 861 – 986 Hz, corresponding well with the measures zone of increased acoustic insertion loss.

4B.6 Comparison with numerical models of the finite enclosure

To validate the measurement results a numerical counterpart is built for the test set-up and the acoustic enclosure.

4B.6.1 Model of the test set-up

The wooden plate is modelled as a baffle: an infinite plane which is acoustically perfectly reflecting. The model is shown in Fig. 12-A. This approach is justified since the acoustic power is measured above the wooden plate and the set-up is positioned within a semi-anechoic chamber. An impedance layer in the plane of the baffle reflects the piece of trim on the wooden plate; a real impedance of $1.578 \cdot 10^4 \text{ kg/m}^2$ corresponding to a sound absorbing coefficient of 0.1 is added [10]. The piece of trim has a size similar to the size of the acoustic enclosure. The impedance layer in the numerical model covers the part of the baffle between the model of the loudspeaker and the enclosure.

The loudspeaker is modelled as a rigid perfectly reflecting box with the same dimension as the loudspeaker: $73 \times 73 \times 55 \text{ mm}$. The speaker mesh and the impedance boundary have a maximal element length of 10 mm. Following the 6 elements per wavelength rule, this mesh is acoustically valid up to above 5000 Hz.

To model the sound source the a point source is used. The point source emits a constant intensity across the frequency spectrum and is placed 5 mm above the centre of the upper plane of the speaker. The upper surface of the speaker mesh is refined since the point source is placed close to this surface. As explained in last section, insertion loss is used as acoustic characteristic for the enclosures, which should be independent of source spectrum.

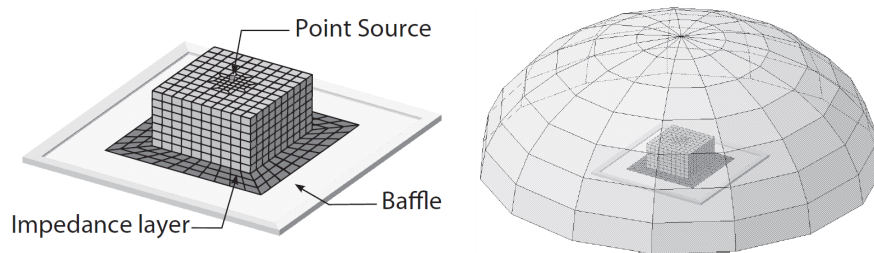


Fig. 12-A: Left: model of the test set-up. Right: Mesh on a hemisphere with a 0.3 m radius around the model of the loudspeaker to evaluate the radiated acoustic power in the numerical model.

The numerically predicted radiated acoustic power is calculated as the sum of the radiated acoustic intensity on a hemisphere with a 0.3 m radius which is centred over the loudspeaker. Fig. 12-A, depicts the mesh, consisting of 105 elements and 113 nodes with a largest element edge equal to 0.1m. This mesh was validated by comparison with refined meshes for the evaluation of the acoustic radiated power.

4B.6.2 Model of the acoustic enclosure

To compute the acoustic radiated power through the enclosure under excitation of the point source within the enclosure a simulation is required in which an acoustic model of the test set-up is coupled to a vibro-acoustic model of the enclosure. To reduce computational cost, a modal-based vibro-acoustic coupling is applied; the structural modes of the enclosure are derived for a detailed structural FE mesh after which these structural modes are projected on an acoustic Boundary Element (BE) mesh of the enclosure such that a coupled vibro-acoustic simulation can be performed. These calculations are performed in the LMS VL.Acoustics software environment coupled to a Nastran structural solver and a Sysnoise acoustical solver.

The FE model of the structure is derived through a repetition of the unit cell described in section 3 of this article. Fig. 13-A shows the FE model of the acoustic enclosure without outer skin. The total structural model with outer skin contains 63353 nodes and 60720 linear Quad4 elements.

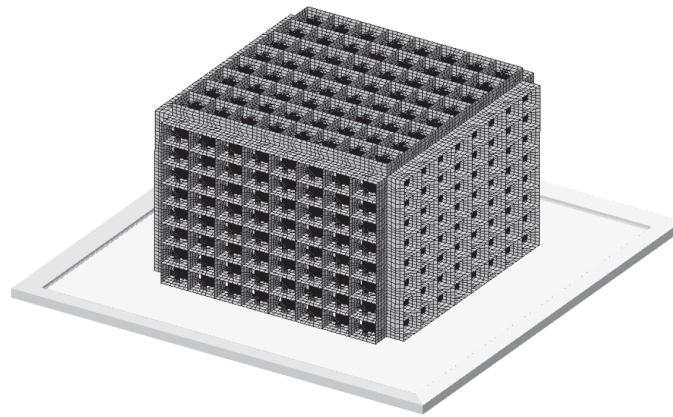


Fig. 13-A: Structural FE model of the acoustic enclosure with the outer skin not shown.

The element size of the structural mesh of the enclosure is driven by the smallest geometry of the unit cell. This geometry is small compared to the wavelength in the structure since the inclusion for metamaterial based stop bands needs to be smaller than the governing wavelength in the structure.

The enclosure is supported by the wooden plate and the piece of trim. This is modelled by removing the translational degrees of freedom of all elements in the bottom plane of the enclosure. The motion parallel to the wooden plate is influenced by the boundary as well; this is neglected in the numerical model. To include the effect of damping both in the material as through the boundary, 1% of modal damping is applied to all the modes.

The minimal size of the acoustic mesh is driven by the wavelength of sound in air. Since the simulations are below coincidence, the element size requirements on the acoustic mesh are less stringent than for the structural mesh. The acoustic mesh is

built as a remeshing of the skin of the enclosure with 15 x15 elements on each side such that the obtained element length is similar to the model of the loudspeaker. This remeshing reduces the number of elements for the outer skin from 4140 for the structural model to 1125 elements for the acoustic model. Fig. 14-A compares the obtained acoustic mesh (right) with the structural mesh (left).

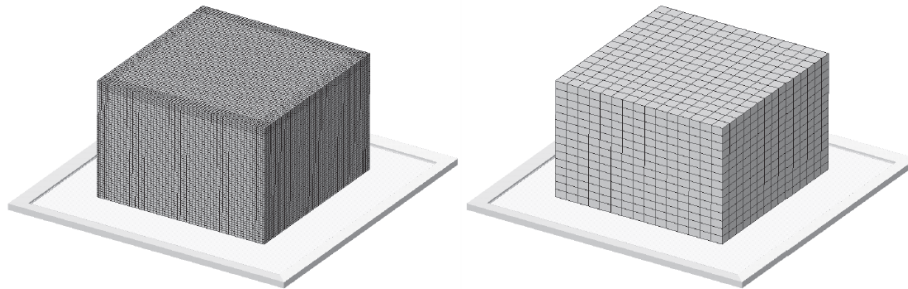


Fig. 14-A: The structural model of the enclosure with skin shown (left) and the acoustic model (right).

To compute the acoustic radiated power through the enclosure a BE modal-based vibro-acoustic coupling is applied. This coupling requires the mode shapes, computed for the structural model, shown in Fig. 14-A and on the left of Fig. 14-A, to be mapped onto the acoustic mesh. The equivalent displacement on a node of the acoustic mesh is calculated based on the movement of the 20 closest nodes on the skin of the structural mesh which are within a 5.5 mm radius of the node on the acoustic mesh. The contributions of these nodes of the structural mesh to the node on the acoustic mesh are weighted based on the distance between the nodes on structural and acoustic mesh.

The mapping of the modes of a structural model with skin, core and resonant structures on an acoustic mesh without core and resonant structures means that the resonant structures cannot be influenced by the acoustic medium in the simulation and the other way around, that the movement of the resonant structures will not influence the acoustic medium. This simplification was validated by comparing the obtained results with this strategy to a simulation using the full structural mesh (skin, core and resonant structure) as acoustic mesh: every node of the structural model coincided with a node on the acoustic model. The difference showed to be negligible, indicating that the mesh mapping is allowed and that the acoustic mesh size is fine enough.

This validation of the mesh mapping indicates that the surrounding air does not influence the motion of the resonators in the numerical model. In reality however, the relative motion of the resonant structure with respect to the host structure could lead to added damping by air being squeezed through the gap between resonant structure and core. The acoustic model applied does not account for possible viscosity effects.

4B.6.3 Validation results

A numerical simulation of the demonstrator with this geometry of the resonator updated according to the measurements shows a good predicted insertion loss (Fig. 15-A). Details on the numerical model used can be found in [6] [11]. The depth of the stop band is overestimated in the simulations, but this might be related to a wrong estimation of the amount of damping in the material as well as due small variation in the resonance frequencies of the resonant structures; both the damping as a spread on the resonance frequencies can have a strong effect on strength of acoustic reduction in the stop zone [5] [6].

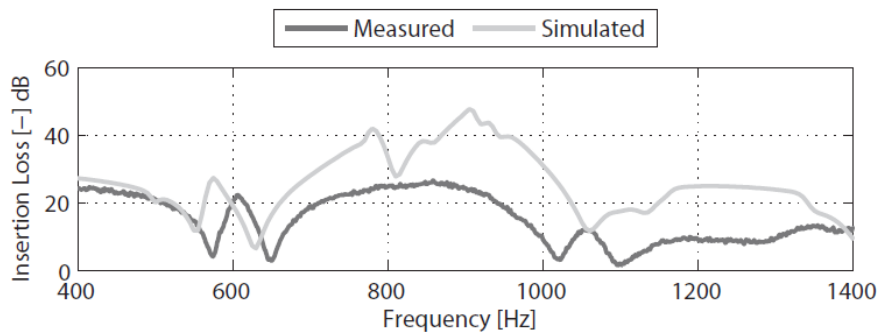


Fig. 15-A: Comparison between measured and numerically predicted insertion loss of the metamaterial demonstrator. The geometry of the resonant structures was updated to comply with measurements results on the geometry of a unit cell.

4B.7 Conclusions

This section introduces a novel method to create resonant metamaterials for acoustic insulation; the inclusion of resonant structures within the core of a sandwich structure. Through the numerical and experimental validation of a demonstrator it is shown that this results in a frequency zone of increased acoustic insertion loss with respect to equivalent materials of the same weight. Unit cell modelling allows a quick estimation of the location of the stop band frequencies and can be used as a tool to assess changes in resonant structure design. This metamaterial concept allows the combination of light weight, compact mass and good acoustic behaviour along with other technological benefits such as integration in structural parts, use in harsh environments and easy designable beneficial frequency ranges. To see and hear this potential in a movie, the interested reader is referred to a movie which can be seen on the following link (http://youtu.be/tOch_GsGaXg).

Acknowledgements

The authors would like to acknowledge the European Commission for their support through the ENLIGHT-project (<http://www.project-enlight.eu/>) and the EMVeM-project (<http://www.emvem.org/>) and the KU Leuven Research Fund for their support through the IOF. E. Deckers and L. Van Belle are respectively a postdoctoral and doctoral fellow of the Fund for Scientific Research Flanders (F.W.O.). This Fund is also gratefully acknowledged for its support in the G.0371.12 research project. The research of N. F. Melo is funded by a PhD Scholarship Sciences without Borders CNPq Brazil (201414/2014-7).

4B.8 References

- [1] Z. Liu, X. Zhang, Y. Mao, YY Zhu, Z. Yang, CT Chan, and P. Sheng, Locally resonant sonic materials, *Science* 289 (2000), no. 5485, 1734–1736.
- [2] J B. Pendry, D.J. Holden, A J.and Robbins, and W.J. Stewart, Magnetism from conductors and enhanced nonlinear phenomena, *Microwave Theory and Techniques, IEEE Transactions on* 47 (1999), no. 11, 2075–2084.
- [3] C. Goffaux, J. S'anchez-Dehesa, A.L. Yeyati, P. Lambin, A. Khelif, JO Vasseur, and B. Djafari-Rouhani, Evidence of fano-like interference phenomena in locally resonant materials, *Physical Review Letters* 88 (2002), no. 22, 225502.
- [4] F. Lemoult, N. Kaina, M. Fink, and G. Lerosey, Wave propagation control at the deep subwavelength scale in metamaterials, *Nature Physics* 9 (2012), 55–60.
- [5] C. Claeys, K. Vergote, P. Sas, and W. Desmet, On the potential of tuned resonators to obtain low frequency vibrational stop bands in periodic panels, *Journal of Sound and Vibration* 332 (2013), no. 6, 1418–1436.
- [6] C. Claeys, Design and analysis of resonant metamaterials for acoustic insulation, PhD Thesis, KU Leuven, 2014.
- [7] L. Brillouin, Wave propagation in periodic structures, 2nd ed., McGraw-Hill Book Company, 1946.
- [8] R.S. Langley, A note on the force boundary conditions for two-dimensional periodic structures with corner freedoms, *Journal of Sound and Vibration* 167 (1993), 377–381.
- [9] C. Claeys, B. Pluymers, P. Sas, W. Desmet. Design of a resonant metamaterial based acoustic enclosure. ISMA2014 - USD2014. Leuven, Belgium, 15-17 September 2014 (art.nr. 561) (pp. 3351-3358).
- [10] Vivolo, M., Vibro-acoustic characterization of lightweight panels by using a small cabin, Ph.D. thesis, KU Leuven, Departement Werktuigkunde, 2013.
- [11] C. Claeys, E. Deckers, B. Pluymers, and W. Desmet, A lightweight vibro-acoustic metamaterial demonstrator: Numerical and experimental investigation, *Mechanical Systems and Signal* (2016), 70-71, 904-918.

Annex 4B

Motion equations of mechanical systems used in common engineering applications

Sorin VLASE¹

¹Dept. of Mechanical Engineering, Transilvania University of Brasov, Romania
svlase@unitbv.ro

4B.1 Motion equations of an one-dimensional finite element

4B.1.1 General considerations

In what follows the motion equations governing the evolution in time of a truss finite element, participating along with the body to the general rigid body motion of the system are being determined [1-7]. In the presentations important parts represent the author's contribution to the development of this field [8-19]. Different applications are presented in [20-29].

The method used will be the method of Lagrange equations. In order to be able to use this method, the kinetic energy of the considered finite element, the internal energy and the work of the distributed and concentrated loads (for obtaining the Lagrangian) will be calculated.

An application of the method is presented in [30]. Experimental results are obtained by [31] and [32]. Mathematical methods to solve the obtained equations are presented in [33] and [34].

The independent coordinates will be the vectors of nodal displacements which may include the displacements in the three directions of bar ends and derivatives of these values having the significance of rotations and curvatures. The number of independent coordinates chosen depends on the bar hypothesis used; they will determine the values that count for the model description and for the way of choosing the interpolation functions. If a bar is flexible only on its own axis and rigid on the other two axes only the axial displacements of bar ends will be considered as being independent coordinates. But if the bar is rigid in axial direction and flexible in the other directions, the displacements in the directions perpendicular on the bar as well as the rotations of the bar cross - section in two directions perpendicular on the bar are being considered.

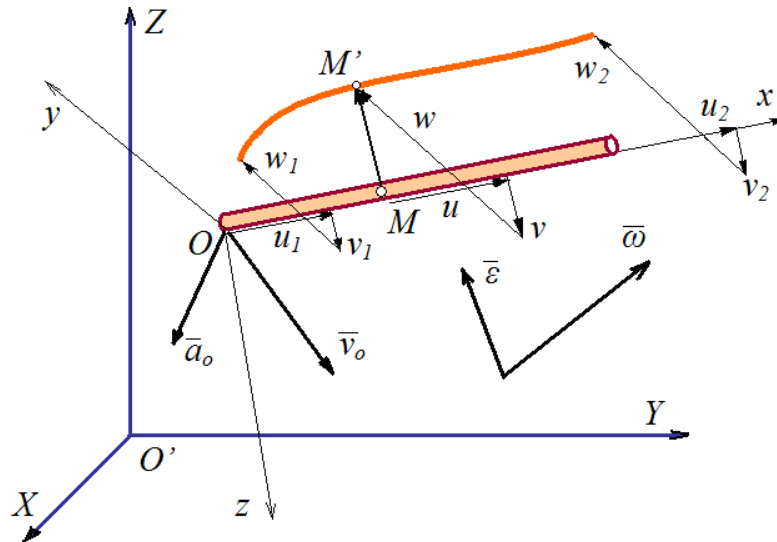


Fig. 1-B. One-dimensional finite element with three-dimensional motion

The aim of the paper is to determine the general motion equations and not to make all the particularizations determined by the idealizations and models chosen. For a type of finite element often used in engineering we shall also obtain the form specific for this case of motion equations

4B.1.2 Lagrangian of the Mechanical System

Within the multibody system containing the finite element the latter has a general three-dimensional rigid body motion. It is assumed that the rigid motion of the mechanical system was previously determined considering all the rigid elements of the multibody system. We start from the hypothesis that the elastic deformations are small and would not influence the general motion of the system of bodies. Thus it is assumed that the velocities and accelerations field for each element of the mechanical system are known.

Let's consider a truss finite element, having at both ends the nodes i and j . δ_i and δ_j represent the displacements of bar ends (Fig.1-B). The finite element is related to a local reference system $Oxyz$ participating to the rigid motion of the bar. We know the velocity and acceleration of the origin of the mobile reference system with respect to the fixed reference system $Ox_1y_1z_1$. The angular velocity and angular acceleration of the mobile reference system is also considered as being known.

The displacement of a point M of bar δ (u, v, w) can be expressed in terms of nodal displacements as follows:

$$\boldsymbol{\delta} = \begin{Bmatrix} u \\ v \\ w \end{Bmatrix} = \mathbf{N} \boldsymbol{\delta}_e = \mathbf{N} \begin{Bmatrix} \boldsymbol{\delta}_1 \\ \boldsymbol{\delta}_2 \end{Bmatrix} \quad \text{Eq. 1-B}$$

where the vector of nodal displacements $\boldsymbol{\delta}_e$ is:

$$\boldsymbol{\delta}_e = \begin{Bmatrix} \boldsymbol{\delta}_1 \\ \boldsymbol{\delta}_2 \end{Bmatrix} \quad \text{Eq. 2-B}$$

and the matrix \mathbf{N} contain shape functions. The lines of the matrix \mathbf{N} corresponding to the displacements u , v and w are named $N_{(u)}$, $N_{(v)}$ and $N_{(w)}$:

$$\mathbf{N} = \begin{bmatrix} N_{(u)} \\ N_{(v)} \\ N_{(w)} \end{bmatrix} \quad \text{Eq. 3-B}$$

The vectors of displacements of the nodes at bar ends (right and left bar ends) have been named $\boldsymbol{\delta}_1$ and $\boldsymbol{\delta}_2$. Thus we have:

$$\boldsymbol{\delta} = \begin{Bmatrix} u \\ v \\ w \end{Bmatrix} = \mathbf{N} \boldsymbol{\delta}_e = \begin{bmatrix} N_{(u)} \\ N_{(v)} \\ N_{(w)} \end{bmatrix} \begin{Bmatrix} \boldsymbol{\delta}_1 \\ \boldsymbol{\delta}_2 \end{Bmatrix} \quad \text{Eq. 4-B}$$

If v and w are the displacements of a bar point in the directions Oy and Oz respectively (displacements perpendicular on the bar axis) we shall have the equations known from the mechanics of continuous media ([35][36][37]):

$$\beta = -\frac{dw}{dx}; \quad \gamma = \frac{dv}{dx} \quad \text{Eq. 5-B}$$

Considering the shape functions, the rotations of the bar ends can be expressed as follows:

$$\beta = -\frac{d}{dx}(N_w \delta_e) = -N'_w \delta_e ; \gamma = \frac{d}{dx}(N_v \delta_e) = N'_v \delta_e \quad \text{Eq. 6-B}$$

In what follows index G applied to a vector or a matrix means that the respective value is expressed in the global reference system and index L means that the respective value is expressed in the local reference system.

As a result of the displacement the position vector of point M becomes in the deformed position M' and can be expressed by:

$$\mathbf{r}_{M',L} = \mathbf{r}_{M,L} + \boldsymbol{\delta} = \mathbf{r}_{M,L} + \begin{Bmatrix} u \\ v \\ w \end{Bmatrix} = \mathbf{r}_{o,L} + \begin{Bmatrix} x+u \\ v \\ w \end{Bmatrix} \quad \text{Eq. 7-B}$$

or, with respect to the global reference system:

$$\mathbf{r}_{M',G} = \mathbf{r}_{M,G} + \mathbf{R} \begin{Bmatrix} u \\ v \\ w \end{Bmatrix} = \mathbf{r}_{o,G} + \mathbf{R} \begin{Bmatrix} x \\ 0 \\ 0 \end{Bmatrix} + \mathbf{R} \begin{Bmatrix} u \\ v \\ w \end{Bmatrix} = \mathbf{r}_{o,G} + \mathbf{R} \begin{Bmatrix} x \\ 0 \\ 0 \end{Bmatrix} + \mathbf{R} \mathbf{N} \delta_{e,L} \quad \text{Eq. 8-B}$$

where the matrix \mathbf{R} expresses the transition of the mobile reference system Oxyz to the fixed reference system O'XYZ . The velocity is given by the relation:

$$\mathbf{v}_{M',G} = \dot{\mathbf{r}}_{M',G} = \dot{\mathbf{r}}_{o,G} + \dot{\mathbf{R}} \begin{Bmatrix} x \\ 0 \\ 0 \end{Bmatrix} + \dot{\mathbf{R}} \mathbf{N} \delta_{e,L} + \mathbf{R} \mathbf{N} \dot{\delta}_{e,L} \quad \text{Eq. 9-B}$$

The kinetic energy expression for the whole bar is:

$$E_c = \frac{1}{2} \int_0^L \rho \left(A \dot{\mathbf{r}}_{M',G}^T \dot{\mathbf{r}}_{M',G} + \boldsymbol{\omega}'_L^T \mathbf{I} \boldsymbol{\omega}'_L \right) dx =$$

$$\begin{aligned}
&= \frac{1}{2} \int_0^L \left(\dot{\mathbf{r}}_{o,G}^T \dot{\mathbf{r}}_{o,G} + 2 \dot{\mathbf{r}}_{o,G}^T \dot{\mathbf{R}} \begin{bmatrix} x \\ 0 \\ 0 \end{bmatrix} + 2 \dot{\mathbf{r}}_{o,G}^T \dot{\mathbf{R}} \mathbf{N} \delta_e + 2 \dot{\mathbf{r}}_{o,G}^T \mathbf{R} \mathbf{N} \dot{\delta}_e + [x \ 0 \ 0] \dot{\mathbf{R}}^T \dot{\mathbf{R}} \begin{bmatrix} x \\ 0 \\ 0 \end{bmatrix} \right) \rho A dx + \\
&+ \frac{1}{2} \int_0^L \left([x \ 0 \ 0] \dot{\mathbf{R}}^T \dot{\mathbf{R}} \mathbf{N} \delta_e + [x \ 0 \ 0] \dot{\mathbf{R}}^T \mathbf{R} \mathbf{N} \dot{\delta}_e + \delta_e^T \mathbf{N}^T \dot{\mathbf{R}}^T \dot{\mathbf{R}} \mathbf{N} \delta_e \right) \rho A dx + \\
&+ \frac{1}{2} \int_0^L \left(2 \delta_e^T \mathbf{N}^T \dot{\mathbf{R}}^T \mathbf{R} \mathbf{N} \dot{\delta}_e + \dot{\delta}_e^T \mathbf{N}^T \mathbf{R}^T \mathbf{R} \mathbf{N} \dot{\delta}_e \right) \rho A dx + \frac{1}{2} \int_0^L \left(\boldsymbol{\omega}'_L{}^T \mathbf{I} \boldsymbol{\omega}'_L \right) \rho A dx
\end{aligned}$$

Eq. 10-B

where:

$$\mathbf{I} = \begin{bmatrix} I_{xx} & 0 & 0 \\ 0 & I_{yy} & -I_{yz} \\ 0 & -I_{yz} & I_{zz} \end{bmatrix} \quad \text{Eq. 11-B}$$

I_{yy} and I_{zz} represent moments of inertia of the bar cross section about co-ordinate axis Oy and Oz respectively of a reference system with its origin in the mass centre of the element $dm = \rho A dx$ (ρ - density); I_{yz} is the centrifugal moment of inertia and I_{xx} is the inertia moment about the co-ordinate axis Ox. Since we have chosen y and z as principal directions of inertia $I_{yz} = 0$, we have:

$$\mathbf{I} = \begin{bmatrix} I_x & 0 & 0 \\ 0 & I_y & 0 \\ 0 & 0 & I_z \end{bmatrix} \quad \text{Eq. 12-B}$$

where, for the sake of simplicity $I_{xx} = I_x$, $I_{yy} = I_y$, $I_{zz} = I_z$. The angular velocity of the element dm is:

$$\boldsymbol{\omega}'_L = \begin{Bmatrix} \omega_{1L} \\ \omega_{2L} \\ \omega_{3L} \end{Bmatrix} + \begin{Bmatrix} \dot{\alpha} \\ \dot{\beta} \\ \dot{\gamma} \end{Bmatrix} = \begin{Bmatrix} \omega_{1L} \\ \omega_{2L} \\ \omega_{3L} \end{Bmatrix} + \mathbf{N}^* \boldsymbol{\delta}_e \quad \text{Eq. 13-B}$$

where: ω_{1L} , ω_{2L} , ω_{3L} are the components of the angular velocity vector related to the mobile reference system.

$$\begin{Bmatrix} \alpha \\ \beta \\ \gamma \end{Bmatrix} = \mathbf{N}^* \boldsymbol{\delta}_e \quad ; \quad \begin{Bmatrix} \dot{\alpha} \\ \dot{\beta} \\ \dot{\gamma} \end{Bmatrix} = \mathbf{N}^* \dot{\boldsymbol{\delta}}_e \quad \text{Eq. 14-B}$$

where: $\mathbf{N}^* = \begin{bmatrix} N_{(\alpha)}^* \\ N_{(\beta)}^* \\ N_{(\gamma)}^* \end{bmatrix}$. Easily can be noted that: $N_{(\beta)}^* = N_w'$ and $N_{(\gamma)}^* = N_v'$.

In the written relations we can notice the occurrence of derivatives of the matrix for positional relation to the global reference system. These derivatives represent angular velocities and accelerations. For a better understanding we shall express these derivatives according to [15].

Next the internal energy stored in the bar as a result of deformation shall be calculated [38][39][40] and [41].

The energy due to bending is given by the expression:

$$E_{pi} = \frac{1}{2} \int_0^L \left[EI_y \left(\frac{d^2 w}{dx^2} \right)^2 + EI_z \left(\frac{d^2 v}{dx^2} \right)^2 \right] dx = \frac{1}{2} \int_0^L [EI_y \beta'^2 + EI_z \gamma'^2] dx \quad \text{Eq. 15-B}$$

If we write:

$$w = \mathbf{N}_{(w)} \boldsymbol{\delta}_e \quad ; \quad v = \mathbf{N}_{(v)} \boldsymbol{\delta}_e \quad \text{Eq. 16-B}$$

then:

$$E_{pi} = \frac{1}{2} \int_0^L \left(EI_y \mathbf{N}_{(w)}''^T \mathbf{N}_{(w)}'' + EI_z \mathbf{N}_{(v)}''^T \mathbf{N}_{(v)}'' \right) dx \boldsymbol{\delta}_e \quad \text{Eq. 17-B}$$

The energy due to axial deformation is:

$$E_{pa} = \frac{1}{2} \int_0^L EA \left(\frac{du}{dx} \right)^2 dx = \frac{1}{2} \delta_e^T \int_0^L (N_u)^T N_u' EA dx \delta_e \quad \text{Eq. 18-B}$$

The deformation energy due to torsion is:

$$E_{pt} = \frac{1}{2} \int_0^L GI_x \left(\frac{d\alpha}{dx} \right)^2 dx = \frac{1}{2} \delta_e^T \left(\int_0^L N_{(\alpha)}^*{}^T N_{(\alpha)}^* GI_x dx \right) \delta_e \quad \text{Eq. 19-B}$$

The axial load P in an axial section of the bar gives the energy if in a first approximation the axial deformations are neglected:

$$E_a = \frac{1}{2} \int_0^L P_{tot} \left[\left(\frac{dv}{dx} \right)^2 + \left(\frac{dw}{dx} \right)^2 \right] dx \quad \text{Eq. 20-B}$$

where P_{tot} represents the axial force in the bar cross section at distance x . The force components acting at the right bar end considered in the local coordinate system are represented by $P_x, P_y=0, P_z=0$. Beside these components, the value of P and the components of the inertia forces acting upon the portion of the bar between x and L are being determined. In order to calculate them we determine the acceleration of the current point of the bar in the rigid motion (Fig.2-B):

$$\mathbf{a}_G = \mathbf{a}_{o,G} + \boldsymbol{\varepsilon}_G \mathbf{R} \begin{Bmatrix} x \\ 0 \\ 0 \end{Bmatrix} + \boldsymbol{\omega}_G \boldsymbol{\omega}_G \mathbf{R} \begin{Bmatrix} x \\ 0 \\ 0 \end{Bmatrix} = \mathbf{a}_{o,G} + \mathbf{R} \boldsymbol{\varepsilon}_L \begin{Bmatrix} x \\ 0 \\ 0 \end{Bmatrix} + \mathbf{R} \boldsymbol{\omega}_L \boldsymbol{\omega}_L \begin{Bmatrix} x \\ 0 \\ 0 \end{Bmatrix} \quad \text{Eq. 21-B}$$

The inertia force is given by:

$$\mathbf{F}_i = - \int_x^L \mathbf{a}_G dm = - \int_x^L \mathbf{a}_{o,G} \rho A ds - \int_x^L \mathbf{R} \boldsymbol{\varepsilon}_L \begin{Bmatrix} s \\ 0 \\ 0 \end{Bmatrix} \rho A ds - \int_x^L \mathbf{R} \boldsymbol{\omega}_L \boldsymbol{\omega}_L \begin{Bmatrix} s \\ 0 \\ 0 \end{Bmatrix} \rho A ds =$$

$$= - \begin{Bmatrix} \ddot{X}_o \\ \ddot{Y}_o \\ \ddot{Z}_o \end{Bmatrix} \left\{ \rho A(L-x) - \frac{1}{2} \mathbf{R} \boldsymbol{\varepsilon}_L \begin{Bmatrix} L^2 - x^2 \\ 0 \\ 0 \end{Bmatrix} \right\} \rho A - \frac{1}{2} \mathbf{R} \boldsymbol{\omega}_L \boldsymbol{\omega}_L \begin{Bmatrix} L^2 - x^2 \\ 0 \\ 0 \end{Bmatrix} \rho A \quad \text{Eq. 22-B}$$

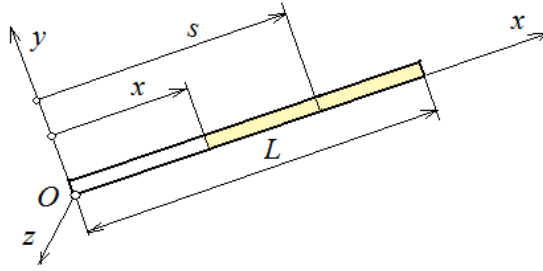


Fig. 2-B. Determination of the axial inertia force

$$\{\mu\} = \begin{Bmatrix} \mu_x \\ \mu_y \\ \mu_z \end{Bmatrix} = -\rho A L \begin{Bmatrix} \ddot{X}_o \\ \ddot{Y}_o \\ \ddot{Z}_o \end{Bmatrix} - \frac{1}{2} \mathbf{R} \boldsymbol{\varepsilon}_L \begin{Bmatrix} 1 \\ 0 \\ 0 \end{Bmatrix} \rho A L^2 - \frac{1}{2} \mathbf{R} \boldsymbol{\omega}_L \boldsymbol{\omega}_L \begin{Bmatrix} 1 \\ 0 \\ 0 \end{Bmatrix} \rho A L^2 \quad \text{Eq. 23a-B}$$

$$\{\lambda\} = \begin{Bmatrix} \lambda_x \\ \lambda_y \\ \lambda_z \end{Bmatrix} = \rho A \begin{Bmatrix} \ddot{X}_o \\ \ddot{Y}_o \\ \ddot{Z}_o \end{Bmatrix} \quad \text{Eq. 23b-B}$$

$$\{\nu\} = \begin{Bmatrix} \nu_x \\ \nu_y \\ \nu_z \end{Bmatrix} = \frac{1}{2} \mathbf{R} \boldsymbol{\varepsilon}_L \begin{Bmatrix} 1 \\ 0 \\ 0 \end{Bmatrix} \rho A + \frac{1}{2} \mathbf{R} \boldsymbol{\omega}_L \boldsymbol{\omega}_L \begin{Bmatrix} 1 \\ 0 \\ 0 \end{Bmatrix} \rho A \quad \text{Eq. 23c-B}$$

We obtain the internal energy due to inertia in the form of:

$$E_a = \frac{1}{2} \boldsymbol{\delta}_e^T \left[\int_0^L (P_x + \mu_x + \lambda_x x + \nu_x x^2) \left(\mathbf{N}_{(\gamma)}^{*T} \mathbf{N}_{(\gamma)}^* + \mathbf{N}_{(\beta)}^{*T} \mathbf{N}_{(\beta)}^* \right) dx \right] \boldsymbol{\delta}_e \quad \text{Eq. 24-B}$$

$$E_a = \frac{1}{2} \boldsymbol{\delta}_e^T \mathbf{k}_e^G \boldsymbol{\delta}_e \quad \text{Eq. 25-B}$$

where the notation for \mathbf{k}_e^G is obvious. The total internal energy is:

$$E_p = \boldsymbol{\delta}_e^T (\mathbf{k}_i + \mathbf{k}_a + \mathbf{k}_t + \mathbf{k}_e^G) \boldsymbol{\delta}_e \quad \text{Eq. 26-B}$$

The external work of distributed loads is:

$$\begin{aligned} W &= \int_0^L (p_x u + p_y v + p_z w + m_x \alpha + m_y \beta + m_z \gamma) dx = \\ &= \int_0^L \begin{bmatrix} p_x & p_y & p_z & m_x & m_y & m_z \end{bmatrix} \begin{bmatrix} N \\ N^* \end{bmatrix} \boldsymbol{\delta}_e dx \end{aligned} \quad \text{Eq. 27-B}$$

and that of concentrated loads \mathbf{q}_{eL}^T in the nodes is:

$$W^c = \mathbf{q}_{eL}^T \boldsymbol{\delta}_e \quad \text{Eq. 28-B}$$

The Lagrangian for the element is [42][43][44][45][46] and [47]:

$$L = E_c - E_p - E_a + W + W^c. \quad \text{Eq. 29-B}$$

4B.2 Two-dimensional finite element

4B.2.1 Motion's equations for a two-dimensional finite element

Let's consider a two-dimensional finite element with a plan parallel motion. The type of finite element which will be used will determine the shape functions and the final form for the matrix coefficients. In what follows it is considered that the deformations are small enough not to influence the general rigid motion of the system.

Both the problem of the rigid motion of the system and the field of velocities and accelerations for each two-dimensional element of the multicorp systems are considered to be solved ([34]). The finite element is related to the local coordinates system Oxy, which is mobile and which participates to the whole motion (Fig. 3-B), so it has a known rigid motion. Let's consider $\mathbf{v}_o(\dot{X}_o, \dot{Y}_o, 0)$ being the velocity

and $\mathbf{a}_o(\ddot{X}_o, \ddot{Y}_o, 0)$ being the acceleration of the origin of the mobile reference system related to the fixed reference system OXY, to which the whole motion of the mechanical system relates. We will consider $\boldsymbol{\omega}(0, 0, \omega_z)$ as being the angular velocity of the solid containing the finite element and $\boldsymbol{\varepsilon}(0, 0, \varepsilon)$ as being the angular acceleration of the same solid.

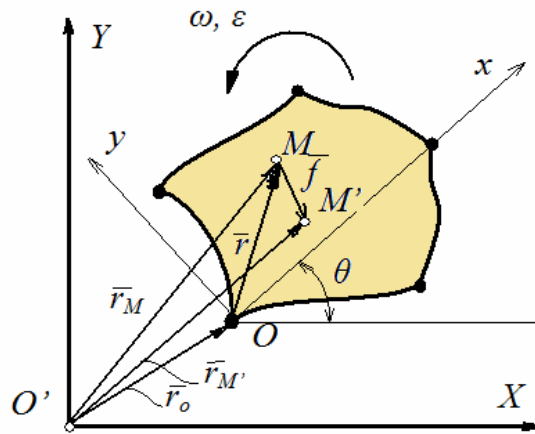


Fig. 3-B. A two-dimensional finite element with plan motion

The change in the values of the position vector $\mathbf{r}_{M,G}$ of a random point M of the finite element when going from the local Oxy reference system into the global fixed OXY reference system is obtained using a rotation transformation matrix \mathbf{R} . If we consider $\mathbf{r}_{M,G}$ as being the position vector of the M point, we have:

$$\mathbf{r}_{M,G} = \mathbf{r}_{O,G} + \mathbf{r}_G = \mathbf{r}_{O,G} + \mathbf{R} \cdot \mathbf{r}_L \quad \text{Eq. 30-B}$$

where we consider G defining the vectorial entities which have their components relating to the global reference system and L defining the vectorial entities which have their components relating to the local reference system.

The rotation transformation matrix R has, in this situation, a very simple form:

$$\mathbf{R} = \begin{bmatrix} \cos \theta & -\sin \theta \\ \sin \theta & \cos \theta \end{bmatrix} \quad \text{Eq. 31-B}$$

If the M point is subjected to a displacement \mathbf{f}_L , transforming into the M' point, we will have:

$$\mathbf{r}_{M',G} = \mathbf{r}_{O,G} + \mathbf{R} \cdot (\mathbf{r}_L + \mathbf{f}_L) \quad \text{Eq. 32-B}$$

where $\mathbf{r}_{M',G}$ is the position vector of the point M' with its components relating to the global reference system. The continuous displacement field $\mathbf{f}(x,y)_L$ is approximated in the finite element method, depending on the nodal displacements, using the relationship:

$$\mathbf{f}_L = \mathbf{N}(x,y) \boldsymbol{\delta}_e(t)_L \quad \text{Eq. 33-B}$$

where the elements of the \mathbf{N} matrix (which contains the interpolation functions) depend on the type of the chosen finite element. The velocity of the M' point, related to the fixed coordinate system, will be:

$$\mathbf{v}_{M',G} = \dot{\mathbf{r}}_O + \dot{\mathbf{R}} \mathbf{r}_L + \dot{\mathbf{R}} \mathbf{f}_L + \mathbf{R} \dot{\mathbf{f}}_L = \dot{\mathbf{r}}_O + \dot{\mathbf{R}} \mathbf{r}_L + \dot{\mathbf{R}} \mathbf{N} \boldsymbol{\delta}_{e,L} + \mathbf{R} \mathbf{N} \dot{\boldsymbol{\delta}}_{e,L}$$

Eq. 34-B

The velocity components are defined related to the global coordinates system. The equations of motion will be obtained in the local coordinates system.

The kinetic energy of the considered element will be determined using the relationship:

$$E_c = \frac{1}{2} \int_V \rho v^2 dV = \frac{1}{2} \int_V \rho \mathbf{v}_{M',L}^T \mathbf{v}_{M',L} dV. \quad \text{Eq. 35-B}$$

When we determined the kinetic energy, we could have been representing the velocity in the global coordinates system, the result for the kinetic energy remaining the same.

This happens because the scalar product of two vectors remains the same, no matter which reference system we use.

The deformation energy is:

$$E_p = \frac{1}{2} \int_V \boldsymbol{\sigma}^T \boldsymbol{\varepsilon} dV. \quad \text{Eq. 36-B}$$

For the ease of understanding, we remember that the generalized Hooke law is:

$$\boldsymbol{\sigma} = \mathbf{D} \cdot \boldsymbol{\varepsilon} \quad \text{Eq. 37-B}$$

where, for a two-dimensional finite element (plane state of deformation) we have:

$$\mathbf{D} = \frac{E}{(1-\mu)(1-2\mu)} \begin{bmatrix} 1-\mu & 0 & 0 \\ 0 & 1-\mu & 0 \\ 0 & 0 & \frac{1-2\mu}{2} \end{bmatrix} \quad \text{Eq. 38-B}$$

and the relation between the specific deformations and the finite deformations can be expressed using the relationship:

$$\boldsymbol{\varepsilon} = \mathbf{a} \cdot \mathbf{f} \quad \text{Eq. 39-B}$$

where \mathbf{a} is a differentiation operator:

$$\mathbf{a} = \begin{bmatrix} \frac{\partial}{\partial x} & 0 & 0 \\ 0 & \frac{\partial}{\partial y} & 0 \\ \frac{\partial}{\partial y} & \frac{\partial}{\partial x} & 0 \end{bmatrix} \quad \text{Eq. 40-B}$$

Considering all this, for the deformation energy we have:

$$E_p = \frac{1}{2} \int_V \boldsymbol{\delta}_{e,L}^T \mathbf{k}_e \boldsymbol{\delta}_{e,L} dV \quad \text{Eq. 41-B}$$

with \mathbf{k}_e being the stiffness matrix:

$$\mathbf{k}_e = \int_V \mathbf{N}^T \mathbf{a}^T \mathbf{D}^T \mathbf{a} \mathbf{N} dV. \quad \text{Eq. 42-B}$$

If we consider $\mathbf{p} = \mathbf{p}(x,y)$ as being the vector for the distributed forces, then the external machine work of those forces is:

$$W = \int_V \mathbf{p}_L^T \mathbf{f}_L dV = \left(\int_V \mathbf{p}_L^T \mathbf{N} dV \right) \boldsymbol{\delta}_{e,L}. \quad \text{Eq. 43-B}$$

The nodal forces \mathbf{q}_e^T give an external machine work:

$$W^c = \mathbf{q}_{e,L}^T \boldsymbol{\delta}_{e,L}. \quad \text{Eq. 44-B}$$

The Lagrangian for the considered element is:

$$\begin{aligned} L &= E_c - E_p + W + W^c = \\ &= \frac{1}{2} \int_V \rho \dot{\mathbf{r}}_o^T \dot{\mathbf{r}}_o dV - \frac{1}{2} \int_V \boldsymbol{\delta}_{e,L}^T \mathbf{k}_e \boldsymbol{\delta}_{e,L} dV + \left(\int_V \mathbf{p}_L^T \mathbf{N} dV \right) \boldsymbol{\delta}_{e,L} + \mathbf{q}_{e,L}^T \boldsymbol{\delta}_{e,L} \end{aligned} \quad \text{Eq. 45-B}$$

The equations of motion are obtained by applying the Lagrange equations. After some ordering, we can write the equations of motion for the finite element like this:

$$\begin{aligned} & \left(\int_V \mathbf{N}^T \mathbf{N} \rho dV \right) \ddot{\boldsymbol{\delta}}_{e,L} + 2 \left(\int_V \mathbf{N}^T \mathbf{R}^T \dot{\mathbf{R}} \mathbf{N} \rho dV \right) \dot{\boldsymbol{\delta}}_{e,L} + \\ & + \left(\mathbf{k}_e + \int_V \mathbf{N}^T \mathbf{R}^T \ddot{\mathbf{R}} \mathbf{N} \rho dV \right) \boldsymbol{\delta}_{e,L} = \end{aligned}$$

$$= \mathbf{q}_e + \int_V \mathbf{N}^T \mathbf{p}_L dV - \left(\int_V \mathbf{N}^T \rho dV \right) \mathbf{R}^T \ddot{\mathbf{r}}_o - \int_V \mathbf{N}^T \mathbf{R}^T \ddot{\mathbf{R}} \mathbf{r} \rho dV$$

Eq. 46-B

We can write the equations of motion in concentrated form:

$$\begin{aligned} & \mathbf{m}_e \ddot{\boldsymbol{\delta}}_{e,L} + 2\mathbf{c}_e \dot{\boldsymbol{\delta}}_{e,L} + [\mathbf{k}_e + \mathbf{k}_e(\varepsilon) + \mathbf{k}_e(\omega^2)] \boldsymbol{\delta}_{e,L} = \\ & = \mathbf{q}_e + \mathbf{q}_{e,L}^* - \mathbf{q}_{e,L}^i(\varepsilon) - \mathbf{q}_{e,L}^i(\omega^2) - \mathbf{m}_{oe}^i \mathbf{R}^T \ddot{\mathbf{r}}_o \end{aligned}$$

Eq. 47-B

where we considered:

$$\begin{aligned} \mathbf{q}_{e,L}^* &= \int_V \mathbf{N}^T \mathbf{p}_L dV ; \quad \mathbf{m}_{oe}^i = \int_V \mathbf{N}^T \rho dV ; \quad \mathbf{m}_e = \int_V \mathbf{N}^T \mathbf{N} \rho dV = \mathbf{m}_{11} + \mathbf{m}_{22} \\ \mathbf{c}_e(\omega) &= \int_V \mathbf{N}^T \mathbf{R}^T \dot{\mathbf{R}} \mathbf{N} \rho dV ; \quad \mathbf{k}_e(\varepsilon) + \mathbf{k}_e(\omega^2) = \int_V \mathbf{N}^T \mathbf{R}^T \ddot{\mathbf{R}} \mathbf{N} \rho dV \\ \mathbf{q}_{e,L}^i(\varepsilon) + \mathbf{q}_{e,L}^i(\omega) &= \int_V \mathbf{N}^T \mathbf{R}^T \ddot{\mathbf{R}} \mathbf{r} \rho dV \end{aligned}$$

Eq. 48-B

The matrix products where the rotation transformation matrix appears can easily be calculated, as this matrix is determined by only one element, the angle θ . The anti-symmetric matrix:

$$\boldsymbol{\omega} = \dot{\mathbf{R}} \mathbf{R}^T = \begin{bmatrix} 0 & -\omega \\ \omega & 0 \end{bmatrix} = \omega \begin{bmatrix} 0 & -1 \\ 1 & 0 \end{bmatrix}$$

Eq. 49-B

represents the angular velocity operator corresponding to the angular velocity ω . We also have:

$$\ddot{\mathbf{R}} \mathbf{R}^T = \varepsilon \begin{bmatrix} 0 & -1 \\ 1 & 0 \end{bmatrix} - \omega^2 \begin{bmatrix} 1 & 0 \\ 0 & 1 \end{bmatrix}$$

Eq. 50-B

In both the global and local reference systems, the angular velocity and angular acceleration vectors have the same components.

If we consider $N_{(1)}$ and $N_{(2)}$ being the rows of the matrix N , with the notations:

$$\begin{aligned} \mathbf{m}_{1x} &= \int_V N_{(1)}^T x \rho dV ; \quad \mathbf{m}_{1y} = \int_V N_{(1)}^T y \rho dV ; \quad \mathbf{m}_{11} = \int_V N_{(1)} N_{(1)}^T \rho dV \\ \mathbf{m}_{2x} &= \int_V N_{(2)}^T x \rho dV ; \quad \mathbf{m}_{2y} = \int_V N_{(2)}^T y \rho dV ; \quad \mathbf{m}_{22} = \int_V N_{(2)} N_{(2)}^T \rho dV \end{aligned}$$

Eq. 51-B

we can obtain the equations of motion for the finite element, with explicit dependencies to the angular velocity ω and angular acceleration ε . Previously, we solve the integrals with the given notations and we can obtain a detailed form for the equations of motion. Therefore, we have:

$$\begin{aligned} \mathbf{m}_e &= (\mathbf{m}_{11} + \mathbf{m}_{22})_e ; \quad \mathbf{c}_e(\omega) = \omega (m_{21} - m_{12})_e \\ \mathbf{k}_e(\varepsilon) + \mathbf{k}_e(\omega^2) &= \varepsilon (m_{21} - m_{12})_e - \omega^2 (m_{11} - m_{22})_e \\ \mathbf{q}_{e,L}^i(\varepsilon) + \mathbf{q}_{e,L}^i(\omega) &= \varepsilon (m_{2x} - m_{1y})_e - \omega^2 (m_{1x} + m_{2y})_e \end{aligned} \quad \text{Eq. 52-B}$$

The equations of motion will be, in this case:

$$\begin{aligned} &(\mathbf{m}_{11} + \mathbf{m}_{22})_e \ddot{\boldsymbol{\delta}}_{e,L} + 2\omega (m_{21} - m_{12})_e \dot{\boldsymbol{\delta}}_{e,L} + \\ &+ [\mathbf{k}_e + \varepsilon (m_{21} - m_{12})_e - \omega^2 (m_{11} + m_{22})_e] \boldsymbol{\delta}_{e,L} = \\ &= \mathbf{q}_e^{ext} + \mathbf{q}_e^{liaison} - \varepsilon (m_{2x} - m_{1y})_e + \omega^2 (m_{1x} + m_{2y})_e - \mathbf{m}_{oe}^i \mathbf{R}^T \ddot{\mathbf{r}}_o \end{aligned} \quad \text{Eq. 53-B}$$

The unknowns in the finite element analysis of such a system are of two kinds: nodal displacements and contact forces. Using a correct assembly of the equations of motion, written by each finite element, the algebraic unknowns (the contact forces) can be removed [13][14][46][48]. The equations of motion for the whole multibody system will be possible to be written as a system of 2nd order non-linear differential equations. The matrix coefficients of this system of equations have the following properties:

- The inertial matrix \mathbf{m} is symmetric;
- The damping matrix \mathbf{c} is a skew symmetric matrix. The terms defined by this matrix represent the Coriolis accelerations, , due to relative motions of

nodal displacements with respect to the mobile reference coordinate system, linked to the moving parts of the system studied;

- The stiffness matrix \mathbf{k} contains both symmetric and skew symmetric terms. Moreover, this matrix can have singularities due to the rigid motion of the system that have to be removed before conducting the study of the system.

4B.2.2 Modal analysis of a rotating disk

In the following there are presented results obtained by the author in the case of a particular case, when we study a rotating homogeneous disk [30].

Let's consider a rotating disk. If we consider a stationary motion, the disk will rotate with an angular velocity ω . In a very small interval Δt we may consider that the angular velocity is constant and we intend to achieve the modal analysis of rotating disk. We will use the method previously presented for carrying out the calculation and compare the result with that obtained by applying the classic version of the method of finite elements. We consider two cases:

Table 1-B. Eigenvalues of a rotating disk

Mode number (without rigid body mode)	Classic model - eigenvalues (Hz)	Proposed model – eigenvalues (Hz)
4	5514	5865
5	5514	5865
6	7045	7323
7	7045	7323
8	8959	9180
9	8959	9180
10	9416	9626
11	10641	10827
12	10641	10827
13	11713	11883
14	11713	11883
15	12767	12923
16	14284	14423
17	14284	14423
18	14910	15044

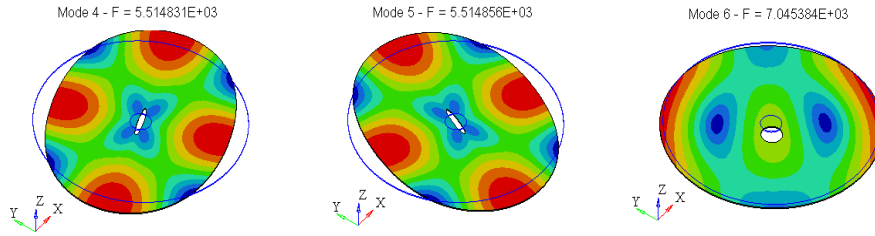


Fig. 4-B. Eigenmodes 4, 5 and 6

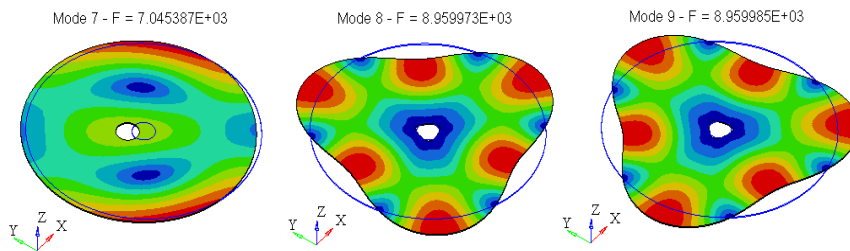


Fig. 5-B. Eigenmodes 7, 8 and 9

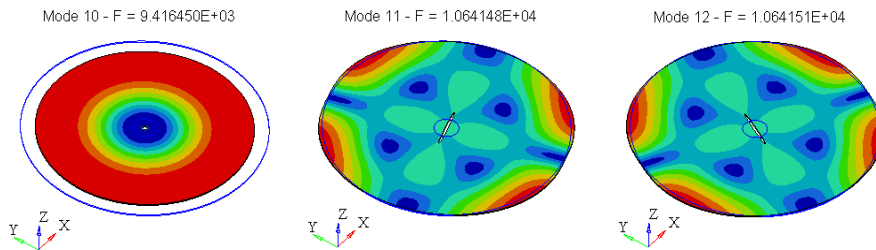


Fig. 6-B. Eigenmodes 10,11 and 12

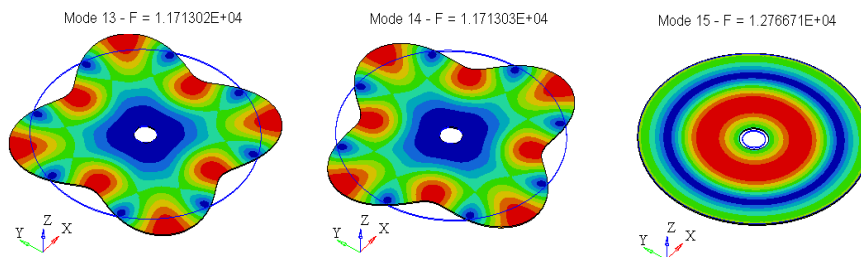


Fig. 7-B. Eigenmodes 13,14 and 15

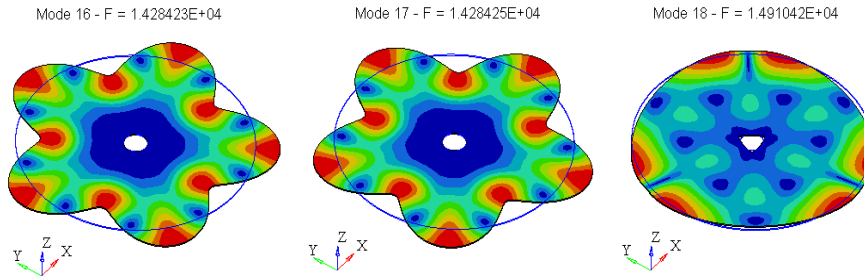


Fig. 8-B. Eigenmodes 16, 17 and 18

- A. The rotating disk has a plan motion and the finite element is in a plane displacement field. The eigenvalues are presented in Table 1-B and the eigenvector in Fig.4-B-Fig.8-B.
- B. The rotating disk has a plan motion and the finite element is in a general displacement field. The eigenmodes are presented in Fig.9-B - Fig.13-B.

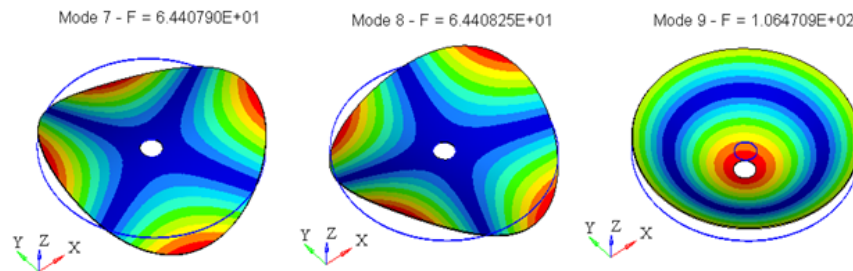


Fig. 9-B. Eigenmodes 7, 8 and 9

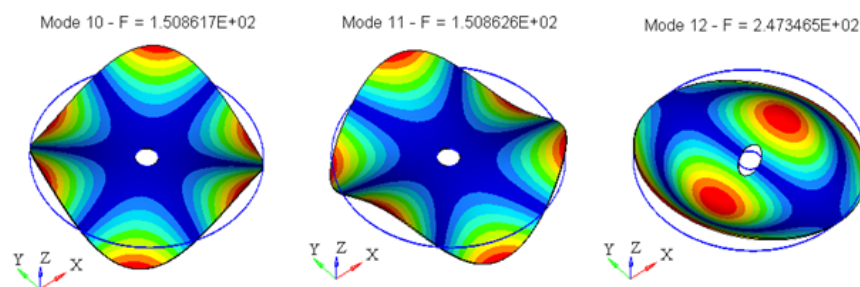


Fig. 10-B. Eigenmodes 10, 11 and 12

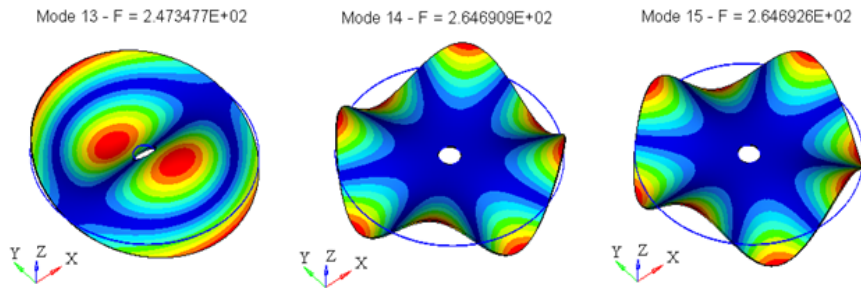


Fig. 11-B. Eigenmodes 13, 14 and 15

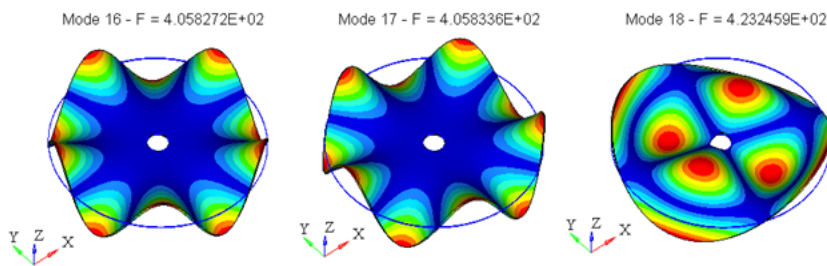


Fig. 12-B. Eigenmodes 16, 17 and 18

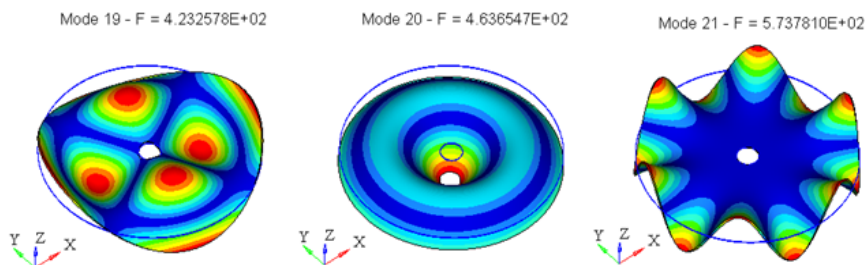


Fig. 13-B. Eigenmodes 19,20 and 21

The additional terms in the equations of motion will influence the dynamic response of the system. It may happen that a resonant state or a loss of stability state to be reached. The modifications of eigenvalues considering a rotating disk (along its own axis) is presented in the paper. An upwards displacement for all the eigenvalues can be observed - this happens because an increase in stiffness takes place in this situation (rotation), due to the inertial forces. The vibration modes remain practically the same, while a small change in the amplitudes can be observed. The presence of inertial and

Coriolis effects can significantly modify, in some situations, the dynamic response of the system.

4B.3 References

- [1] Thomson, B.S., Sung, C.K., A survey of Finite Element Techniques for Mechanism Design. *Mech.Mach.Theory*, 21, nr. 4, p. 351–359 (1986).
- [2] Nath, P.K., Ghosh, A., Kineto-Elastodynamic Analysis of Mechanisms by Finite Element Method, *Mech.Mach.Theory*, 15, pp. 179 (1980a).
- [3] Nath, P.K., Ghosh, A., Steady-state Response of Mechanisms with Elastic Links by Finite Element Method. *Mech.Mach.Theory*, 15, pp. 199 (1980b).
- [4] Nguyen, V.K., Zur Dynamischen Analyse Ebener Mechanismen mit mehrere Freitsgraden unter Beruecksichtigung der Gestell Schwingungen Ebener Mechanismen. *St.Cerc.Mec.Apl.*, Tom 29,Nr.3 (1984).
- [5] Nguyen, V.K., Ueber der Einfluss von Schwingungen des Gestells auf die Dynamischen Stabilitaetsbedigungen und Periodischen Schwingungen Ebener Mechanismen. *St.Cerc.Mec.Apl.*, Tom 29,Nr.3 (1984).
- [6] Pandrea, N., Le calcul des forces dans les mécanismes à barres linéairment élastiques. *Rev.Roum.Sci.Tech-Méc.Appl.*, Tom 33, Nr.1, p.73 (1988).
- [7] Pandrea,N., Nicolaescu, N., Kineto-static Analysis of a Plane Mechanism with Joints using Finite Element Method. (In Romanian). *Mechanisms and Mechanical Transmission*, Timisoara, p.255 (1980).
- [8] Vlase, S., On the Motion Equation of the Mechanism using Finite Element Method (In Romanian). *PRASIC Symposium, Brasov*,vol.I, p.189 (1982).
- [9] Vlase, S., Motion Equations for a Planar Finite Element (In Romanian). *PRASIC Symposium, Brasov*, Vol.I, p.183 (1982).
- [10] Vlase, S., Elastodynamische Analyse der Mechanischen Systeme durch die Methode der Finiten Elemente. *Bul. Univ. Brasov*, p.1-6 (1984).
- [11] Vlase, S., Ein Ebenes Finiten Element in Zustand einer Membrane fuer Elastodynamische Analyse der Mechanischer Systeme. *Bul. Univ. Braşov*, p.547 (1985).
- [12] Vlase, S., Bewegungsleichungen fuer ein Finit Element mit allgemeiner Bewegung.*Bul. Univ.Braşov*, seria A, Vol.XXVIII, p.19-26 (1986).
- [13] Vlase, S., A Method of Eliminating Lagrangean Multipliers from the Equations of Motion of Interconnected Mechanical Systems. *Journal of applied Mechanics*, ASME Transactions, vol. 54, nr. 1 (1987).
- [14] Vlase, S., Elimination of Lagrangean Multipliers. *Mechanics Research Communications*, vol. 14, pp. 17–22 (1987).
- [15] Vlase, S., Contributions to the elastodynamic analysis of the mechanisms with the finite element method (In Romanian). Ph.D., Transilvania University (1989).
- [16] Vlase, S., Finite Element Analysis of the Planar Mechanisms: Numerical Aspects. In *Applied Mechanics - 4*. Elsevier, pp.90-100 (1992).
- [17] Vlase, S., Teodorescu-Draghicescu, H., Calin, M.R., Scutaru, M.L., Advanced Polylyte composite laminate material behavior to tensile stress on weft

- direction. *Journal of Optoelectronics and Advanced Materials*, Vol. 14, No. 7- 8, p. 658 – 663 (2012).
- [18] Vlase, S., Teodorescu, P.P., Elasto-dynamics of a solid with a general “rigid” motion using FEM model. Part I. *Rom. Journ. Phys.*, Vol. 58, Nos. 7–8, P. 872-881, Bucharest, (2013).
- [19] Vlase, S., Teodorescu, P.P., Itu, C., Scutaru, M.L., Elasto-Dynamics of a Solid with a General “Rigid” Motion using FEM Model. Part II. Analysis of a Double Cardan Joint. Vol.58, No.7-8,p.882-892 (2013).
- [20] An, Y.C., Wang, X.H., Elastodynamic Analysis of Open Chain Mechanism with N DOF. *SYROM*, Bucuresti, Vol.II-1, p.1 (1985).
- [21] Deu J.-F., Galucio A.C., Ohayon R., Dynamic responses of flexible-link mechanisms with passive/active damping treatment. *Computers & Structures*, Volume 86, Issues 3–5, pp. 2 (2008).
- [22] Fanghella P., Galletti C., Torreg G., An explicit independent-coordinate formulation for the equations of motion of flexible multibody systems. *Mech. Mach. Theory*, 38, p. 417–437 (2003).
- [23] Hou W., Zhang X., Dynamic analysis of flexible linkage mechanisms under uniform temperature change. *Journal of Sound and Vibration*, Volume 319, Issues 1–2, Pages 570–592 (2009).
- [24] Neto M.A., Ambrosio J.A.C, Leal R.P., Composite materials in flexible multibody systems. *Computer Methods in Applied Mechanics and Engineering*, Volume 195, Issues 50–51, p. 6860–6873 (2006).
- [25] Shi Y.M., Li Z.F., Hua H.X., Fu Z.F., Liu T.X., The Modelling and Vibration Control of Beams with Active Constrained Layer Damping. *Journal of Sound and Vibration*, Volume 245, Issue 5, p. 785–800 (2001).
- [26] Zhang X., Lu J., Shen Y., Simultaneous optimal structure and control design of flexible linkage mechanism for noise attenuation. *Journal of Sound and Vibration*, Volume 299, Issues 4–5, p. 1124–1133, (2007).
- [27] Ibrahimbegovic, A., Mamouri, S., Taylor, R.L., Chen, A.J., Finite Element Method in Dynamics of Flexible Multibody Systems: Modeling of Holonomic Constraints and Energy Conserving Integration Schemes, *Multibody System Dynamics*, Volume 4, Numbers 2–3, 195–223 (2000).
- [28] Khulief, Y.A., On the finite element dynamic analysis of flexible mechanisms. *Computer Methods in Applied Mechanics and Engineering*, Volume 97, Issue 1, Pages 23–32 (1992).
- [29] Zhang X., Erdman A.G., Dynamic responses of flexible linkage mechanisms with viscoelastic constrained layer damping treatment. *Computers & Structures*, Volume 79, Issue 13, p. 1265–1274 (2001).
- [30] Vlase, S., Eigenvalues and Eigenmodes of an Inclined Homogeneous Truss in a Rotational Field. *Rom. Journ. Phys.*, 59, 699-714 (2014).
- [31] Sung, C.K., An Experimental Study on the Nonlinear Elastic Dynamic Response of Linkage Mechanism. *Mech. Mach. Theory*, 21, p.121–133 (1986).
- [32] Alexandre, R.M., Lawrence, K.L., An Experimental Investigation of the Dynamic Response of an Elastic Mechanism. *Journal of REngineering for Industry*, ASME Transaction, February, p.269,(1974).
- [33] Biancolini, M.E., Brutti, C., Pennestri, E., Valentini, P.P., Dynamic, mechanical efficiency and fatigue analysis of the double cardan homokinetic joint,

- Journal of Vehicle Design, vol.32, n.3/4, pp.231-249 (2003).
- [34] Pennestri, E., De Falco, D., Vita, L., An Investigation of the Influence of Pseudoinverse Matrix Calculations on Multibody Dynamics by Means of the Udwadia-Kalaba Formulation, *Journal of Aerospace Engineering*, Volume 22, Issue 4, pp. 365-372 (2009).
- [35] Akin, J.E., *Application and Implementation of Finite Element Methods*. Academic Press, (1982).
- [36] Bathe, K.J., Wilson, E., *Numerical Methods in Finite Element Analysis*. Prentice Hall, Inc., (1976).
- [37] Cleghorn, W.L., Fenton, E. G., Tabarrok, K.B., *Finite Element Analysis of High-Speed Flexible Mechanism*. *Mech.Mach.Theory*, 16, p. 407 (1981).
- [38] Midha, A., s.a., *Finite Element Approach to Mathematical Modeling of High Speed Elastic Linkage*. *Mechanism and Machine Theory*, Vol. 13, p.603 (1978).
- [39] Massonet, CH., s.a., *Calculul structurilor la calculatoarele electronice*. Ed. Tehnică, București (1974).
- [40] Erdman, A. G., Sandor, G. N., Oakberg, A., *A General Method for Kineto-Elastodynamic Analysis and Synthesis of Mechanisms*. *Journal of Engineering for Industry*. ASME Trans., p.1193 (1972).
- [41] Gioncu, V., Ivan, M., *Basis of the Stability Structures Calculus (in Romanian)*. Ed. Facla, Timisoara (1983).
- [42] Simeon, B., *On Lagrange multipliers in flexible multibody dynamic*. *Computer Methods in Applied Mechanics and Engineering*, Volume 195, Issues 50-51, Pages 6993-7005 (2006).
- [43] Alexandre, R. M., Lawrence, K. L., *An Experimental Investigation of the Dynamic Response of an Elastic Mechanism*. *Journal of REngineering for Industry*, ASME Transaction, February, p.269,(1974).
- [44] Bagci, C., *Elastodynamic Response of Mechanical Systems using Matrix Exponential Mode Uncoupling and Incremental Forcing Techniques with Finite Element Method*. *Proceeding of the Sixth World Congress on Theory of Machines and Mechanisms*, India, p. 472 (1983)
- [45] Bagnaru, D., Nanu, G. H., Iordachita, I., *Modeles à un nombre fini de degrés de liberté pour les mechanisms spatiaux à éléments déformables*. SYROM, București, Vol.II-2, p.27 (1985).
- [46] Khang N.V., *Kronecker product and a new matrix form of Lagrangian equations with multipliers for constrained multibody systems*, *Mechanics Research Communications*, Volume 38, Issue 4, pp. 294–299 (2011).
- [47] Blejwas, E.T., *The Simulation of Elastic Mechanisms using Kinematic Constraints and Lagrange Multipliers*. *Mechanism and Machine Theory*, Vol.16, Nr.4, p.425 (1981).
- [48] Blajer W., Kolodziejczyk, K., 2011, *Improved DAE formulation for inverse dynamics simulation of cranes*, *Multibody Syst Dyn* 25: 131–143 (2011).

Annex 4C

Numerical prediction of the sound field produced by the alerting system of EVs and HVs using the BEM

Luís Godinho¹, Alba Sánchez-Milan², Paulo Amado Mendes³, Ramon Peral-Orts⁴,
Núria Campillo Davó⁵

¹ Luís Godinho, ISISE, Dept. of Civil Engineering, University of Coimbra, Portugal, lgodinho@dec.uc.pt

² Alba Sánchez-Milan, Departamento de Ingeniería Mecánica y Energía, Universidad Miguel-Hernandez, Elche, España, albasanchezmilan@gmail.com

³ Paulo Amado Mendes, ISISE, Dept. of Civil Engineering, University of Coimbra, Portugal, pamendes@dec.uc.pt

⁴ Ramon Peral-Orts, Departamento de Ingeniería Mecánica y Energía, Universidad Miguel-Hernandez, Elche, España, ramon.peral@umh.es

⁵ Núria Campillo Davó, Departamento de Ingeniería Mecánica y Energía, Universidad Miguel-Hernandez, Elche, España, ncampillo@umh.es

Abstract. In recent years, both the scientific and the technical community addressed the topic of noise emission by different types of vehicles. In the particular case of electrical and hybrid vehicles, the specific problem of near-field sound emission is a concern, since at low speed these vehicles are considerably silent, and thus much less detectable in a city environment. Indeed, this topic is of significant importance since it is the means of identifying the presence of these vehicles by visually impaired persons, and the correct detection within a safe distance is the only way to minimize possible accidents. The simulation of the sound emitted by these vehicles can be done using different methods, but in all cases the inclusion of details such as the directivity of the sound source emitting warning sounds (usually named the Acoustic Vehicle Alerting Systems - AVAS) is of utmost importance. The Boundary Element Method is one of the preferred methods to perform acoustic simulation, and is indeed very adequate also for this type of problems. The present chapter intends to present the BEM as a very good tool for this purpose. To overcome some limitations of the classic BEM, an “ACA-BEM” model is here described, and is complemented with adequate Green’s functions to allow the analysis of some simple configurations of urban environments. Some application examples are then presented regarding the sound pressure level distribution originated by a possible alerting system in an open street and in a street with a lateral rigid wall; an addition example is presented to illustrate the importance of possible obstacles in the propagation path of the alerting sound, such as the presence of parked vehicles, which indeed act as barriers.

4C.1 Introduction

From an urban environment point of view, one of main characteristics of an Electric Vehicle (EV) is its absence of mechanical noise, giving as a result very low sound pressure levels compared to conventional Internal Combustion Engine vehicles (ICE). But this noise divergence is highly influenced by the speed of the vehicle, on one

hand, the difference between the noise level of an EV and an ICE vehicle could be higher than 6 dB(A) at 10 km/h. However, if the speed is higher than 40 km/h, both types of vehicles emit similar sound pressure levels, due mainly to the tyre/road noise. But this characteristic is not thought to be always advantageous, the very low sound levels due to an approaching electric or hybrid vehicle, masked by the environmental noise, can be a danger to pedestrians and cyclists. The effect is even worse to children, elderly and blind people. Some previous studies demonstrated [1], on different background noise conditions, that the detectability of an EV is significantly lower than in a conventional ICE vehicles. Along these same lines, some other publications [2-4] reflect the problem of vehicle detection by visually impaired persons.

In order to tackle the problem, automotive manufacturers are boarding Acoustic Vehicle Alerting Systems (AVAS) on EV and HEVs. Regarding that, some specifications already exist. Japan issued guidelines defining the characteristics of warning sound in January 2010 and the United States approved legislation on December 2010. In 2011 the European Commission drafted a guideline for AVAS and, in 2016, it is expected to be approved the uniform provisions concerning the approval of Quiet Road Transport Vehicles with regard to their reduced audibility. This document will establish that the sound emitted by an EV shall be measured by a specific methodology in the speed range between 0 km/h and 20 km/h, as well as specifications on maximum and minimum sound levels emitted by the AVAS. Some other general characteristics are related with the frequency range. The main frequencies of the warning sounds should be within 200-1000 Hz and no sound should be emitted below 100 Hz. The optimal sound system for electric and hybrid vehicles includes three to four speakers- one in each corner of the car- but in principle, two loudspeakers would be enough as long as one directs sound forward and one backwards. However, there is expected any indication related with the sound directivity of the system, while it is true that it is going to be a relevant characteristic to optimise the detectability of the vehicle and minimise the annoyance and environmental impact.

This background information clearly indicates the necessity of performing in-depth research regarding the use of standardized AVAS in EV and HEV. In this contribution it is simulated the sound field produced by a mid-size sport utility vehicle, under different scenarios. In terms of the urban environment, both an open street and a street with a lateral rigid wall are considered. Regarding the vehicle, two scenarios are considered in terms of loudspeaker distribution, with one or two front-placed speakers. Complementarily, the effect of an obstacle (parked vehicle) is also analysed, introducing further complexity in the sound propagation patterns. The selected numerical method is the Boundary Element Method (BEM), which is particularly well suited for acoustic simulations, in which usually an extensive propagation medium exists around the radiating sources. However, standard BEM formulations can pose significant limitations regarding problem size, and special strategies must be used whenever larger problems need to be analysed. In the present work, an Adaptive-Cross-Approximation algorithm is used, as described [5], and previously applied by the authors [6].

4C.2 Governing equations for acoustic wave propagation

The propagation of sound within a three-dimensional space can be mathematically represented in the frequency domain by the Helmholtz partial differential equation as:

$$\nabla^2 p + k^2 p = - \sum_{k=1}^{NS} Q_k \delta(\xi_k^f, \xi) \quad \text{Eq. 1 - C}$$

where $\nabla^2 = \partial^2/\partial x^2 + \partial^2/\partial y^2 + \partial^2/\partial z^2$, p is the acoustic pressure, $k = \omega/c$, $\omega = 2\pi f$, f is the frequency, c is the sound propagation velocity within the acoustic medium, NS is the number of sources in the domain, Q_k is the magnitude of the existing sources ξ_k^f located at $(x_{\xi_k^f}, y_{\xi_k^f}, z_{\xi_k^f})$, ξ is a domain point located at (x_ξ, y_ξ, z_ξ) and $\delta(\xi_k^f, \xi)$ is the Dirac delta generalized function.

In the above defined Helmholtz equation, the Sommerfeld radiation condition $\lim_{x \rightarrow 0} [\partial p(X)/\partial n - ikp(X)] = 0$ is automatically satisfied at infinity, where X is the field point located at (x, y, z) , n is the unit outward normal vector and $i = \sqrt{-1}$.

Considering that a point source is placed within this propagation domain, at $X_0 = (x_0, y_0, z_0)$, it is possible to establish the fundamental solution for the sound pressure at a point X , at a distance $r = \sqrt{(x-x_0)^2 + (y-y_0)^2 + (z-z_0)^2}$, which can be written as:

$$G(\xi, X) = \frac{e^{-ikr}}{4\pi r} \quad \text{Eq. 2-C}$$

This simple fundamental solution can be further developed in order to account for some particular environmental configurations of the propagation medium. Considering an acoustic analysis, the presence of perfectly reflecting plane surfaces can be taken into account by using the well-known image-source method. In this technique, the effect of a point source in the presence of a given plane surface can be simulated by considering an additional virtual source, positioned in a symmetrical position with respect to the reflecting plane. Thus, following, for example, [7] if such plane is defined by $z = 0$, the corresponding Green's function can be written as

$$G_{half}(\xi, X) = \frac{e^{-ikr}}{4\pi r} + \frac{e^{-ikr_1}}{4\pi r_1} \quad \text{Eq. 3-C}$$

where $r_1 = \sqrt{(x-x_0)^2 + (y-y_0)^2 + (z+z_0)^2}$. The above expression is only valid if the plane is perfectly rigid, with a reflection coefficient of 1, although these expressions can be easily adjusted to include a different reflection coefficient. More complex configurations may also be simulated, as described in [7].

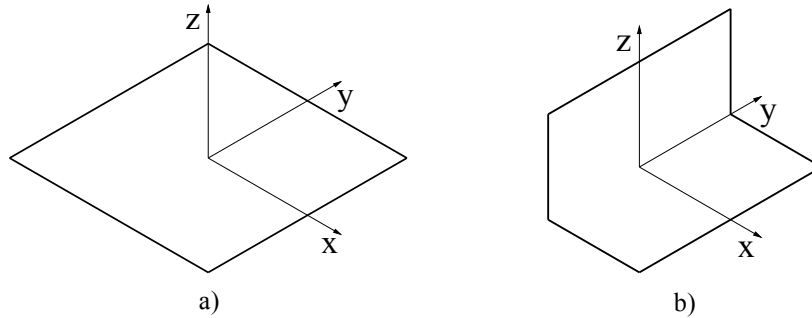


Fig. 1-C. Some simple configurations simulated using image-sources: a) half-space; b) quarter-space.

4C.3 The Boundary Element Method - BEM

The Boundary Element Method is a boundary technique, in which the relevant quantities and calculations are performed over the problem's boundary. To formulate the method, consider Green's Second Identity applied to Eq. 1-C, originating the following Classic Boundary Integral Equation (CBIE):

$$C(\xi)p(\xi) = -i\rho\omega \int_{\Gamma} G(\xi, X)v_n(X)d\Gamma - \int_{\Gamma} \frac{\partial G(\xi, X)}{\partial n} p(X)d\Gamma + \sum_{k=1}^{NS} Q_k G(\xi_k^f, \xi) \quad \text{Eq. 4-C}$$

where Γ is the boundary surface, ρ is the medium density, $G(\xi_k^f, \xi)$ is the incident field regarding the acoustic pressure generated by the real source placed at position ξ_k^f ; $p(X)$ and $v_n(X)$ represent the acoustic pressure and the normal component of the particle velocity at X , respectively. The coefficient $C(\xi)$ depends on the boundary geometry at the source point, and equals 0.5 for a smooth boundary.

For the case of exterior problems, it is known that equation 4-C provides unstable solutions at certain frequencies. Strategies have thus been developed in order to avoid this significant drawback, namely by means of its combination with the so-called Hypersingular Boundary Integral Equation (HBIE). To obtain this second equation, the first derivative with respect to the normal direction at the source point, n_L , must be considered, and the following equation arises:

$$-i\rho\omega\tilde{C}(\xi)v_n(\xi) = -i\rho\omega\int_{\Gamma}\frac{\partial G(\xi,X)}{\partial n_L}v_n(X)d\Gamma - \int_{\Gamma}\frac{\partial^2 G(\xi,X)}{\partial n_L\partial n}p(X)d\Gamma + \sum_{k=1}^{NS}Q_k\frac{\partial G(\xi_k^f,\xi)}{\partial n_L}$$

Eq. 5-C

As before, the coefficient $\tilde{C}(\xi)$ depends on the boundary geometry at the source point, and equals 0.5 for a smooth boundary.

It has been proposed by Burton and Miller [8] that combining the two equations 4-C and 5-C in the form

$$CBIE + i/k HBIE = 0$$

Eq. 6-C

originates a new boundary integral equation which provides unique solutions at all frequencies. Different boundary conditions may be prescribed at each boundary element, such as Dirichlet ($p(X) = \bar{p}(X)$), Neumann ($v(X) = \bar{v}(X)$) or Robin ($p(X)/v(X) = \bar{Z}(X)$, being $\bar{Z}(X)$ the acoustic impedance) boundary conditions. After prescribing such conditions, discretizing the boundary into NE_B segments, and establishing adequate interpolation functions within each segment (constant interpolation in the present work), a system with NE_B equations on NE_B unknowns can be assembled. Its solution makes it possible to obtain the acoustic pressure and the normal velocity at each boundary element, and consequently the pressure at any point of the domain can be computed by applying the boundary integral Eq. 4 - C.

4C.4 Adaptive Cross Approximation formulation

One of the most significant drawbacks of the classic BEM is the difficulty to address problems with a very large number of elements, and thus to tackle realistic engineering problems, without making use of additional mathematical strategies. Indeed, the BEM generates fully populated matrices, and the related memory requirements grow quadratically with NE_B . An estimation of the required computer memory in acoustic problems (with complex numbers and double precision) can be obtained simply as $memory(MB) = 16NE_B^2 / 1024^2$, and it is thus simple to understand that with as little as 10000 elements, 1.5 GB of RAM are required just for the system matrix. Fig. 2-C illustrates the growth of the memory requirements of the BEM with the number of nodes.

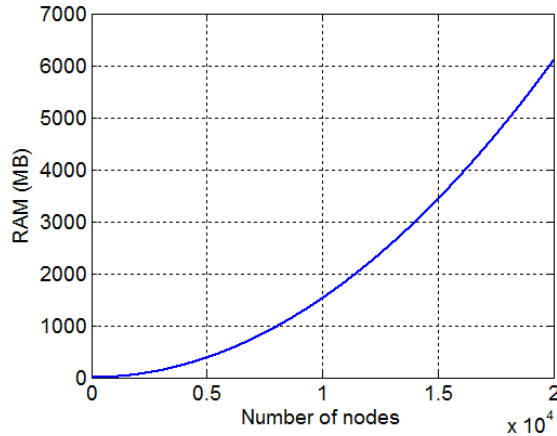


Fig. 2-C. Memory requirements of the classic BEM as a function of the number of nodes.

To overcome this difficulty, different strategies have been developed by the scientific community [5]. Among these, perhaps the most widely known is the Fast-Multipole method, which allows tackling problems with more than 1 million nodes. However, mathematically it involves some substantial changes to the way the BEM is implemented, and thus the reuse of existing codes is more difficult.

An interesting alternative for mid-sized problems is the use of the Adaptive Cross Approximation technique [5,6]. The Adaptive Cross Approximation (ACA) is based in hierarchical matrices (H matrices), an approach that allows for matrix operations with almost linear complexity. These matrices may be understood as an algebraic structure reflecting a geometrically motivated partitioning into sub-blocks, that in turn are classified to be either admissible or not. This block structure points out the fact that the H-matrix arithmetic is easily parallelizable. After having concluded the setup of each block, admissible blocks have to be approximated. The main advantage of ACA is that, for such approximation, it only requires the evaluation of some original matrix entries and the approximation is still almost optimal. Having a matrix $A \in C^{t \times s}$, the approximation is obtained as follow:

$$A \approx S_k = UV^T \quad \text{Eq. 7-C}$$

where $U \in C^{t \times k}$ and $V \in C^{s \times k}$. In this approximation k has a smaller rank when compared with t and s . This low-rank approximation can be obtained only for well-separated computational domains $x \neq y$.

To exploit the full advantages of such approach, it becomes necessary to solve the corresponding equation system by means of an iterative solver. In the examples presented here, the Generalized Minimal Residual Method (GMRES) iterative solver has been used, together with a block preconditioner (to accelerate convergence) based on the non-admissible blocks of the matrix.

4C.5 Sound field calculation around emitting vehicles

To illustrate the applicability of the described ACA-BEM in the analysis of the sound field around an emitting EV or HV, in this section a number of simple examples are presented. A very simple geometry of the vehicle is chosen just as an illustrative case, as depicted in Fig. 3-Ca.

In a first set of examples, let us consider a simple vehicle emitting a warning sound from a single frontal loudspeaker in an open street. The assemblage of the BEM system matrix is performed as described in the previous section, considering an ACA algorithm, in which admissible blocks are greatly compressed. Fig. 3-Cb illustrates the hierarchical matrix constructed for this purpose, where white patches correspond to admissible blocks (composing the vast majority of the matrix). Comparing BEM and ACA-BEM memory requirements, it can be stated that in ACA-BEM the required memory is reduced to 35%.

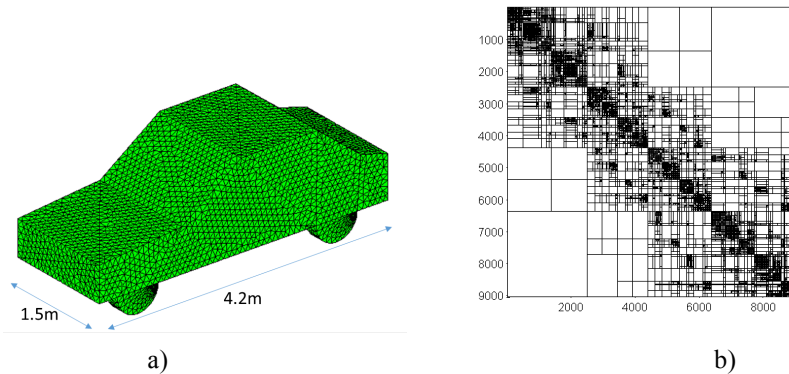


Fig. 3-C. Discretized vehicle using 9056 triangular boundary elements (a) and corresponding ACA-BEM hierarchical matrix representation (b).

For this geometry, sound pressure levels have been calculated considering the single loudspeaker to be placed in the front part, centred with the vehicle. In Fig. 4-C, the sound pressure levels in a plane parallel to the ground is illustrated for 250Hz, 500Hz, 750Hz and 1000Hz. It is clear that the increasing excitation frequency originates more intricate SPL maps, with the interaction between direct sound waves and the various reflections being responsible for this complexity. In addition, regions with very low SPL are visible at varying distances, which are generated by the interference between the direct waves and the first reflection on the rigid ground.

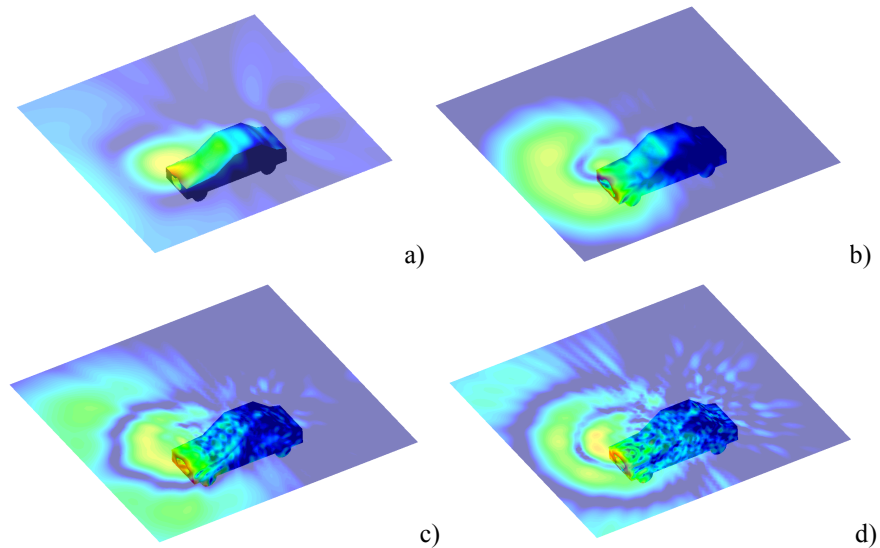


Fig. 4-C. Results for 250Hz (a), 500Hz (b), 750Hz (c) and 1000 Hz (d). Colour scale from 15 dB (dark blue) to 75 dB (dark red).

To have a better and clearer view of the observed behaviour, polar plots are depicted in Fig. 5-C, considering a distance from the front of the vehicle of 10 m, and for receivers placed 1.6 m above the ground. As stated in the introduction, the distance of 10 m can be considered as the minimum safe distance for vehicle detection by pedestrians, and thus it is worth a more detailed analysis.

The polar plots in Fig. 5-C evidence a distinct directivity pattern, varying with the excitation frequency. For lower frequencies, in spite of the presence of the rigid vehicle shadowing the source, relatively high SPL is reached for all angles, although with somewhat higher values in the front part (a difference of 5 to 10 dB). For higher frequencies, and as in Fig. 4-C, a more complex behaviour is observed. It is interesting to note, for the frequency of 750 Hz, a very significant distinction between the front and rear parts of the vehicle, with energy being more concentrated in the front part, as expected.

It is important to note that, in the previous simulations, the emitting source was assumed to be a point source placed near the front panel of the vehicle, approximately 0.1 m away from it. To better understand the influence of this simplification, a second set of simulations was performed embedding this source within the frontal panel, introducing a small semi-spherical cavity where the source is located. A detailed view of the corresponding BEM mesh is depicted in Fig. 6-Ca, and the computed polar plots, indicating the directivity of the system, are illustrated in Fig. 6-Cb, for a frequency of 750Hz. Comparing with the plots of Fig. 5-C, some differences are visible, particularly in what concerns the rear part of the vehicle, where less energy seems to be arriving; by contrast, in the front part, an increase in the SPL is visible, and was to be expected due to the more intense shadowing/baffle effect originated by the cavity where the source is now placed. Remarkably, the main features of the

directivity plot in the frontal part are almost exactly maintained, indicating that, for the purpose of evaluating the effect of the source in the front region, making use of the simpler approach of Fig. 5-C can be sufficient.

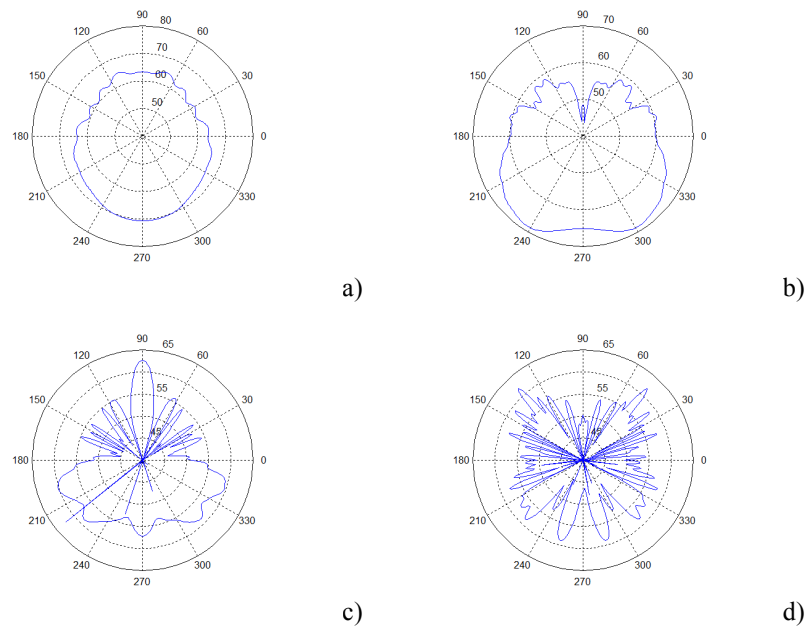


Fig. 5-C. Polar plots for 250Hz (a), 500Hz (b), 750Hz (c) and 1000 Hz (d).

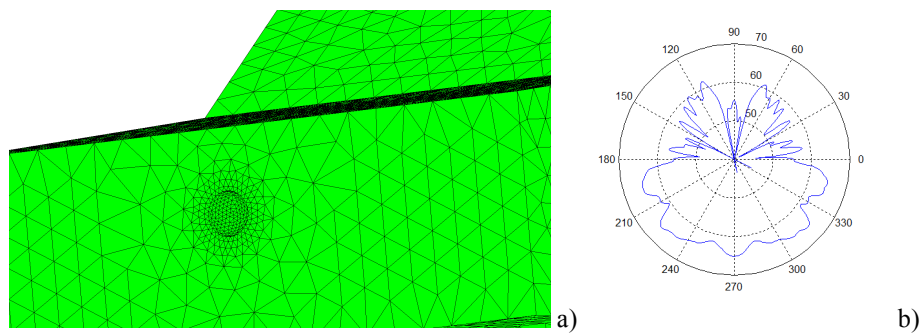


Fig. 6-C. Effect of considering the source embedded in the front panel: (a) detailed view of the BEM mesh and (b) polar plot for a frequency of 750 Hz.

In the previous examples, a single emitting speaker was considered in the front of the vehicle. However, it has been proposed by different researchers that better detectability may be obtained if more sources are placed emitting the warning sound.

In the plots of Fig. 7-C, the directivity pattern is compared in polar plots for situations with one and two acoustic sources emitting noise in the frontal part of the vehicle. As expected, the polar plot for the latter case indicates a more dense concentration of energy in front and to both sides of the vehicle; indeed, it is interesting to note that the directivity plot exhibits two broad lobes, one to each side of the vehicle, where significant and homogenous SPLs are attained, indicating that a significant area is illuminated by the emitting system.

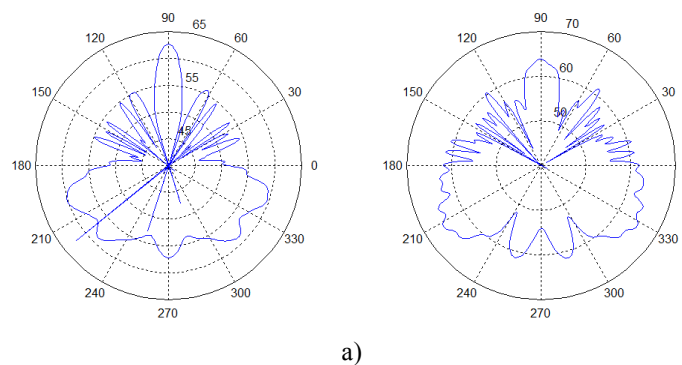


Fig. 7-C. Effect of one (a) or two (b) emitting sources in the front part of the EV, for 750Hz.

In what follows, two distinct situations, usually occurring in an urban environment, are now considered, namely the presence of a parked car (obstacle) and the presence of a rigid wall parallel to the street.

Let us start by analysing the effect of a right-sided parked vehicle, acting as a barrier to the propagation of the warning sounds emitted by the AVAS. Fig. 8-C illustrates both the SPL and the directivity polar plot for such situation. The SPL colour map of Fig. 8-Ca clearly indicates the existence of a shadow effect behind the parked vehicle, which, in practice, acts as a barrier to the propagation of sound waves. Observing the polar plot in Fig. 8-Cb, this effect is clearly seen, with a significant decrease of the energy reaching the region where pedestrians circulate. Although this decrease is largely dependent on the relative position of the two vehicles, the presented result gives a clear indication regarding a potential acoustic shadowing effect that may decrease detectability of the EVs.

Results in Fig. 9-C refer to the last analysed case, in which a rigid lateral wall is considered parallel to the street. Results for 1000Hz are illustrated. The results, presented in terms of SPL maps, indicate the presence of a reflected field coming from the rigid vertical wall, originating a more complex sound field. This reflection may enrich the sound field and may slightly increase the detectability of the vehicles by pedestrians. However, it must be stressed that this second wave is traveling from a direction opposite to the car (from the wall side and not from the street side), and can thus induce some confusion as to where the vehicle is situated (particularly in the case of visually impaired people). This behaviour merits a more in-depth study, and falls beyond the scope of the present chapter.

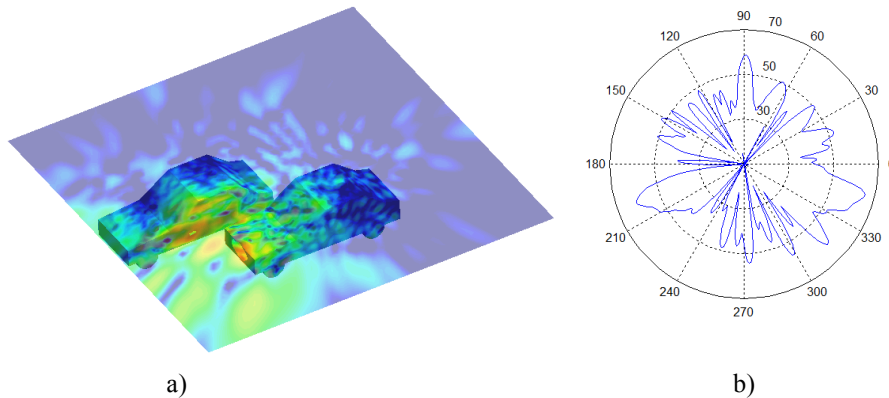


Fig. 8-C. SPL distribution (a) and polar plot (b) calculated in the presence of a parked car, for a frequency of 750Hz.

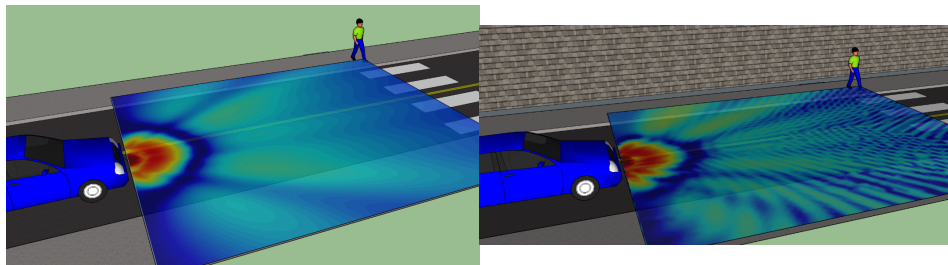


Fig. 9-C. SPL distribution calculated for a frequency of 1000Hz: a) open street; b) street with a rigid lateral wall.

4C.6 Final remarks

This chapter addressed the potential of modern numerical methods in the prediction of the sound field generated by circulating EVs and HVs in an urban environment. The specific case of the Boundary Element Method (BEM) has been focused, presenting its mathematical formulation and addressing a possible simple strategy adequate to allow tackling mid-sized problems (up to several hundred thousands of nodes). This, technique, the “ACA-BEM”, complemented with adequate Green’s functions, was here used to illustrate some numerical examples regarding the study of the effect of AVAS used in electrical and hybrid vehicles in an urban environment. Open and straight-shaped configurations and the presence of other vehicles (acting as barriers) were here illustrated. Although the objective of the chapter was just to illustrate the applicability of the numerical tool, it was also possible to draw interesting conclusions regarding the global acoustic behaviour of the system. It was observed that the effects of parked vehicles and the specific urban configuration can greatly influence the

capacity of pedestrians to detect circulating vehicles. To finish, it should be noted that further research in this topic is required, and objective quantification of the detectability of these vehicles deserves further attention.

4C.7 References

- [1] Garay-Vega, L., Hastings, A., Pollard, J. K., Zuschlag, M., & Stearns, M. D. Quieter cars and the safety of blind pedestrians: Phase I (No. HS-811 304) (2010).
- [2] Verheijen, E. Jabben, J. Effect of electric cars on traffic noise and safety. Report 680300009/2010. National Institute for public Health and the Environment Netherlander (2010).
- [3] Goodes, P., Bai Y. B., Meyer, E., Investigation into the Detection of a Quiet Vehicle by the Blind Community and the Application of an External Noise Emitting System. SAE International. 2009-01-21895 (2009).
- [4] Mendonça, C., Freitas, E., Ferreira, J.P., Raimundo, I.D., Santos, J.A. Noise abatement and traffic safety: The trade-off of quieter engines and pavements on vehicle detection. Accident Analysis and Prevention 51(2013) 11-17.
- [5] Liu Y. J., Mukherjee S., Nishimura N., Schanz, M., Ye, W., Sutradhar, A., Pan, E., Dumont, N. A., Frangi, A., Saez, A. Recent Advances and Emerging Applications of the Boundary Element Method. Appl. Mech. Rev. 64-3 (2012) 030802.
- [6] Godinho, L., Amado-Mendes, P., Santos, P. G., Cordeiro, M. An efficient and accurate numerical model for the 3D analysis of sonic crystals. 22nd International Congress on Sound and Vibration, Florence (2015).
- [7] Godinho, L., Costa, E., Santiago, J., Pereira, A., Amado-Mendes, P. 3D analysis of the sound reduction provided by protective surfaces around a noise source. International Journal of Acoustics and Vibrations 19-2(2014) 78-88.

Annex 4D

Equivalent material modelling of sandwich beam assemblies: propagating and evanescent wave considerations

Sophie de Rijk¹, Eugène Nijman¹

¹Virtual Vehicle Research Center, Inffeldgasse 21/A, 8010 Graz, Austria,
sophie.derijk@v2c2.at, eugene.nijman@v2c2.at

Abstract. An approach to modelling sandwich structures in bending with a homogenised equivalent material is presented. The dispersion of the layered system is brought to a Timoshenko behaviour, and an equivalent damping coefficient is derived. The equivalent model can then be implemented in finite element (FE) models by means of commonly used shell elements with transverse shear stiffness. A critical review of the limitations of such an equivalent material is made, specifically in relation to the evanescent parts of the dispersion, which are of importance in assembled structures. A benchmark case with specific boundary conditions is presented to demonstrate the strengths and weaknesses of the approach.

4D.1 Introduction

In an effort to build more fuel-efficient vehicles, high stiffness to mass ratio solutions for vehicle structures are being researched and used in the automobile, train and aerospace industries alike. This is in particular becoming critical for vehicles equipped with hybrid or electric powertrain in order for the additional weight of the battery cells and the auxiliary units to be leveraged. However, the introduction of light yet very stiff composite materials in automotive structures has an important implication on their vibro-acoustic behaviour. The high stiffness-to-weight ratio namely heavily impacts the structural dynamics and acoustical properties of these structures leading to novel, emerging noise, vibration and harshness (NVH) challenges. In particular, the air-borne sound insulation properties become very poor compared to conventional materials. This is due to the (i) high stiffness-to-weight ratio implying low coincidence frequency and (ii) the inherently low mass, which is however the governing parameter when it comes to air-borne insulation in the low frequency range. The resulting trade-off between the reduced weight and worsened NVH must be therefore accounted for. Furthermore, hybrid and electric vehicles exhibit an acoustic footprint different to that of vehicles equipped with conventional internal combustion engine, which implies specific requirements to be considered during the product development phase.

In this context, sandwich constructions have very promising characteristics as they present high bending stiffness for very low mass. Such structures however show a variety of types of behaviours over the range of frequencies in which they are excited during operation. Calculating their response by representing all their layers in FE

requires large computing power and time. For design and modelling purposes, specifically in FE, representing the multi-layered system with an equivalent single-layered material would make computing costs significantly lower and allow for much more flexibility during the development phase of vehicles. Since the aim is to set-up a methodology easily employable using commercial FE packages, making an equivalent material using Timoshenko beam theory would be a convenient choice as it can be implemented easily using shell elements. In this paper we first present a brief overview of existing methodologies for modelling sandwich structures with equivalent beams, including damping and shear modelling in laminates. Subsequently, an example case is presented and the issues and shortcomings of the approach are highlighted.

4D.2 State of the art in sandwich beams and plates dynamics

Many publications can be found on vibrations of sandwich beams and plates. Over the past few decades, researchers have strived to describe the vibrations in bending of sandwich structures using theories with complexities ranging from classic plate theory (Euler beam), first order shear (Mindlin for plates, Timoshenko for beams) to higher order theories. Several reviews concerning previous work on vibrations of laminates and sandwich structures already exist. We redirect the reader to, for instance, the review of Mallikarjuna and Kant [1] or that of Denli and Sun [2]. This section limits itself to giving some examples of typical approaches that can be found in the literature. For general orthotropic laminates, Yang, Norris and Stavsky [3] developed general equations of motion, assuming plane stress in each layer and first order shear theory for the global displacements of the plate. They then also simplify to classic plate theory by ignoring transverse shear and rotary inertia terms. The stress-strain relations of the laminate are obtained by integration of the properties of each layer over the cross section. Yu and Cleghorn [4] calculate the eigenfrequencies of simply supported symmetric sandwich plates by constructing the stiffness and mass matrices of the system following in turn the classic plate theory, the Mindlin plate theory and Reddy's third order plate theory. The stress-strain relations are calculated analogously to [3]. Lok and Cheng [5] obtain the various stiffness terms for a Mindlin plate from static stiffness calculations of a unit element of the sandwich structure and then calculate their eigenfrequencies assuming simply supported boundary conditions. Another approach, presented for instance by Mead [6], Zhou and Li [7], and Banerjee et al. [8], is to consider separately the motion of the face sheets and core, using different assumptions for each layer and then coupling the layers in one plate. Publications by Gaudenzi and Carbonaro [9] and Kant and Swaminathan [10] are examples of higher order theory applications. Backström [11] bases his work on the description of the behaviour of a sandwich beam described by Nilsson and Nilsson [12] to define frequency-dependent stiffness terms for either an equivalent Euler or Timoshenko beam.

Damping

When modelling a sandwich structure as a single material, the various loss factors of each layer need to be merged into a single equivalent loss factor. An often adopted assumption in the literature is that only shearing in the core is dissipative since it typically has higher damping but relatively low elastic modulus, see [6]. Sadasiva, Rao and Nakra [13] consider the core to be dissipative both in in-plane elongation and transverse shear motion and calculate a system loss factor as the ratio between the imaginary and real parts of the complex stiffness for simply supported beams. Maheri, Adams and Hugon [14] treat the case of a simply supported plate, considering damping for the in-plane elongation, in-plane shear and transverse shear motion. The in-plane stresses in the core and transverse shear in the face sheets are however neglected. Modal damping capacities are then obtained by solving the eigenvalue problem. Cremer, Heckel and Petersson [15] present a more generalised methodology to compute system loss factors of layered systems by defining it as the ratio of dissipated energy over potential strain energy per cycle.

Transverse shear stress distribution and correction factors

In the formulations given by the first order shear theory as well as the one given by Nilsson and Nilsson [12], the shear term D_s implies uniform shear stress distribution over the cross section. This is however inaccurate as the shear stiffness varies over the layers and a no-shear condition is required at the top and bottom surfaces of the beam. To account for this, a shear correction factor κ_s must be applied to D_s . In the case of beams with rectangular cross section and homogeneous material, the default reference shear correction factor applied in most FE packages (for example ABAQUS or NASTRAN) for shell elements is $\kappa_s = 0,833$ given by Reissner [16], assuming a parabolic stress distribution. Several authors have also addressed the issue of defining such a correction factor for laminates, see for example [17], [18], [19] and [20]. The shear correction factor is calculated such that the shear strain energy from the uniform stress/strain distribution and the actual stress/strain distributions are the same. The difference in the approach between the various authors lies in the assumptions on the actual stress distribution.

4D.3 From Nilsson sandwich beam to Timoshenko equivalent beam

For the work presented in this paper, the reference theory for the motion of a sandwich beam is taken from Nilsson and Nilsson [12]. This theory considers the total bending of the layup, the transverse shearing of the core and the individual bending of the face sheets about their own mid plane as well as global transverse and rotary inertias. The governing equations are then derived using the Hamiltonian approach:

$$-D_S \left(\frac{\partial^2 W}{\partial x^2} - \frac{\partial \psi}{\partial x} \right) + 2D_F \left(\frac{\partial^4 W}{\partial x^4} - \frac{\partial^3 \psi}{\partial x^3} \right) + \mu \frac{\partial^2 W}{\partial t^2} = 0 \quad \text{Eq. 1-D}$$

$$-D_{tot} \frac{\partial^2 \psi}{\partial x^2} + 2D_F \left(\frac{\partial^3 W}{\partial x^3} - \frac{\partial^2 \psi}{\partial x^2} \right) - D_S \left(\frac{\partial W}{\partial x} - \psi \right) + I_p \frac{\partial^2 \psi}{\partial t^2} = 0 \quad \text{Eq. 2-D}$$

where W the transverse displacement and ψ the rotation angle of the cross sections. From Eq. 1-D and 2-d and considering a general solution of the form $W = e^{i(\omega t - \kappa x)}$, a 6th order dispersion equation is obtained:

$$2D_F \kappa^6 + \left(D_S - 2 \frac{D_F}{D_{tot}} I_p \omega^2 \right) \kappa^4 - \left(\mu + 2 \frac{D_F}{D_{tot}} \mu + \frac{I_p D_S}{D_{tot}} \right) \kappa^2 \omega^2 - \frac{\mu D_S}{D_{tot}} \omega^2 + \frac{\mu D_S}{D_{tot}} \omega^4 = 0 \quad \text{Eq. 3-D}$$

where D_F is the individual bending stiffness of the face sheets, D_S the shear stiffness, D_{tot} the total bending stiffness, I_p the rotary inertia and μ the mass per unit length. The shear stiffness is considered to be simply that of the core, neglecting the contribution of the face sheets. We also point out here that in the original paper, no shear correction factor is considered. From Eq. 3-E we obtain three distinct wave numbers. In the undamped case, the first wavenumber κ_1 , is strictly real and represents the propagating part of the solution going from pure bending at low frequency to shearing in the mid-frequency range, then over to individual bending of the face sheets about their own mid plane in the high frequency range. The second wavenumber κ_2 , takes purely imaginary values in the lower frequency range and real values past a given limit frequency. Below the limit frequency, the second wavenumber represents a slowly decaying evanescent solution. Above the limit frequency, the solution is propagating. The third wavenumber κ_3 , is purely imaginary and is a very local exponential solution with a short decay. The various solutions of the dispersion relation (Eq. 3-D) are shown in Fig. 1-D.

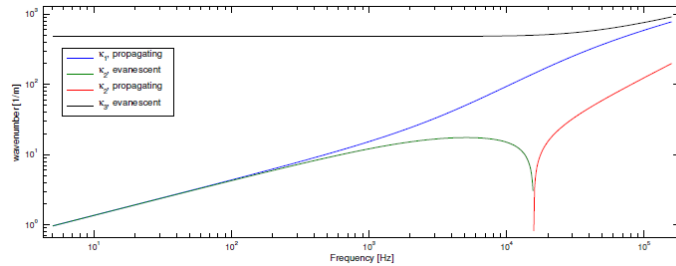


Fig. 16-D. Solutions to the dispersion relation following Nilsson and Nilsson [12] for a 15 mm thick aluminium sandwich beam with 1 mm face sheets

As mentioned in the introduction, we will model sandwich beams with an equivalent Timoshenko beam for which the governing equations are:

$$-D_{st} \left(\frac{\partial^2 W}{\partial x^2} - \frac{\partial \psi}{\partial x} \right) + \mu_t \frac{\partial W}{\partial t^2} = 0 \quad \text{Eq. 4-D}$$

$$-D_{bt} \frac{\partial^2 \psi}{\partial x^2} - D_{st} \left(\frac{\partial W}{\partial x} - \psi \right) + I_{\rho t} \frac{\partial^2 \psi}{\partial t^2} = 0 \quad \text{Eq. 5-D}$$

From which we obtain the following 4th order dispersion equation:

$$D_{st} \kappa^4 - \left(\mu_t + I_{\rho t} \frac{D_{st}}{D_{bt}} \right) \kappa^2 \omega^2 - \mu_t \frac{D_{st}}{D_{bt}} \omega^2 + \frac{I_{\rho t} \mu_t}{D_{bt}} \omega^4 = 0 \quad \text{Eq. 6-D}$$

where μ_t is the mass per unit length, $I_{\rho t}$ the rotary inertia, D_{st} is the transverse shear stiffness and D_{bt} the bending stiffness. We can then define an equivalent material by choosing an elastic modulus, shear modulus, density and total thickness such that $D_{bt} = D_{tot}$, $D_{st} = D_s$, $I_{\rho t} = I_p$ and $\mu_t = \mu$. We draw attention to the fact that, while all previous authors agree on matching the bending and shear stiffness and density, most authors define the thickness of the equivalent material (H_t) to be either the total thickness of the sandwich layup, or that of the core alone. We choose to match the rotary inertia instead, requiring the thickness of the equivalent material to be different from the total thickness of the layup:

$$\begin{cases} \mu_t = \mu \\ I_{\rho t} = I_p \end{cases} \longrightarrow H_t = \sqrt{\frac{12I_p}{\mu}}, \rho_t = \frac{\mu}{H_t} \quad \text{Eq. 7-D}$$

This choice is driven by the fact that, while the rotary inertia is typically too small to influence the propagating part of the solution κ_1 of the sandwich and Timoshenko beams, the κ_2 part of the solution is sensitive to the accuracy of I_p . As shown in Fig. 2-D, if I_p is not exactly matched (but the total thickness H_{tot} is), the transition frequency between evanescent and propagating solutions of κ_2 changes as well as the propagating κ_2 , compared to the sandwich dispersion.

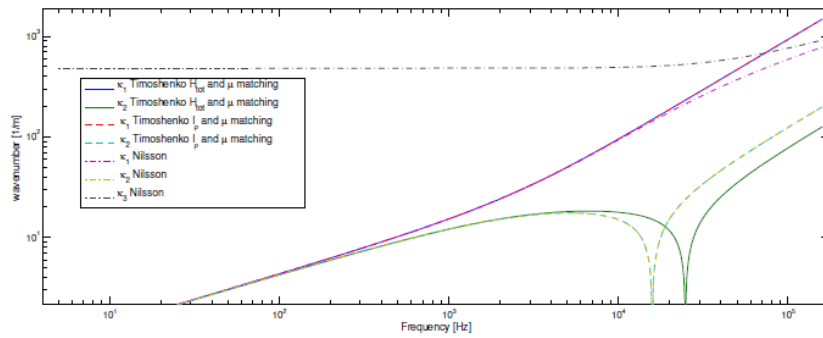


Fig. 17-D. Dispersion solutions for a 15 mm aluminium honeycomb sandwich beam with 1 mm face sheets compared to equivalent Timoshenko solutions either matching H_{tot} and μ or I_p and μ

Equivalent loss factor

When using shell elements in FE, one typically sets the damping with a single loss factor such that $E_t = E_t^*(1 + i\eta_{tot})$ and $G_t = G_t^*(1 + i\eta_{tot})$, where E_t^* and G_t^* are the undamped moduli. We therefore need to define a single equivalent loss factor from the various loss factors of the face sheets and the core. We follow the approach given in [15] where the total loss factor η_{tot} is calculated as the ratio between dissipated energy and potential strain energy:

$$\eta_{tot} = \frac{E_{diss}}{2\pi E_{pot}} \quad \text{Eq. 8-D}$$

We then consider the dissipative parts of the motion to be the elongation in the face sheets due to bending and the transverse shearing in the core:

$$E_{diss} = E_{dissL} + E_{dissS} = 2\pi\eta_f E_f h_f \left| \frac{d\epsilon_L}{dx} \right|^2 + \pi\eta_c G_c^* H_c |\gamma|^2 \quad \text{Eq. 9-D}$$

where h_f the thickness of the face sheets, H_c the thickness of the core and ϵ_L the longitudinal displacement of the face sheets due to bending, which can be expressed in function of the rotation of the cross section ψ : $\epsilon_L = \frac{H_c + h_f}{2} \psi$. γ is the shear angle given by: $\frac{\partial W}{\partial x} - \psi$. The strain potential energy is considered, as given in [12], to be the sum of the total bending energy, the individual face sheet bending energy of the face sheets and the transverse shear energy:

$$E_{pot} = \frac{1}{2} D_{tot} \left| \frac{d\psi}{dx} \right|^2 + D_f \left| \frac{d\gamma}{dx} \right|^2 + \frac{1}{2} D_s |\gamma|^2 \quad \text{Eq. 10-D}$$

Using the governing equations of the Nilsson sandwich beam, we can express γ in function of ψ . Considering the general solution of the form $\psi = e^{i(\omega t - \kappa x)}$, deriving by x is equivalent to multiplying by the wavenumber κ (we consider the propagating κ_1):

$$\frac{\partial \psi}{\partial x} \implies \kappa; \gamma \implies \frac{D_{tot}}{\mu \omega^2} \kappa^4 + \frac{I_\rho}{\mu} \kappa^2 - 1; \frac{d\gamma}{dx} \implies \frac{D_{tot}}{\mu \omega^2} \kappa^5 + \frac{I_\rho}{\mu} \kappa^3 - \kappa \quad \text{Eq. 11-D}$$

The total equivalent loss factor is then:

$$\eta_{tot} = \frac{\frac{1}{2} \eta_f E_f^* h_f (h_f + H_c)^2 \kappa^2 + \eta_c G_c^* H_c \left(\frac{D_{tot}}{\mu \omega^2} \kappa^4 + \frac{I_\rho}{\mu} \kappa^2 - 1 \right)^2}{D_{tot} \kappa^2 + 2D_f \left(\frac{D_{tot}}{\mu \omega^2} \kappa^5 + \frac{I_\rho}{\mu} \kappa^3 - \kappa \right) + D_s \left(\frac{D_{tot}}{\mu \omega^2} \kappa^4 + \frac{I_\rho}{\mu} \kappa^2 - 1 \right)^2} \quad \text{Eq. 12-D}$$

Slider-clamped beam numerical example

In the following, we calculate the response of a sandwich beam and its Timoshenko counterpart using the analytical formulations given in Section 3. All computations are implemented in MATLAB. For this numerical example, we choose to model a beam which is loaded by a unit force at $x = 0$ where a slider condition is assumed, so transverse motion W is allowed and is clamped at $x = L = 600 \text{ mm}$. The boundary conditions set for both beam theories are listed in Table 1-D.

Table 1-D. Considered boundary conditions

Nilsson	Timoshenko
$F(0) = 1$	$F(0) = 1$
$\psi(0) = 0$	$\psi(0) = 0$
$\frac{\partial W(0)}{\partial x} = 0$	
$W(L) = 0$	$W(L) = 0$
$\psi(L) = 0$	$\psi(L) = 0$
$\frac{\partial W(L)}{\partial x} = 0$	

The sandwich beam modelled is composed of 1 mm thick aluminium face sheets ($E_f = 70 \text{ GPa}$, $G_f = 0$, $\rho_f = 2730 \frac{\text{kg}}{\text{m}^3}$, $\eta_f = 0,01$) Following Nilsson [12], the bending stiffness is set as that of the whole laminate, the shear stiffness to be given solely by the core with no shear correction factor. The rotary inertia and density per unit length are also kept identical. The damping of the equivalent material is defined in two different ways. The first, which is only possible if we are computing the response analytically, consists in setting separately the loss factor of the face sheets (on the bending terms) and of the core (in the shear terms), identically to the sandwich formulation. It therefore represents a best case scenario. The second is defined following Eq. 12-D as a unique equivalent loss factor. Fig. 3-D shows the input mobility and dispersion solutions of the sandwich with its Timoshenko counterpart. Fig. 4-D then shows the force and moment transfer mobilities obtained in this case. While Fig. 3-D reflects the accuracy of the global response of the equivalent material, Fig. 4-D is meant to show how the boundary conditions are respected by the equivalent material

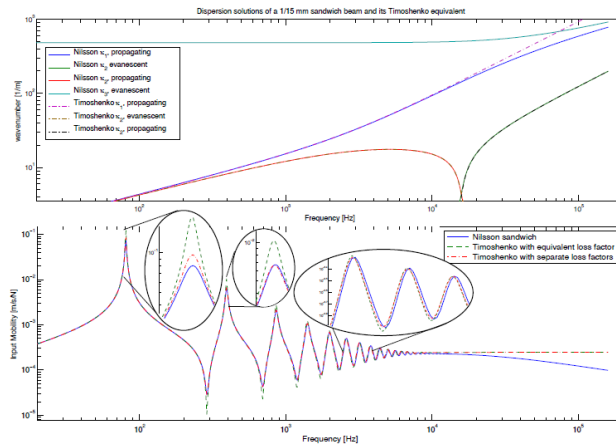


Fig. 18-D. Dispersion and input mobility for a 15 mm sandwich beam and its equivalent Timoshenko beam, with damping defined by separate loss factors or by equivalent loss factor

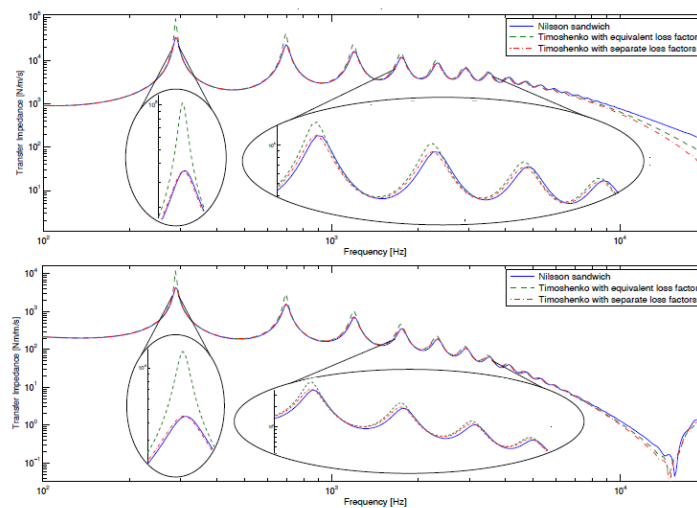


Fig. 19-D. Force (top) and Moment (bottom) transfer impedance between $x=0$ and $x=L$ for a 15 mm sandwich beam and its equivalent Timoshenko beam, with damping defined by separate loss factors or by equivalent loss factor

Firstly we notice from Fig. 3-D and 4-D alike that the equivalent material with the damping defined with separate loss factors follows very accurately the behaviour of the sandwich beam up to about $f \cong 3 \text{ kHz}$ (with the exception of the first peak value). Further on, a slight shift in the frequencies can be noticed (about 35 Hz shift at 3 kHz). The peak values however remain very close to the sandwich values (within 0.2 dB). At about $f \cong 6 \text{ kHz}$ the response given by the equivalent material starts to diverge clearly from the reference sandwich. Looking at the response of the equivalent material with the unique global loss factor, we notice that it clearly

underestimates the damping, but its accuracy improves as the frequency increases. The equivalent global loss factor is defined using only the propagating part κ_1 of the dispersion solution. At low frequencies however, the wavenumber of the evanescent κ_2 is of the same order of magnitude as that of the propagating solution κ_1 . This implies that the evanescent field affects the total displacement (and therefore dissipated energy) with similar wavelengths as the propagating solution. As the frequency increases, the wavenumber of the propagating solution increases, which means it increasingly dominates the total integrated dissipated energy, while the evanescent solution serves more as a local scaling. This is visible in both Fig. 3-D and 4-D, whereas frequency increases, the Timoshenko beam with the total equivalent loss factor starts to converge to the solution of its counterpart with the damping defined by parts. This observation highlights the importance of the evanescent field at lower frequencies and should therefore not be ignored. The influence of inaccurate damping is all the more striking in the force and moment transfer impedances. Another issue concerns the representation of shear stiffness. In the (common) case of thin face sheets, the assumption that the shear stiffness is only given by the core is reasonable. However, setting a shear correction factor of 1 is, in such cases, also inaccurate. The shear stress distribution in the laminate doesn't merely depend on the shear stiffness terms but also on the in-plane stiffnesses of the layers [17][18][19][20]. As the face sheets have high in-plane stiffness, their presence modifies the shear stress distribution. For the laminate considered here, the shear stiffness of the face sheets is of $h_f G_f = 2,63 \cdot 10^7$, that of the core is of $H_c G_c = 2,72 \cdot 10^6$, if one calculates the total shear stiffness following the approach of Madabhushi-Raman and Davalos [20] neglecting cross-plane (plate) effects, the total shear stiffness of the laminate becomes $D_s = 3,16 \cdot 10^6$. In this case, the difference in stiffness is of an acceptable 16%, but it clearly indicates that the face sheets do have an influence on the total shear stiffness. In order to be as generic as possible and cover a wide range of laminates from thinner to thicker face sheets, our methodology should include the face sheets in the computation of the shear stiffness. Simply adding up the stiffnesses is however clearly not an option, the actual stress distributions need to be considered via shear correction factors. If a fully generic approach is considered in which one would include the face sheet shear stiffness, an added complication then comes when considering damping. As shearing is then considered over both the face sheets and core, the energy dissipated in each part needs to be quantified separately. This requires defining multiple shear correction factors for the laminate, one for the face sheets, one for the core:

$$E_{diss} = E_{dissL} + E_{dissS} = 2\pi\eta_f E_f^* h_f \left| \frac{d\varepsilon_L}{dx} \right|^2 + \pi(2\kappa_{sf}\eta_f G_f^* h_f + \kappa_{sc}\eta_c G_c^* H_c) |\gamma|^2 \quad \text{Eq. 13-D}$$

where κ_{sf} and κ_{sc} are the shear correction factors in the face sheets and the core. These two shear correction factors can be obtained following the methodology given by Vlachoutsis [19] such that:

$$\kappa_s \sum_{i=1}^3 G_i h_i = \sum_{i=1}^3 \kappa_{si} G_i h_i \quad \text{Eq. 14-D}$$

were G_i , h_i and κ_{si} are the shear modulus, the thickness and the shear correction factor of each layer respectively.

4D.4 Conclusions

In this paper, the approach to building an equivalent Timoshenko beam for representing a sandwich laminate based on current knowledge is presented. The final aim is to accelerate FE calculations of sandwich structures using shell elements with equivalent material properties. Then, on the basis of a practical example, some of the challenges that need to be tackled with ongoing research to make a reliable and generically applicable equivalent model are highlighted. The main issue arising from this example is the proper definition of an equivalent loss factor to be applied to the equivalent material. It has been shown here that the latter depends not only on the propagating part of the solution, which is commonly considered by modelling simply supported structures (purely sinusoidal solution), but also the evanescent field, especially at lower frequencies. The necessity to compute the shear stiffness considering both the face sheets and the core as well as separate shear correction factors is also pointed out.

Acknowledgements

The research work of Sophie de Rijk has been funded by the European Commission within the Marie Curie program through the EID eLiQuiD project (GA 316422). The authors acknowledge the financial support of the COMET K2 - Competence Centres for Excellent Technologies Programme of the Austrian Federal Ministry for Transport, Innovation and Technology (BMVIT), the Austrian Federal Ministry of Science, Research and Economy (BMWFW), the Austrian Research Promotion Agency (FFG), the Province of Styria and the Styrian Business Promotion Agency (SFG). We also acknowledge the support of the COST action TU1105.

4D.5 References

- [1] Mallikarjuna and T. Kant, A critical review and some results of recently developed refined theories of fiber-reinforced laminated composites and sandwiches. *Composite Structures*, 23, 293–312, 1993.
- [2] H. Denli and J. Sun, Structural-acoustic optimisation of composite sandwich structures: A review. *The Shock and Vibration Digest*, 39 (3), 189–200, 2007.
- [3] P. Yang, C. Norris and Y. Stavsky, Elastic wave propagation in heterogeneous plates. *International Journal of Solids and Structures*, 2, 665–684, 1966.
- [4] S. Yu and W. Cleghorn, Free flexural vibration analysis of symmetric honeycomb panels. *Journal of Sound and Vibration*, 284, 189–204, 2005.

- [5] T.-S. Lok and Q.-H. Cheng, Free and forced vibration of simply supported, orthotropic sandwich panel. *Computers and Structures*, 79, 301–312, 2001.
- [6] D. Mead, A comparison of some equations for the flexural vibration of damped sandwich beams. *Journal of Sound and Vibration*, 83 (3), 363–377, 1982.
- [7] H. Zhou and G. Li, Free vibration analysis of sandwich plates with laminated faces using spline finite point method. *Computers and Structures*, 59 (2), 257–263, 1996.
- [8] J. Banerjee, C. Cheung, R. Morishima, M. Perera and J. Njuguna, Free vibration of a threelayered sandwich beam using the dynamic stiffness method and experiment. *International Journal of Solids and Structures*, 44, 7543–7563, 2007.
- [9] P. Gaudenzi and R. Carbonaro, An evaluation of higher-order effects on the eigenfrequencies of composite structures. *Composite Structures*, 47, 821–825, 1999.
- [10] T. Kant and K. Swaminathan, Analytical solutions for free vibration of laminated composite and sandwich plates based on a higher-order refined theory. *Composite Structures*, 53, 73–85, 2001.
- [11] D. Backström, Vibration of sandwich beams. Doctoral Thesis, KTH Stockholm, Sweden, 2006.
- [12] E. Nilsson and A. Nilsson, Prediction and measurement of some dynamic properties of sandwich structures with honeycomb and foam cores. *Journal of Sound and Vibration*, 251 (3), 409–430, 2002.
- [13] Y. Sadasiva Rao and B. Nakra, Vibrations of unsymmetrical sandwich beams and plates with viscoelastic cores. *Journal of Sound and Vibration*, 34 (3), 309–326, 1974.
- [14] M. Maheri, R. Adams and J. Hugon, Vibration damping in sandwich panels. *Journal of Material Science*, 43, 6604–6618, 2008.
- [15] L. Cremer, M. Heckl, B. Petersson, *Structure-borne sound: Structural vibrations and sound radiation at audio frequencies*, 3rd edition. Springer, Berlin Heidelberg, Germany, 2005.
- [16] E. Reissner, The effect of transverse shear deformation on the bending of elastic plates. *Journal of Applied Mechanics*, 12 (2), A69–A77, 1945.
- [17] J. Whitney, Shear correction factors for orthotropic laminates under static load. *Journal of Applied Mechanics*, 40, 302–303, 1973.
- [18] C. Bert, Simplified analysis of static shear factors for beams of nonhomogeneous cross section. *Journal of Composite Materials*, 7, 525–529, 1973.
- [19] S. Vlachoutsis, Shear correction factors for plates and shells. *International Journal for Numerical Methods in Engineering*, 33, 1537–1552, 1992.
- [20] P. Madabhushi-Raman and J. Davalos, Static shear correction factor for laminated rectangular beams. *Composites: Part B*, 27B, 285–293, 1996.

Annex 4E

NVH Simulation of Electric Drivetrains: SRM Case

Fabio Santos, Cassio Faria, Herman Van der Auweraer
Siemens Industry Software, Interleuvenlaan 68, 3001 Leuven, Belgium
Herman.vanderauweraer@siemens.com

Abstract. CAE-based optimization of electric drivetrains is a challenging task due to the interaction between electromagnetic, structural and acoustic effects. The electric motor noise generation problem is briefly reviewed and an integrated multi-physics approach is presented and applied to the case of a switched reluctance based drivetrain system. The baseline functional model that is used to calculate the structural loads for an FE-based NVH analysis of the motor is then used in a multiscale thermal model of the electric vehicle into which the motor is integrated. Two simulation examples illustrate the practical usability of the methods, one focusing on the NVH aspects and the other on the energy management.

4E.1 Introduction

In an effort to build more fuel-efficient With the electrification of road vehicles, several new design engineering challenges emerge. New components and subsystems such as battery and electric drive systems are introduced and performance parameters such as energy consumption get a new meaning because of the intrinsic range implications. The specific nature of these components and their vehicle integration requirements impose to critically investigate the design engineering process itself and explore new tools and approaches. Below, a CAE process for the electric motor is discussed.

Currently, the focus for designing electric drives primarily is on energy efficiency. Carmakers increasingly realize that this must be complemented by including the acoustic behaviour. Whereas indeed overall noise levels can be expected to be lower than the ones produced by internal combustion engines (ICEs), the sound quality is often compromised due to the high tonal nature of the generated noise, the effect of which can be aggravated by coinciding structural resonances. Vibro-acoustic simulation and analysis early on in the design cycle is a must to prevent these from happening, and to deliver customers high-quality products.

Specifically for reluctance machines, which offer an interesting drive system alternative due to their rare-earth free and mechanically simple design, the higher level of torque ripple significantly increases the acoustic emissions, which further aggravates the “annoyance” perception by the users. To address this issue and avoid corrective measures later in the product development process, it is important to incorporate vibro-acoustic analysis early on in the design process.

4E.2 Multiphysics modelling of an EM drivertrain

The multiphysics nature of the NVH problem is obvious. The primary drive principle relies on harmonic electromagnetic forces which are generated when rotor and stator are unaligned. These forces have a radial and a tangential component, as illustrated in Fig. 1-E. For operational purposes, the tangential component is the most interesting one, as it produces the power.

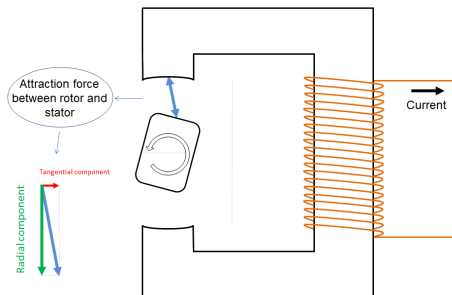


Fig. 1-E. Electromagnetic forces as generated in a SRM.

The radial component is absorbed in the rotor and the stator, and transformed in an elastic deformation. These forces may lead to structural vibrations, which finally produce a pressure field that is radiated from the motor outer surface to the surroundings or is transmitted through the connections with the supporting structure. This process is illustrated in Fig. 2-E, showing the interaction between the different physical domains.

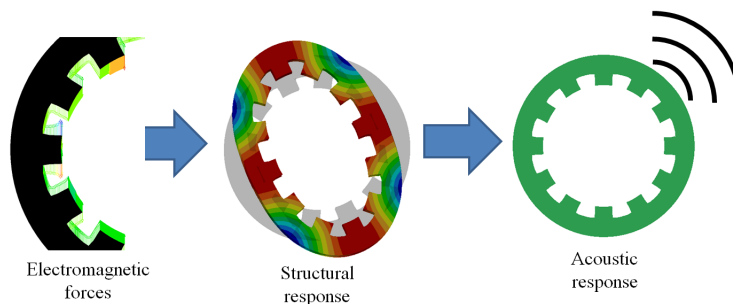


Fig. 2-E. Multiphysics vibro-acoustic model of an electric motor

The modelling and simulation of such a complex process hence requires using a set of different tools and lots of expertise in the multiple fields to appropriately capture the phenomena. A very important characteristic that, to some extent, simplifies the problem at hand is the weak two-way coupling between the domains, i.e. there is a unidirectional flow of “information” between domains. For example, while the

vibration of the structure produces pressure waves in the air surrounding the motor, these same waves have little or no effect on the vibration of the structure.

Different approaches can be followed to build the multiphysics simulation model. Through a connection of Electromagnetic and structural Finite Element models, the transient EM forces can be processed to structural responses for each relative position of rotor and stator. This allows to estimate the structural and vibro-acoustic response of the stator. Important considerations relate to the correct functional connection of system variables, but also the correct connectivity between the electromagnetic and the structural meshes. For example, the EM mesh has a higher refinement close to the air gap because the phenomenon there dominates the system dynamics, meanwhile the refinement for the structural mesh is concentrated near the smaller section of the structure. (Fig. 3-E).

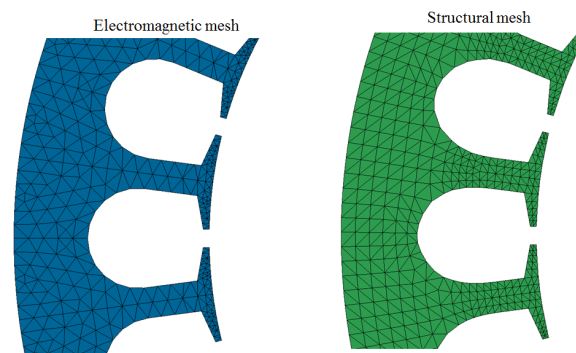


Fig. 3-E. Direct comparison between two example meshes used for electromagnetic and structural simulations

Alternatively, through the use of a 1-D system model, the electromagnetic position dependent forces can furthermore be processed to time domain torque and torque ripple profiles and current and efficiency values. The resulting multilevel modeling approach can then be used to study structural but also thermal/energetic system responses and even the motor controller design. The model can furthermore be integrated in a complete vehicle model that includes other components of the powertrain such as the battery, a combustion engine in case of a HEV, and also other energy consumers and heat producers, like HVAC, the inverter, and cabin thermal models. In this way, driving cycles and scenarios can be simulated such that a global power consumption prediction can be performed, cooling systems can be designed and typical motor operating conditions can be derived.

The same detailed functional model can also be used to calculate the phase currents which, using an electromagnetic FEM model, yield the radial stator forces at each rotor position (and time step). After transformation to the frequency domain and application to a structural model, surface accelerations and hence acoustic contributions can be calculated, leading to a noise, vibration and harshness (NVH)

model. Consequently, the result of the defined modeling approach is that the design parameters for the motor, the cooling system and the motor control can be linked to multiple vehicle performance parameters. Fig.4-E shows the overall scheme of this modeling approach.

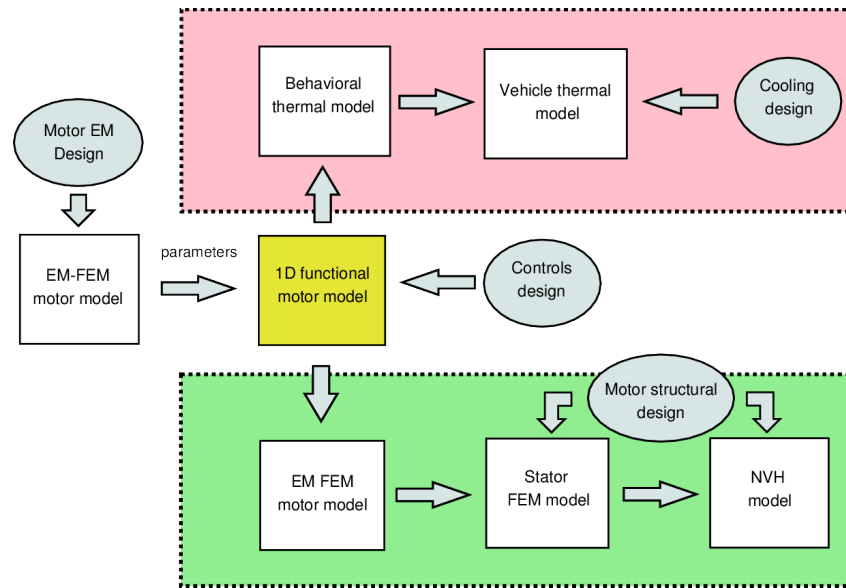


Fig. 4-E. Multiscale SR motor model for full vehicle integration

The discussion will further focus on the latter approach and is illustrated for the specific case of the design and vehicle integration of a Switched-Reluctance (SR) electric motor. Such SR-based drive systems gain interest because of their robust and low-cost designs and the absence of the need of rare earth materials. To develop such motors, it is a prerequisite to take into account from the start not only component performance specifications, but also the vehicle integration and vehicle performance requirements.

4E.3 The Switched Reluctance Motor

The switched reluctance motor (SRM) is a type of synchronous machine, but with particular features - the stator windings make use of field coils, but no coil or magnetic material is present on the rotor. The motor works by energizing two opposing stator poles, generating a magnetic field. This magnetic field forces the rotation of the closest rotor poles to the position of minimum reluctance, aligning them to the stator poles. Fig. 5-E shows the energizing and alignment of the stator and rotor poles. By energizing consecutive stator poles, continuous rotation is generated

on the rotor. The SRM functionality and modeling is thoroughly explained in [1]. The switched reluctance motors are usually referred to by their number of stator and rotor poles - hence, Fig. 5-E represents an 8/6 SRM (8 stator poles and 6 rotor poles). The way that each phase is energized, also referred to as turn-on and turn-off angles or firing angles, is an important part of the motor activation. The proper synchronization of the phase currents with the rotor position minimizes torque ripple [2] and helps reduce current peaks and consequently copper losses.

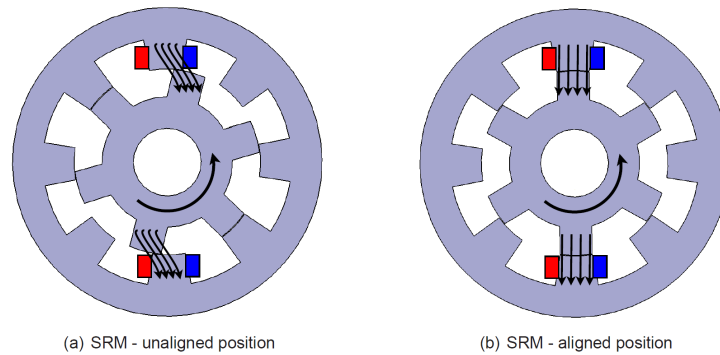


Fig. 5-E. Switched reluctance motor functionality

4E.4 Motor Functional Model

The switched reluctance motor is a non-linear system mainly due to the non-linear inductance profile, leading to a non-linear torque equation [3]. Analytical solutions for modeling of the SRM exist [4], but a more detailed and precise model can be obtained by the use of look-up tables containing the non-linear inductance profile and other important magnetic characteristics. Look-up tables give the best results overall and for this reason they were chosen as the method to represent the 1D 12/8 SRM system. To obtain the magnetic characteristics for this virtual model, an electromagnetic finite element model can be used [5] such as the freeware Finite Element Method Magnetics (FEMM) software [6] or the commercial software JMAG. Such model uses the stator and rotor geometry and material magnetic properties, as well as the coil characteristics such as the number of wire turns, to obtain the steady state system response (Fig. 6-E), from which magnetic flux and torque can be extracted for a given rotor angular position and current.

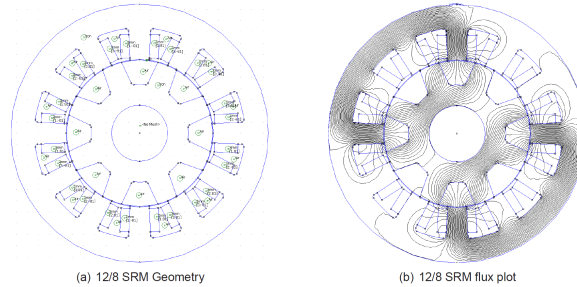


Fig. 6-E. SRM electro-magnetic finite element modeling - (a) stator and rotor geometry; (b) magnetic flux plot

This procedure is repeated obtaining flux and torque for a discrete range of current and rotor position values that cover the whole operating range of the SRM [7]. Since each phase individually has the same behavior for a given current and relative rotor position and assuming that magnetic flux superposition is true for all cases, the look-up table data can be extracted only for a single phase and replicated for the other ones.

Once the look-up tables are obtained, the complete functional model can be implemented, including models for controls, power electronics, loads, activation angles and losses. The 1-D functional model was developed in the software LMS Imagine.Lab AMESim [8], [9], a 1-D multi-domain simulation software that allows for interactions between mechanical and electrical domains and is very suitable for the simulation of FEV and HEV, integrating different physical domains. Fig.7-E shows the 12/8 SRM system with 3 half-bridge converters and activation angle control.

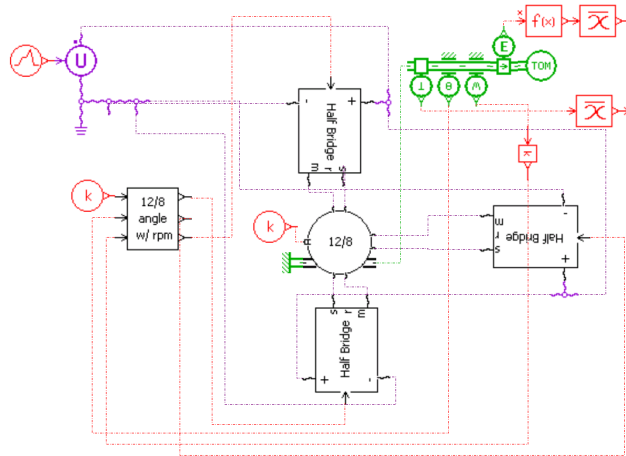


Fig. 7-E. 1-D functional model of a 12/8 SRM with half-bridge converters and controlled firing angles

4E.5 NVH Model

The acoustic contribution of the electric motors on FEV's and HEV's must be predicted as early as possible in the design phase. The dominant cause of noise generated from the electric motors is considered to be the stator vibrations caused by radial forces [11][11]. The radial magnetic forces in the air gap between rotor and stator teeth excite vibrations that are transferred through the structure to the external surface of the motor and through the air.

Basically, the SRM noise prediction can be divided in 3 consecutive parts: (1) calculation of stator radial forces; (2) vibration or structure-borne transmission of the forces; (3) noise generation. By using the detailed 1-D model described above, one can calculate the phase currents and motor rotor position of a given working or load condition. This data is used in the 2-D magnetic FE model of the motor to determine the magnetic forces in the air gap acting on the stator teeth. These forces are surface density and volume density magnetic forces, but the latter can be neglected [12]. This procedure is done for only one full rotation, given that the motor is working on steady state conditions. The resulting forces are then transformed to the frequency domain.

Subsequently, the structural modes of the stator are calculated by means of finite element method. Fig. 8-E shows the first 10 structural vibration modes of the 12/8 SRM stator. These vibration modes are used together with the magnetic forces generated previously to calculate a modal-based forced response, which consists of the surface accelerations of the stator based on the magnetic forces excitation. Finally, the calculated accelerations are the boundary conditions to be used with the Boundary Element Method (BEM) direct method, used for exterior problems.

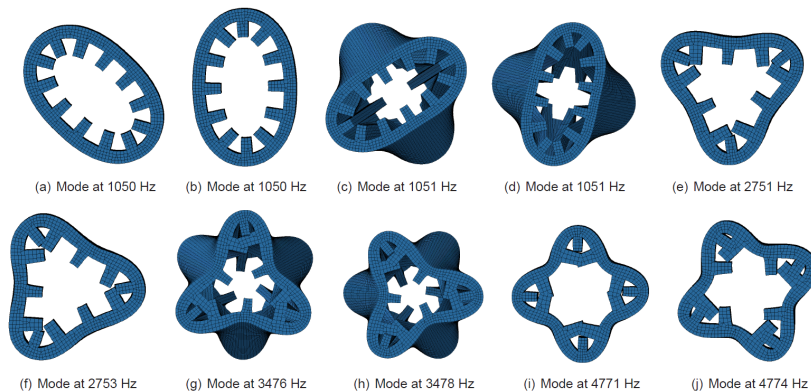


Fig. 8-E. Ten first vibration modes of a 12/8 switched reluctance motor stator

The whole process of the acoustic prediction methodology is summarized in Fig.9-E. Each step of shows the system inputs that can be modified. In the first step, the most important inputs are the material and coil magnetic properties, as well as the stator

and rotor geometry. For the 1-D simulation, the most important parameters are the different control strategies that can be implemented, together with different load conditions and/or operation cycles. The third step of the process is where the force calculations take place, and on the last part of the process, the most important inputs are the structural properties of the motor stator, which can affect directly the sound pressure levels around the motor.

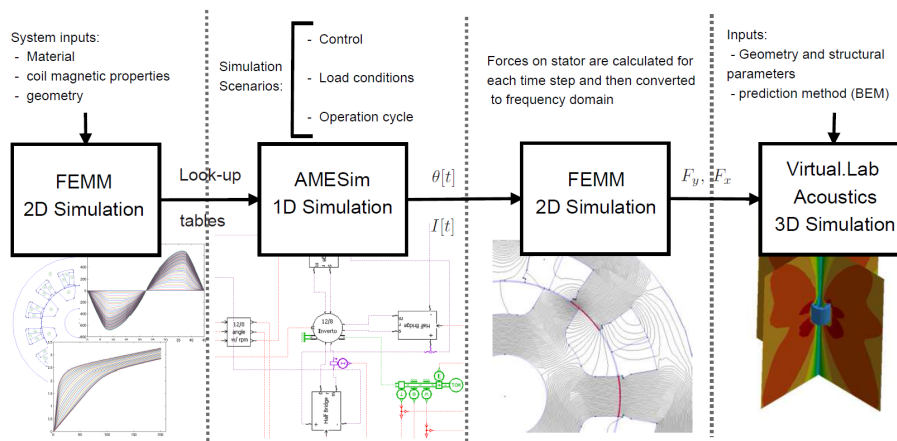


Fig. 9-E. Acoustic prediction diagram

4E.6 Energy Model

The investigation and simulation of the global energy consumption of the FEV's and HEV's is an important stage in the development of these vehicles [13]. By estimating the different system losses it is possible to dimension adequately the vehicle's systems, such as motor and cabin cooling or battery power consumption, based on the operating conditions. Similarly, the vehicle powertrain characteristics can be evaluated before prototyping, based on suitable driving cycle scenarios. To obtain a computationally efficient simulation system for the global energy flow, a simpler motor model has to be used, providing the simulation with just the necessary data needed for the losses computations. This behavioural model contains data that can be extracted from a more detailed motor model, as discussed above, or from real measurements.

Three look-up tables are used in this simpler model: (1) Maximum motor torque in function of input voltage, rotary velocity and temperature, (2) Maximum generator torque in function of input voltage, rotary velocity and temperature, (3) Motor losses in function of torque, rotary velocity and temperature. The tables containing the maximum motor and generator torque can easily be obtained using the detailed functional model by running it under different conditions of rotary velocity, input voltage and temperature. The average torque is extracted from the system and the

tables can be created. To obtain the losses table, a submodel was created, dividing the losses in 3 different types - copper losses, core losses and mechanical losses [14]. Copper losses are generated when the current goes through the coil, iron losses are related to the magnetic flux that passes through iron (stator and rotor) and mechanical losses are generated from friction. Thereafter the 3 tables can be utilized in the SRM behavioural model that is included in a global electric vehicle system specially designed to verify the system's energy flow. The complete energy flow model of this electric vehicle is seen in Fig. 10-E. **Source du renvoi introuvable.**

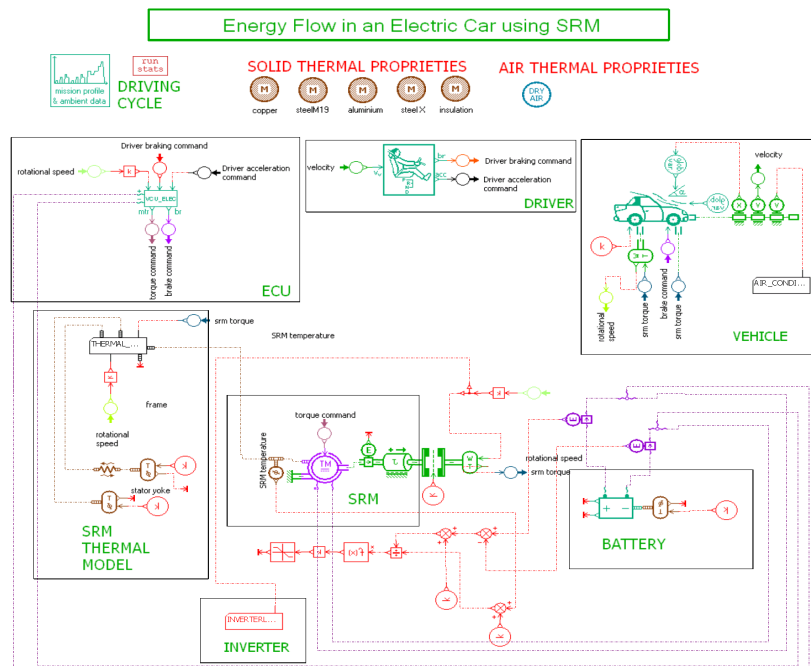


Fig. 10-E. AMESim model of an electric vehicle with energy flow management

The Driver, ECU and Vehicle subsystems are used to simulate braking and acceleration commands, as well as simple translational dynamics for the whole vehicle, given a constant load. The Vehicle subsystem also includes an air-conditioning model that is able to regulate the cabin temperature. Benchmark driving cycles consisting of input velocities are used to simulate different operating conditions.

The switched reluctance motor and its thermal subsystems - inverter, battery and the SRM itself - are used to compute the temperature and energy losses in the different component parts. To model the temperature distribution in the SRM, a lumped thermal model of the SRM was used based on a thermal equivalent circuit for the temperature distribution in the motor. The motor is divided into several thermal parts: frame, stator yoke, stator teeth, rotor core, rotor teeth, coil windings and lateral

windings, axial shaft, bearings, internal air and air gap [15]. The whole thermal network is shown in Fig. 11-E.

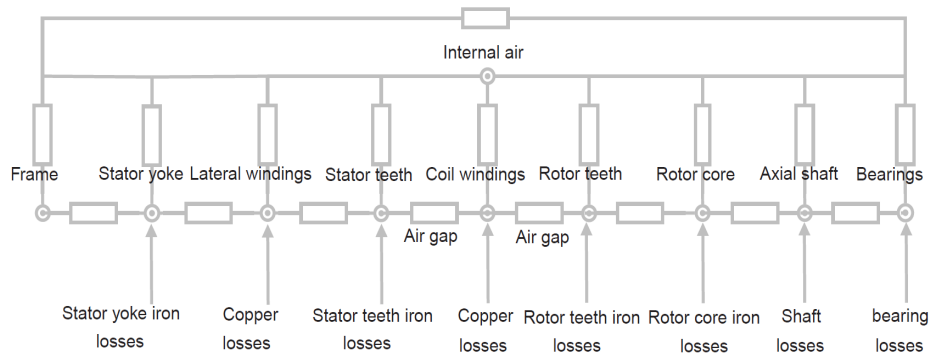


Fig. 11-E. SRM thermal network

The thermal component of the SRM also allows to connect the cooling system. Two inputs that are connected directly to the frame and stator yoke allow to create a thermal network representing the cooling system and the effect on the motor temperature can be visualized on the motor itself. The inverter losses are modeled as a half-bridge with two types of components - diodes and transistors - and the losses are also divided into two types - conduction and switching losses [16]. By using the motor rotational velocity as input, the switching losses are calculated, and the conduction losses are calculated based on peak and average current values.

Losses on the battery are estimated with a model that takes into account the internal resistance of the battery, as well as the open circuit voltage.

4E.7 Simulation Examples

Two simulations were carried out to verify both the NVH model of the SRM and the vehicle thermal model of the electric vehicle.

Acoustic Analysis

Following the procedure described above, an acoustic prediction of the SRM was carried out for two working conditions. The firing angles which are very important in the SRM with respect to maximum and minimum current and torque production were chosen as parameters to be investigated in view of their effect on the sound pressure levels produced by the motor. The two cases chosen were: firing angles optimized to maximize torque and firing angles optimized to maximize torque and minimize mean current levels. The objective was to evaluate if, by minimizing the coil current, a significant improvement on the acoustic quality of the SRM could be realized, due to the reduction of the magnetic field amplitude and hence the forces exciting the stator teeth. The parameters used for the 1-D and 3-D simulations are shown in Table 1-E. To control the torque generated by the motor, a simple PI controller was used, and the

chosen rotary velocity was guaranteed by attaching an auxiliary motor to the SRM shaft.

Table 1-E. Acoustic Simulation Specifications

Parameter	Value
Rotational speed	6000 RPM
Torque	30 Nm
Minimum frequency	200 Hz
Maximum frequency	3500 Hz

A Boundary Element sound prediction method was used, allowing the use of field point meshes, to visualize the system's spatial response. Fig. 12-E shows the sound pressure levels of the two simulation cases for a planar field point mesh of 1.2m by 1.2m at 1604 Hz.

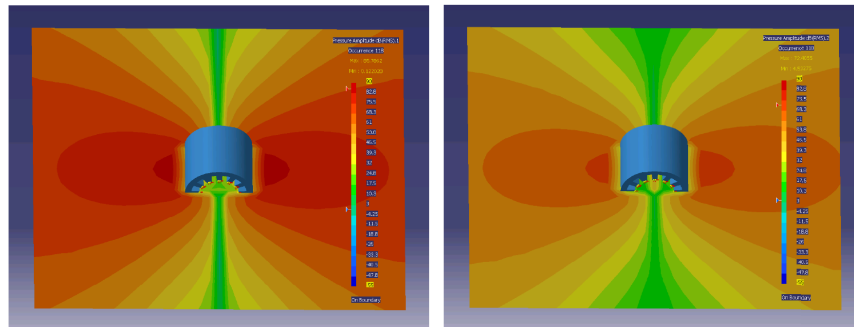


Fig. 12-E. Comparison of the sound pressure levels of the two simulation cases at 1604 Hz - (a) SRM with firing angle optimization with regards to torque (b) SRM with firing angle optimization with regards to torque and current

To assess the acoustic response over the whole frequency range, a spherical field point mesh was used to obtain the average value of the acoustic power over all points around the stator. Fig. 13-E shows the acoustic power responses of both simulations.

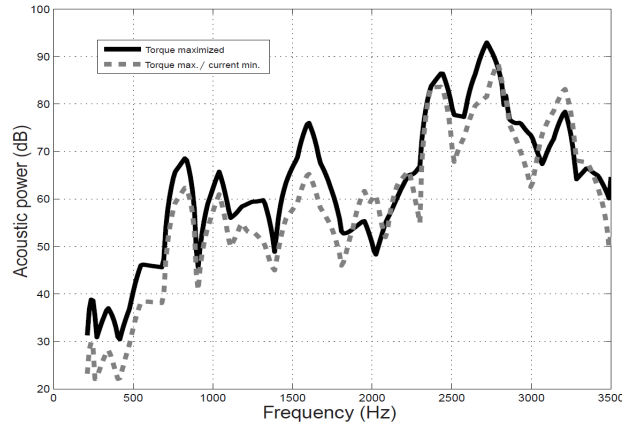


Fig. 13-E. Comparison of the acoustic power response of a 12/8 SRM at 6000 RPM and 30 Nm torque - two firing angle strategies: (—) System response with maximized torque in respect to the firing angles (---) System response with maximized torque and minimized current with respect to the firing angles

The simulation results show a clear difference between the acoustic properties in the two cases. The minimization of the current has an important effect on the acoustic power response of the SRM. However, on some frequency ranges the system with current minimization has higher acoustic power levels. This happens because the current levels at that particular frequency band are higher, even though the mean current levels are lower for that case.

Electric Vehicle Energy Management Simulation

To evaluate and test the global vehicle model, two simple cooling scenarios were used, one with cooling fluid temperature at 35 °C and one at 45 °C. Both scenarios consider the use of a hypothetical cooling jacket to cool the SRM frame. The objective is to observe the motor temperature with respect to the cooling fluid temperatures. This sort of procedure can be very helpful on determining the optimal specifications of the cooling circuit of the motor, so that on one hand the motor temperature is kept within operational limits, and on the other hand no overdimensioning of the cooling circuit is done. The simulations use the New European Driving Cycle (NEDC) as the operational conditions. This driving cycle contains both an urban driving cycle and an extra-urban driving cycle, relating to city and highway driving modes, respectively, with total duration of 1180 seconds. The vehicle velocity (Km/h) in function of the total driving cycle time for the NEDC is shown in Fig. 14-
Erreur ! Source du renvoi introuvable.

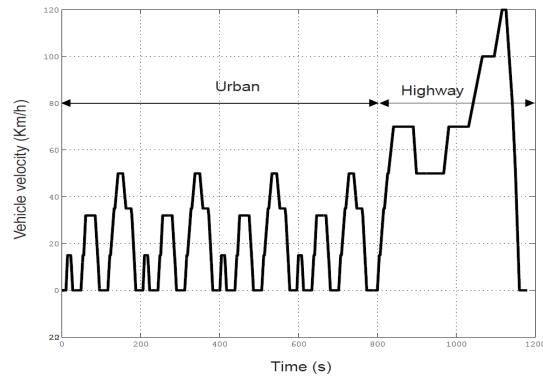


Fig. 14-E. New European Driving Cycle used for the global electric vehicle simulation, with urban and highway cycles

The main motor and system losses (total SRM losses, copper, iron and mechanical losses, battery and inverter losses) for both simulation scenarios are shown in Fig. 15-E.

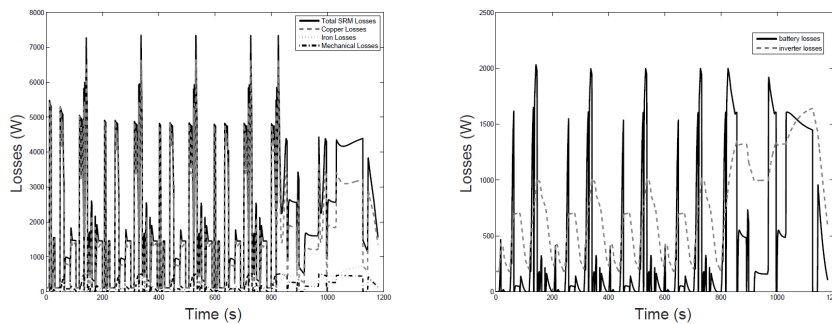


Fig. 15-E. Integrated electric vehicle system losses simulation results. Left: total SRM losses, iron losses, mechanical losses. Right: Battery and inverter losses

The temperature rise in the SRM is mainly caused by the heating of the copper windings. Consequently, the windings and stator teeth are the most critical part to be monitored in the SRM. To verify the effectiveness of the cooling circuit, the temperature rise was observed on the two critical parts plus on the stator yoke, which is in direct contact with the frame and the cooling circuit. **Erreur ! Source du renvoi introuvable.** 16-E shows the temperature rise for both simulation scenarios - cooling fluid and jacket at 45 ° C and at 35 ° C

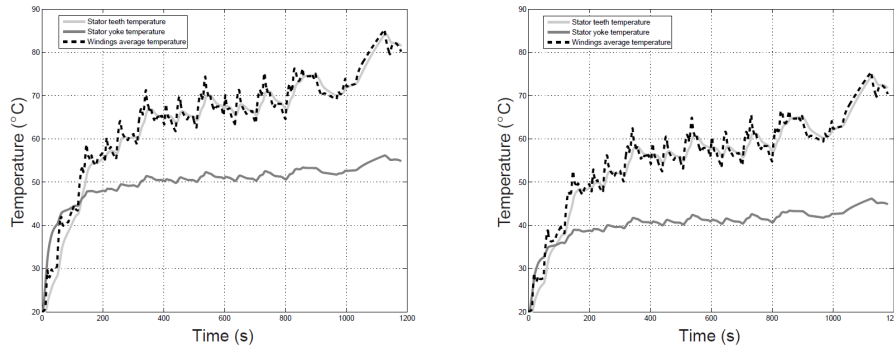


Fig. 16-E. Temperature rise on a NEDC cycle, analyzed at critical points of the Switched Reluctance Motor - stator yoke, stator tooth and coil windings. Left: results for cooling fluid of 45°, right cooling fluid of 35°

Analyzing both simulation scenarios, the difference of the temperature values in the SRM parts can be clearly seen. The temperature on the coil windings is well influenced by the cooling circuit.

4E.8 Conclusion

A multiphysical system model was developed for studying the acoustic and thermal behaviour of an electromotor. A detailed functional model was created by means of an integrated approach that uses magnetic finite element modeling to generate look-up tables that contain the non-linear inductance profile and magnetic torque characteristics. These tables are the basis for a 1-D simulation model that yields the torque, phase currents and rotor position. Based on this model, two applications were realized: an NVH prediction approach to compute sound pressure levels around the motor and a global electric vehicle system model to compute losses and thermal management.

The modeling approach was applied to the case of an SRM motor. It was shown how the control setting of the motor can affect the radiated sound. The structural parameters of the stator are also relevant, and can be modified to verify the benefits in the system. Furthermore, trade-offs can be investigated so that the optimal parameters can be chosen based on system specifications. In a second application, the behavioural motor model was used in an energy management system calculation. Using the detailed functional model, peak values that could otherwise go unchecked are taken into account, leading to more realistic results. The thermal properties of the motor can be evaluated, such as the main source of heat and/or losses, and how the material properties affect the distribution of the energy. Two examples show how the motor cooling system specifications can be defined based on driving cycle simulations.

Acknowledgement

VLAIO, the Flemish Agency for Innovation, is acknowledged for their financial support in the SRMOTIF project and Flanders' Drive for their financial support with the Electric Powertrain project.

4E.9 References

- [1] R. Krishnan. *Switched Reluctance Motor Drives: Modeling, Simulation*. CRC Press, 2001.
- [2] C. Mademlis and I. Kioskeridis. Gain-scheduling regulator for high-performance position control of switched reluctance motor drives. *Industrial Electronics, IEEE Transactions on*, 57(9):2922–2931, 2010.
- [3] S.M. Lukic and A. Emadi. State-switching control technique for switched reluctance motor drives: Theory and implementation. *Industrial Electronics, IEEE Transactions on*, 57(9):2932–2938, 2010.
- [4] W. Ding and D. Liang. A fast analytical model for an integrated switched reluctance starter/generator. *Energy Conversion, IEEE Transactions on*, 25(4):948–956, 2010.
- [5] K. Mhatli and B. Ben Salah. Improved modeling of switched reluctance motor including mutual and saturation effects. In *MELECON- 15th IEEE Mediterranean Electrotechnical Conference*, pages 1470–1475. IEEE, 2010.
- [6] H. Kuss, T. Wichert, and B. Szvmanski. Design of a high speed switched reluctance motor for spindle drive. In *Compatibility in Power Electronics, 2007. CPE'07*, pages 1–5. IEEE, 2007.
- [7] N.H. Fuengwarodsakul, R.W. De Doncker, and RB Inderka. Simulation model of a switched reluctance drive in 42 v application. In *Industrial Electronics Society, 2003. IECON'03. The 29th Annual Conference of the IEEE*, volume 3, pages 2871–2876. IEEE, 2003.
- [8] R. Meillier, T. Rozier, A. Brizard, and D. Almer. Optimization of vehicle energy management through multi-domain system simulation. In *Transport Research Arena Europe*, 2010.
- [9] L. Broglia, M. Ponchant, and R. Meillier. Balancing vehicle energy performance with drivability and thermal comfort: benefits of a multi-domain system simulation approach in the case of an electric-hybrid vehicle. In *25th World Electric Vehicle Symposium and Exposition*, 2009.
- [10] J. Florentin, F. Durieux, Y. Kuriyama, T. Yamamoto, M. DeBruin, S. Jordan, J. Han, G. Barber, Q. Zou, X. Sun, et al. Electric motor noise in a lightweight steel vehicle. *Analysis*, 1:1062, 2011.
- [11] J.O. Fiedler, K.A. Kasper, and R.W. De Doncker. Calculation of the acoustic noise spectrum of srm using modal superposition. *Industrial Electronics, IEEE Transactions on*, 57(9):2939–2945, 2010.
- [12] M. van der Giet, E. Lange, DAP Correa, IE Chabu, SI Nabeta, and K. Hameyer. Acoustic simulation of a special switched reluctance drive by means of field–circuit coupling and multiphysics simulation. *Industrial Electronics, IEEE Transactions on*, 57(9):2946–2953, 2010.

- [13] V.P. Atluri, K. Koprubasi, and N.D. Brinkman. Analytical evaluation of propulsion system architectures for future urban vehicles. In *Advanced Hybrid vehicle Powertrains*, 2011.
- [14] M. Woon, X. Lin, A. Ivanco, A. Moskalik, C. Gray, and Z.S. Filipi. Energy management options for an electric vehicle with hydraulic regeneration system. In *Advanced Hybrid vehicle Powertrains*, 2011.
- [15] H. Rouhani, J. Faiz, and C. Lucas. Lumped thermal model for switched reluctance motor applied to mechanical design optimization. *Mathematical and computer modelling*, 45(5-6):625–638, 2007.
- [16] MH Bierhoff and FW Fuchs. Semiconductor losses in voltage source and current source igbt converters based on analytical derivation. In *Power Electronics Specialists Conference, 2004. PESC 04. 2004 IEEE 35th Annual*, volume 4, pages 2836–2842. IEEE, 2004.

Annex 4F

CAE Approach to Electric Vehicle Warning Sound System Design

Bert Van Genechten, Koen Vansant, Herman Van der Auweraer
Siemens Industry Software, Interleuvenlaan 68, 3001 Leuven, Belgium
Herman.vanderauweraer@siemens.com

Abstract. Electric vehicles need to be equipped with a sound generation system to warn vulnerable road users of their presence, in particular at low speeds. Next to generating the right sound, also the actual sound system needs to be designed and configured in order to have a maximal effect. A numerical simulation approach was developed and applied to the case of bumper integration of a steerable sound source.

4F.1 Introduction

A topic that is increasingly considered as a critical noise performance for electric/hybrid vehicles is the relation between the exterior sound of quiet road vehicles and the safety of Vulnerable Road Users (VRU). In particular at low speeds, before the tire noise becomes observable, the absence of any perceived engine noise and hence the absence of any vehicle proximity warning, may cause danger to other road users.

Perceptual considerations for the sound design [1], [2], [3] lead to considerations regarding harmonic and narrow/broadband spectral content, speed dependency and modulations. To be relevant at potential VRU listener positions, the propagation of the sound from source to receiver has to be considered, taking in to account the influences of the surrounding structure and space (car body, road, road obstacles, road layout...) and taking into account the masking effect from the traffic noise (Fig 1-F). A proper system configuration needs to identify the number of sources, the source characteristics and the optimal source locations.

A numerical simulation approach was hetero investigated and applied in the design of a transducer array to be installed on the bumper of the eVADER vehicle [1], [2]. eVADER was an EU funded research project in the FP7 framework in which the problem of warning sound generation to protect vulnerable road users was investigated, leading to the installation of a prototype system on a demonstrator vehicle. Such simulation models allow assessing more realistically the impact of the system integration on the performance of the warning system [4]. Using the acoustic responses obtained with these models, the strategy selected ifor the source design is verified. Next, a sensitivity study is presented to assess the impact of the most critical changes in the vehicle's acoustic environment: temperature changes, changes in the road surface properties and the influence of nearby scattering objects such as e.g. parked vehicles.

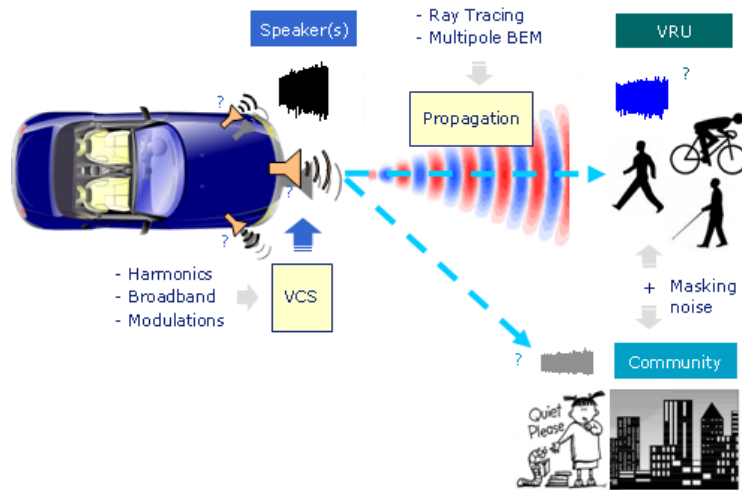


Fig. 1-F. Vehicle Warning Sound design challenges and synthesis model

4F.2 CAE Tools for exterior warning sound design

Simulation Approach

Whenever virtual prototypes are used for design support or performance evaluation, the selection of a suitable discretization approach and analysis type is key. When considering acoustic radiation problems, which involve solving an uncoupled exterior acoustic problem with imposed normal velocity boundary conditions in the frequency domain two families of numerical models are frequently used in the current engineering practice. The Boundary Element Method (BEM) is based on a boundary discretization and is hence very suited to model acoustic radiation.

Moreover, significant advances such as the Fast Multipole BEM methods [5], [6], [7] and the Hierarchical Matrix (or H-Matrix) solvers [8] have been made in the BEM's computational efficiency. The Finite Element Method (FEM) has become the standard solution approach for solving interior acoustic and vibro-acoustic problems. Different strategies for coping with this limitation have been devised such as infinite elements and perfectly matched layer (PML) approaches [9] applied on fictitious outer FEM boundaries. Based on the strengths and weaknesses of the different modelling approaches a combination of different strategies is proposed for this design study. For scenarios where only the bumper itself needs to be considered, the FEM-AML technique which is based on the PML approach is selected.

Integration Study

A detailed geometrical model of the front bumper of the eVADER demonstrator vehicle is incorporated in the numerical models in this design study. The front of the car is approximated by extruding the outer edge of the surface model in the length direction (Fig. 2-F). Due to their small size, the six individual loudspeakers are

incorporated as the six red circular vibrating pistons shown in the left. To finalize the creation of the FEM-AML model, the pre-processing capabilities of the LMS Virtual.Lab Acoustics [10] suite of numerical tools are used to automatically generate a suitable convex wrapper mesh around the extended bumper geometry. The right side of Fig. 2-F shows the final baseline FEM-AML model with an average mesh size such that it is at least valid up to 1.3kHz according to commonly used rules of thumb. The total computational cost for solving this baseline FEM model of 120.000 degrees of freedom is 9 seconds per frequency. In comparison, solving an equivalent H-matrix BEM model takes 210 seconds while providing similar acoustic predictions.

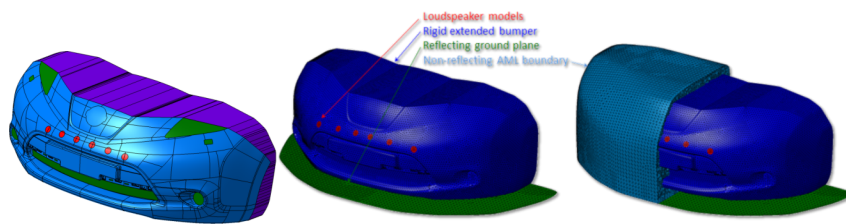


Fig. 2-F. (left) Computational bumper geometry, (right) FEM-AML model of the warning signal generator

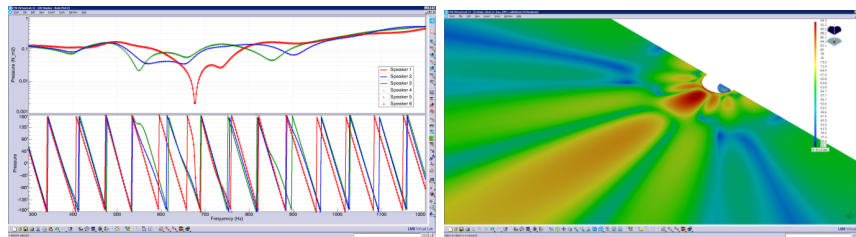


Fig. 3-F. Acoustic pressure responses obtained with the baseline FEM-AML model: (left) individual acoustic transfer functions for the six speakers, (right) forward-facing acoustic beam at 900Hz

The FEM-AML model of the warning signal generator installed on the front bumper is used in two steps:

- Firstly to obtain the acoustic transfer functions between the surface velocity of each individual loudspeaker and the acoustic pressure at a number of semi-circular microphone arrays. These transfer functions are used as an input for the beam forming strategies. An example of such transfer functions is shown in the left of Fig 3-F.
- Secondly, by introducing the optimal beam forming control parameters in the numerical model, the acoustic pressure generated by the warning generator can be reconstructed. This information is useful to assess the impact the warning generator has on the environment noise landscape.

Design Sensitivity Study

Given the high level of exposure of the exterior warning system to a range of environmental conditions it is important that the dominant parameters are taken into account during the design of the system to ensure robustness. Based on a literature review the following parameters have been found to influence the propagation of acoustic waves in typical traffic environments: (i) Variations in the acoustic properties of the air that may be caused by the presence of temperature gradients or variations in relative air humidity, (ii) Aerodynamic disturbances of the propagating medium caused by wind gradients and air turbulence, (iii) Impact of second order reflections that may interfere with the direct field generated by the array such as the presence of reflecting objects and ground reflections and (iv) Interference with other noise sources that can be other sound sources in the environment or incoherent background noise. In the current study, the first and third class of influencing factors were considered. The fourth impact type is implicitly integrated into the total warning system that automatically selects a suitable absolute sound level to be generated.

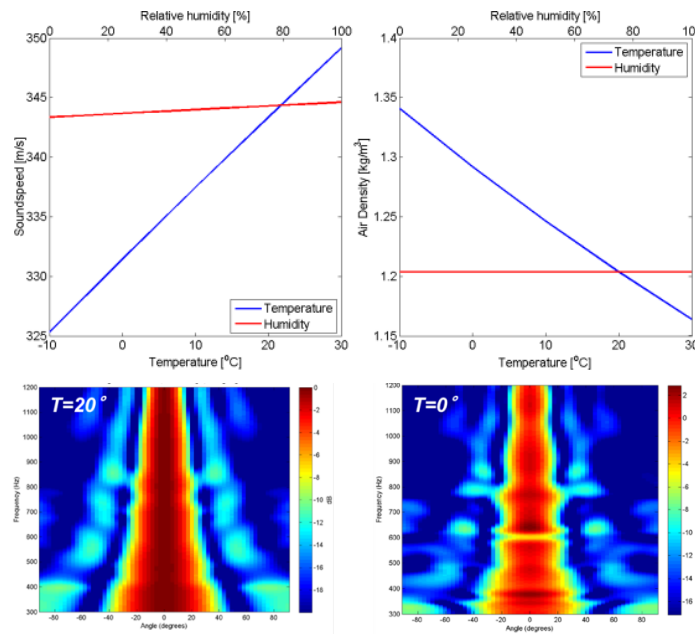


Fig. 4-F. Impact of temperature and humidity on speed of sound and density (*upper*) and on beam forming (*lower*)

Both the ambient temperature and the air's relative humidity change the acoustic wave propagation properties and hence may significantly impact the warning system's performance. In order to identify the most influential parameter, Fig. 4-F shows the evolution of both density and sound speed for representative temperature (-10°C to +30°C, blue curves) and humidity (0 to 100%, red curves) ranges. The curves clearly show that the temperature has the most impact. Since temperature changes

only impact the acoustic material properties of the ambient fluid, the selected FEM-AML technique remains valid. By combining these updated models with the control coefficients computed for the reference conditions, the robustness with respect to ambient fluid property changes is assessed. The right side of Fig. 5-F shows a representative example result of this study for a warning signal targeted at a 0° orientation at 20°C and at 0°C . A very good agreement between the obtained directivities can be observed.

A second parameter with a major impact on the warning system's performance is the acoustic absorption of the road surface. Apart from attenuating acoustic waves, the acoustic impedance of the road surface may also introduce asymmetry or even fully scatter the warning signal. In order to incorporate these effects a description of the frequency-dependent acoustic normal impedance is incorporated in a discretization of the road surface. In [11] a theoretical model was developed in which the acoustic surface impedance depends on the ambient fluid properties and also on the air flow resistivity and porosity of the asphalt. Typical values for these quantities were taken from literature. Since the exterior warning system is designed to warn at-risk VRUs up to large distances in front of the vehicle, the road surface should be appropriately modelled. Hence, the area where the road surface is located is modelled explicitly for a scenario where the vehicle is driving along a 20m long straight road which is two lanes wide, as is shown in the left of Fig. 5-F. Additionally the impact that scattering objects in the vicinity of the warning signal generator is considered. To this end, the BEM model is extended by adding a model of two vehicles parked on the side of the road 5m in front of the approaching demonstrator vehicle. The vehicles themselves are considered to be perfectly reflecting and their additional impact on the spatial distribution and directivity of the acoustic warning signals will be assessed. The increased extent and complexity of the problem setting significantly impacts the choice of the modelling approach. Based on the model size (around 190.000 degrees of freedom for the road surface and 250.000 when including the parked cars) the H-matrix BEM was selected. Due to the increased computational cost (around 13-25 min per frequency of interest), the acoustic responses are only computed every 25Hz.

The right side of Fig. 5-F shows the spatial distribution of the acoustic pressure amplitude generated by the warning system at 600Hz for a steering angle of 0° . This case is considered as the worst possible mode of operation since the central acoustic pressure amplitude lobe of the warning signal impinges directly on both stationary vehicles. As can be seen in the contour plots, the presence of the two vehicles shields the areas behind them as expected. The sound waves that are scattered by the vehicles do interfere with the central lobe of the warning signal but do not alter its shape nor do they generate areas of very low SPL.

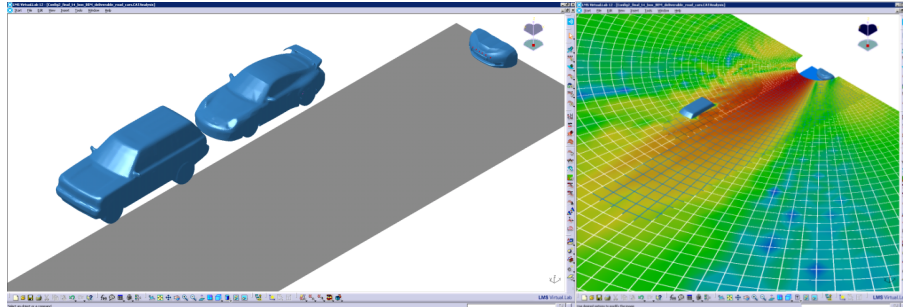


Fig. 5-F. Impact of road surface impedance and nearby scattering objects on beam forming performance: (left) H-matrix BEM model discretisation, (right) spatial distribution of the acoustic pressure field at 600Hz

The conclusions above for the spatial pressure distributions at discrete frequencies are confirmed by the directivity analysis presented in Fig. 6-F. On the left side the directivity obtained for the baseline problem setting is given. This is compared to the directivity for a 0° steering where only the road surface impedance (middle) and where both the road surface and the two parked vehicles (right) are included in the analysis. In both cases, the directivity pattern becomes asymmetric due to the asymmetric positioning of the vehicle with respect to the road (it occupies the right lane). Additionally the interference between the direct radiated acoustic field and the acoustic waves scattered by the parked vehicles is clearly visible in the image on the right but as was observed in Fig. 5-F these interferences do not distort the overall directionality and hence they do not impact the system's intended operation.

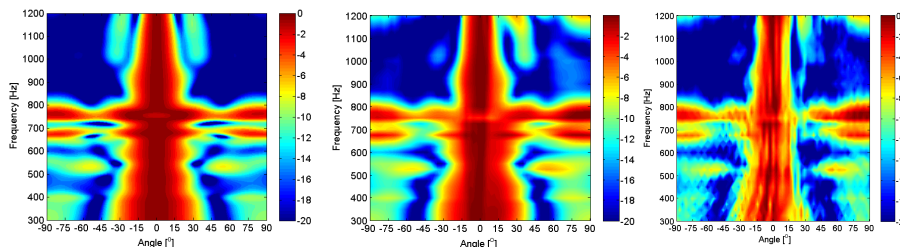


Fig. 6-F. Impact of road surface impedance and nearby scattering objects on beam forming performance: (left) reference configuration, (middle) impact of 20m long asphalt road, (right) impact of asphalt road and parked cars

4F.3 CAE Tools for interior warning sound design

Additional to warning the vulnerable road users, also the driver needs to be alerted of the presence of such road users. Detection systems such as pedestrian detection and obstacle warning systems become available and their input can be used to generate an appropriate warning signal to the driver. Such systems should provide clear information about the diagnosed risk, allowing the driver to take appropriate action.

In this design, both acoustic and visual warnings are merged to achieve optimal driver alertness and to support his or her decision making. For the acoustic diver warning, the use of the existing vehicle audio system to provide intuitively correct sensational information on the detected threat situation was explored through a simulation-based acoustic configuration analysis approach towards interior warning systems, more specifically, to investigate the generation of direction feeling on the interior warning sound so as to optimally provide information on the detected direction of the threat situation (generation of a so-called “phantom source” correlated to the VRU). These simulations which are based on Ray Tracing and binaural auralization have provided inputs regarding optimal speaker configuration and control (including optimal use of already available audio systems through pre-filtered acoustic warning signals). The digital filter design process is shown schematically in Fig. 7-F.

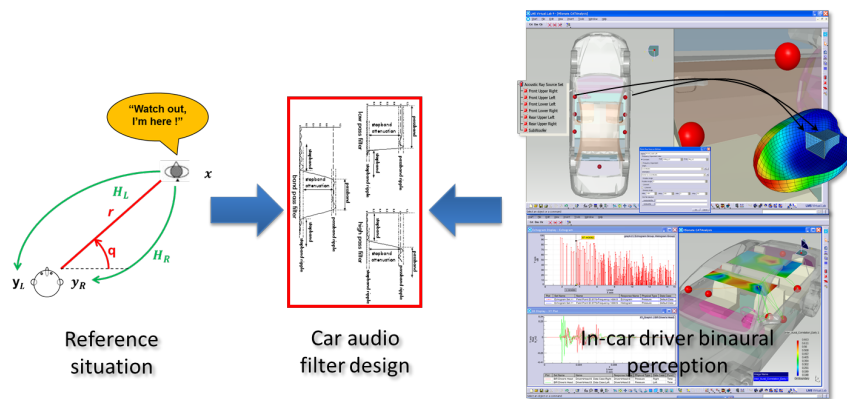


Fig. 7-F. Simulation-based interior warning system design.

4F.4 Conclusion

A CAE-based analysis and evaluation is proposed to support the design of the an acoustic exterior warning system. In this process, advanced acoustic beam forming algorithms are linked to high-fidelity numerical models for the assessment of the acoustic radiation of the different transducers as installed on the vehicle. In this way, a thorough assessment of different configurations can be executed in a flexible and efficient manner. The choice of modelling technique is based on the problem setting and the expected computation times for different CAE models. Based on the control coefficients for a localized warning signal targeted at different angles with respect to the forward direction of travel, a verification study of the spatial distribution of the acoustic pressure was performed. Finally it was demonstrated that also the design of an internal warning system for the driver can be designed using CAE tools, in particular Ray Tracing methods.

4F.5 References

- [6] D. Quinn, J. Garcia, J. Mitchell, P. Clark, "eVADER : the development and evaluation results of a next-generation pedestrian alert solution for quiet electric vehicles", Fisita World Automotive Congress 2014 (Maastricht, the Netherlands, June 2-6 ,2014
- [7] J. J. García , J. M. Barrios , D. Quinn , G. Baudet ,T. Schmit , J. Chamard, "The expected impact of eVADER technology on the safety of vulnerable road users", Proc. ISMA 2014, Noise and Vibration Conference (Leuven, Belgium, 15-17 September 2014
- [8] H. Van der Auweraer, D. Sabbatini, E. Sana, K. Janssens, "Analysis of Electric Vehicle Noise in View of VRU Safety", in Proceedings ICSV18, Brazil, 10-14 July 2011
- [9] Van Genechten B., Vansant K. & Berkhoff A.P., Simulation-based design of a steerable acoustic warning device to increase (H)EV detectability while reducing urban noise pollution In Proceedings of the TRA 2014, Paris, France, 14-17 April 2014
- [10]R. Hallez, K. De Langhe, "Solving large industrial acoustic models with the fast multipole method", Proc. ICSV 16, Krakow (Poland), 2009
- [11]K. Vansant, R. Hallez, K. De Langhe, H. Bériot, G. Massa, S. Donders, H. Van der Auweraer, "Simulating acoustic engine performance over a broad frequency range", SAE Paper 2011-26-0019, Proc. SIAT 2011, Pune, India, Jan. 19-21, 2011
- [12]Gumerov N.A. and Duraiswami R., Fast Multipole Methods for the Helmholtz equation in three dimensions, Elsevier Science, 2005
- [13]Hackbusch, W., "A sparse matrix arithmetic based on H-matrices. Part I: introduction to H-matrices", Computing, 62(2):89–108, 1999.
- [14]Bérenger, J., "A perfectly matched layer for the absorption of electromagnetic waves", Journal of Computational Physics, 114:157–171, 1994
- [10] LMS Virtual.Lab Rev 12
- [11] J.F. Hamet and M. Bérengier, "Acoustical characteristics of porous pavements: a new phenomenological model," Proc. Internoise 93 (Leuven, Belgium) 641-646 (1993)

Annex 4G

Damage detection in the inertial dampers of the electrical vehicle using experimental modal identification

Calin Itu¹, Paul Nicolae Borza¹, Maria Luminita Scutaru¹, Consuelo Gragera Pena²,
Sofia Sanchez Mateo³, Sorin Vlase¹

¹ TRANSILVANIA University of Braşov, Romania

² Extremadura University, Badahoz, Spain

³ Mechanical Engineering and Energy Department, Miguel Hernandez University of Elche, Av de la Universidad, S/N - 03202, Elche, Spain,

4G.1 Introduction

Inertial dampers ensure, through the structural design, mechanical energy dissipation due to vibration or noise generating source. Also these dampers allow, as result of vibration energy dissipation in volume of plastics on the one hand and as result of dissipative higher power efficiency and stability on the other hand (due to the high energy absorption distributed system) the use of corresponding nonlinear zone flexibility based plastics. Moreover, the spatial distribution of inertial masses ensure a more uniform thermal loading plastic base and can be achieved without breaking conditions thereby avoiding pregnancy and the development of concentrators zones in basic plastic. The same spatial distribution in conjunction with inertial masses form, their surface roughness and especially the flexibility of plastics allow obtaining anisotropic features extremely useful in terms of optimal adaptation in relation to the type of shock absorber damping designed for this task. In [11] such a solution is presented that allows vibration damping electronic control circuit due to the commutation of a stepper motor power. If evoked system consists of silicone plastic housed in a hermetic housing, and moving inertial masses is limited mechanically. If plastic studied system consists of a silicone housed in a hermetic housing and the motion of the inertial masses is limited mechanically.

In [1] are shown the theoretical equations of motion corresponding inertial mass immersed in basic plastic. In the paper [2] such dampers are included in the class of 'meta-materials', mechanical hybrid structures respectively (composite) that allow "predicting the mechanical properties of the design phase" and damping properties in relation to specific needs in system which the damper is included. Such systems are found in the living world that can fulfil both dissipation function but also amplification and therefore accelerations of vibration transmitted through the damper. These issues are extremely important in case of electric vehicles, as a result their shareholders through either the power of synchronous motors or asynchronous motors with the control based on the electric commutation circuit occurring two categories of sources of vibration or noise frequency bands with two distinct areas. First, lower,

corresponding to the fundamental frequency applied to the electric motor that is dependent on variable angular speed.

The second frequency range of vibration is due to electrical switchgear and circuit characteristics and correspond to higher frequencies such as those produced by electrical switching circuit. This second field will vary very little in relation to the angular speed of the engine or the velocity of the vehicle. This second area is intended to be covered by the damping characteristics (band pass filter) that can perform inertial damper.

Alternative solutions, involving the development of an annulator of oscillations in electric commutation type Wiener filter [8], which both in terms of reliability, energy consumption, especially high computing power necessary to implement satisfy only partially the needs of applications involving a rotating as uniform for electric vehicle drive system. The Wiener filter operation is based on fundamental control signal adding an estimated signal so that the resulting signal at the output compensate the vibrations due to the commutation electric power applied to the electric motor. The use of a computer system in real time requires high computing power or specialized circuits but also requires a certain energy and so strictly administered in case of an electric vehicle. Furthermore, if for some reason practically disappears the power control system of the torsional vibration, disappears too the possibility to decrease the vibrations.

4G.2 Mechanical model and analysis scenarios

In Fig 1-G a standard model of an inertial damper is presented. The damper is made by rubber reinforced with balls. In the paper two cases are considered: the balls are made by steel and, alternately, by aluminium (Al). The results are similar, which is why we only present the case where steel balls are. The properties for rubber and steel are those currently used in engineering.

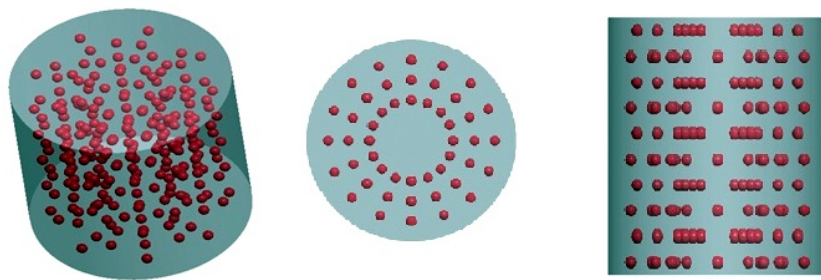


Fig. 1-G. Physical model of the inertial damper

A finite element model for the damper is presented in Fig.2-G. The main goal of the paper is to determine the eigenvalues for a functional structure and for the damaged

structure. Making an analysis in the Eigen frequencies changes is possible to identify the moment when the damage is produced. The method was presented in previous paper as [3],[4],[7]. Analytical methods in the field of the eigenvalues can be found in many paper (see [5],[6]).

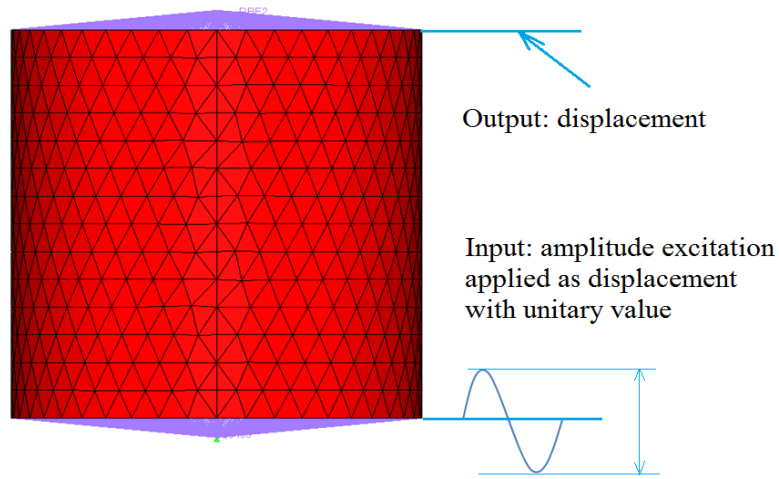


Fig. 2-G.. Finite element model of the damper

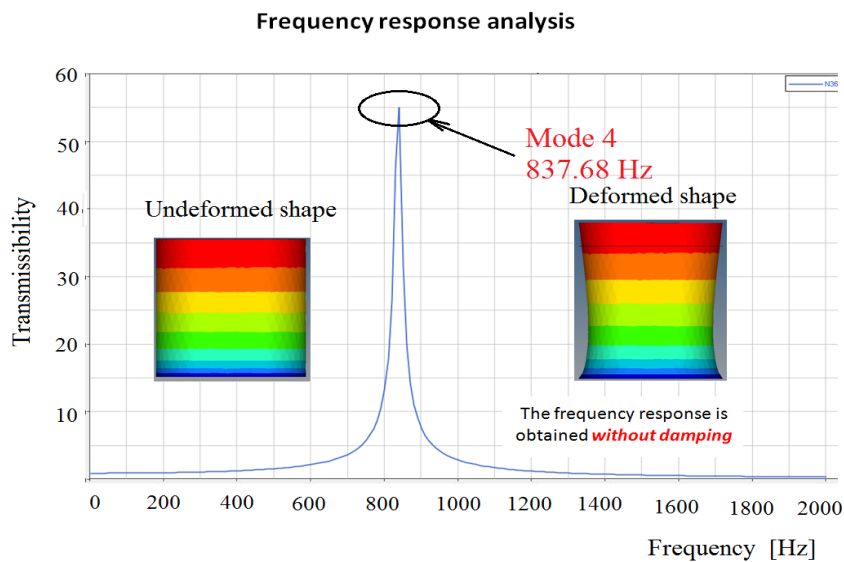


Fig. 3-G. Frequency response for a rubber model

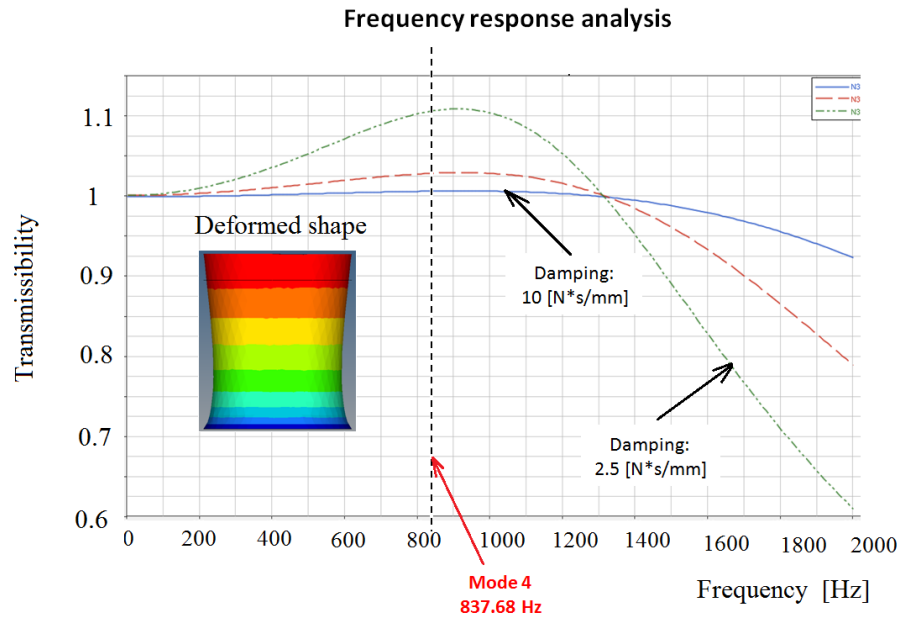


Fig. 4-G. Frequency response for an inertial damper with steel balls

Scenarios of analysis – Height zone of damage from ground

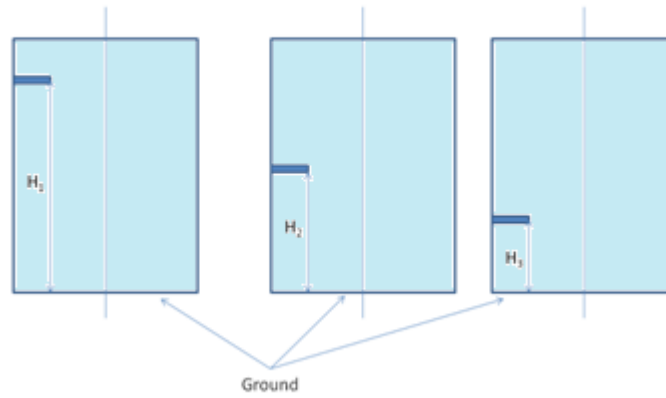


Fig. 5-G. Damage scenarios for the damper

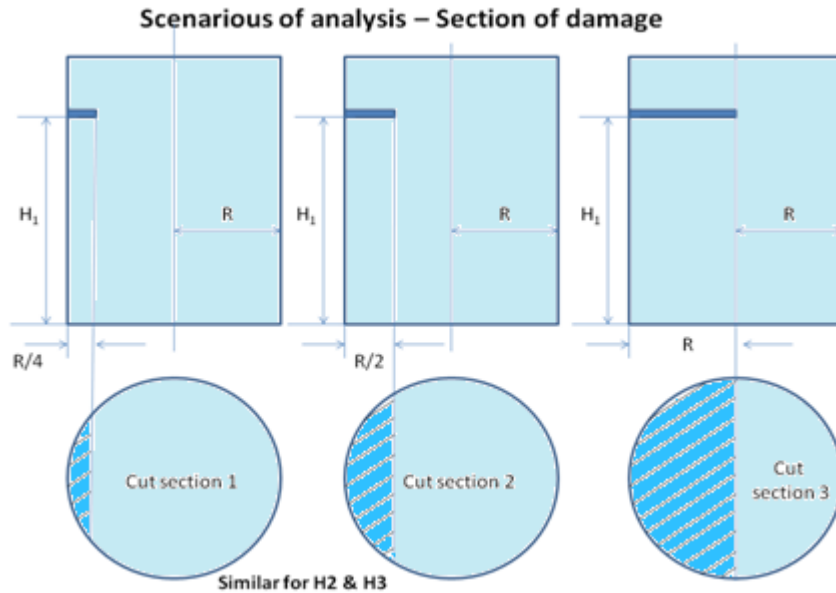


Fig. 6-G. Damage scenarios for the damper

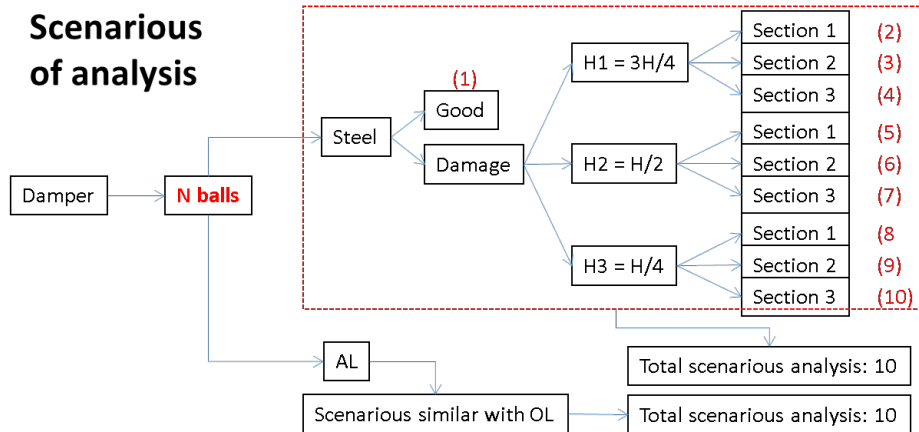


Fig. 7-G. Scenarios of analysis

4G.2 Eigenvalues for the damaged damper

The eigenvalues and eigen modes were computed using a finite element soft. The result for the eigenvalues computed for the scenarios presented in Fig. 7-G are presented in Table 1-G.

Table 1.G. Eigenvalues for the first 10 scenarios

Mode no.	Frequency [Hz]									
	Good (1)	D1 (2)	D2 (3)	D3 (4)	D4 (5)	D5 (6)	D6 (7)	D7 (8)	D8 (9)	D9 (10)
1	320	320	320	305	318	302	212	312	280	170
2	320	321	321	311	320	310	243	318	305	223
3	459	460	458	437	456	438	383	451	427	349
4	837	835	814	554	824	711	461	822	730	500
5	879	874	859	727	860	852	711	863	835	671
6	879	876	864	843	880	858	844	872	854	803
7	1379	1356	1245	934	1366	1270	1009	1381	1383	1375
8	1559	1541	1460	1140	1547	1487	1232	1559	1555	1495
9	1560	1554	1519	1289	1562	1515	1369	1561	1560	1505
10	1600	1600	1588	1382	1602	1590	1548	1600	1592	1570

A representation of the first ten eigenvalues for the scenarios considered is made in the Fig. 8-G to Fig. 12-G.

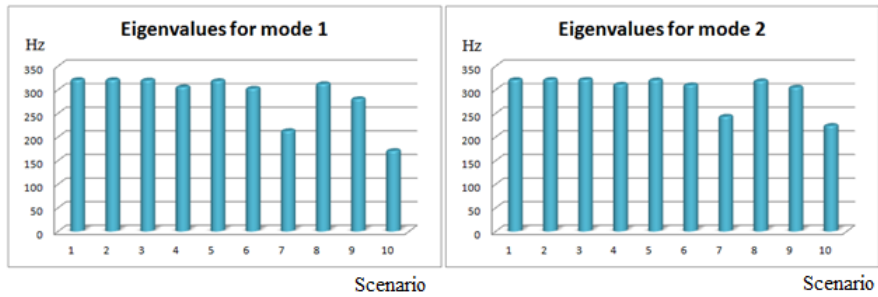


Fig. 8-G. The first two eigenvalues for the ten scenarios

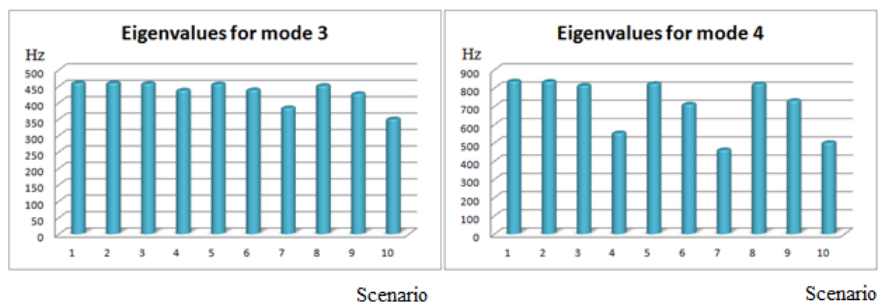


Fig. 9-G. The 3rd and 4th eigenvalues for the ten scenarios

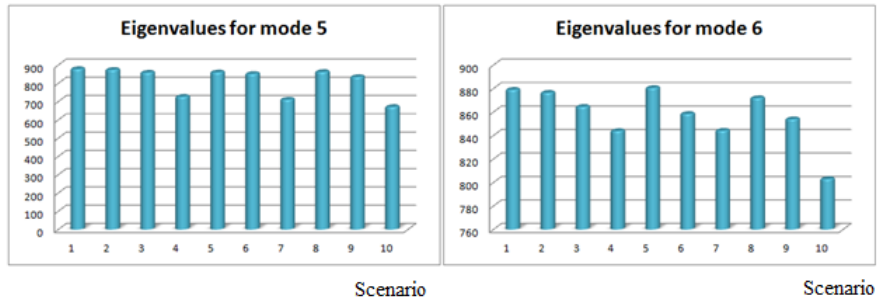


Fig. 10-G. The 5th and 6th eigenvalues for the ten scenarios

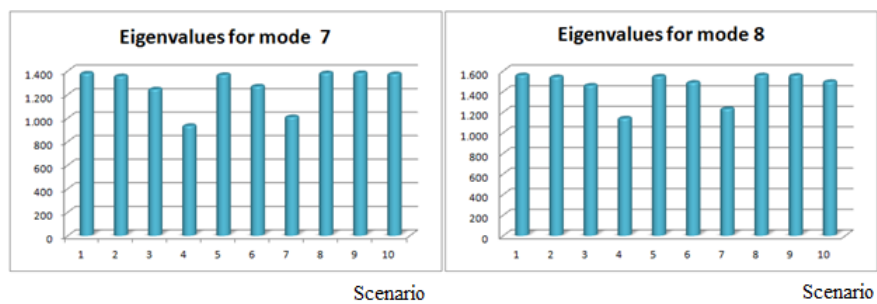


Fig. 11-G. The 7th and 8th eigenvalues for the ten scenarios

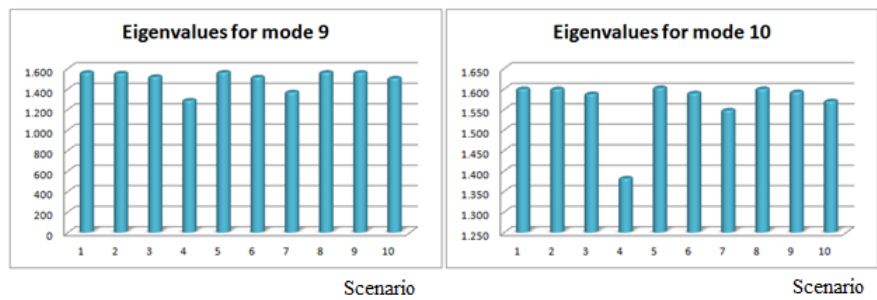


Fig. 12-G. The 9th and 10th eigenvalues for the ten scenarios

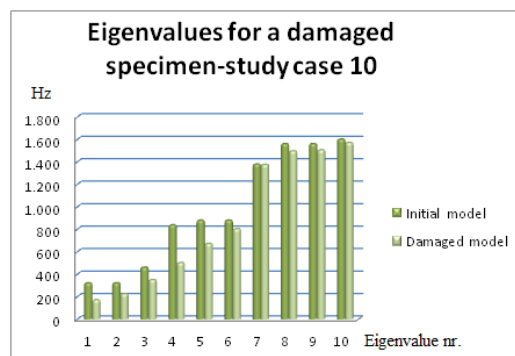


Fig. 13-G. The first 10 eigenvalues for the scenario nr. 10 (initial and damaged model)

Symmetric modes gives equal eigenvalues [9], [10] but a crack in the material makes one of the eigen modes to keep his value while the other will change. That is why it is necessary to consider various eigen modes each time to make comparison. Some eigenvalues, despite the emergence of crack and damage of the damper, do not change (it can compare, for example, line 1 and 2 of Table 1-G).

If we analyse one of the cases, for example, the last case (version 10 – Fig. 13-G) you can see that the eigen mode 7, for example, is not changed although the case study shows a consistent fissure. In contrast to most other eigenvalues are severely affected. It will result so that some eigenvalues are not altered by a change in material continuity while others give some consistent differences. It follows therefore that for detecting a beginning of damage is necessary to consider several vibration modes to be comparable to the initial situation.

Table 2-G. Eigenvalues for the next 10 scenarios (balls made of aluminium)

Mode no.	Frequency [Hz]									
	Good (11)	D1 (12)	D2 (13)	D3 (14)	D4 (15)	D5 (16)	D6 (17)	D7 (18)	D8 (19)	D9 (20)
1	327	327	326	312	325	309	217	318	286	174
2	327	328	328	317	326	316	248	325	311	228
3	467	467	465	445	464	446	390	459	434	356
4	855	853	831	565	841	725	471	839	745	511
5	895	891	876	741	877	870	725	879	851	684
6	895	893	881	861	897	875	861	888	871	819
7	1401	1379	1265	951	1389	1291	1029	1404	1406	1398
8	1592	1574	1489	1164	1579	1516	1258	1592	1588	1526
9	1592	1587	1550	1315	1594	1546	1394	1594	1593	1536
10	1634	1634	1621	1408	1637	1624	1580	1634	1626	1605

When we use balls made by aluminium the results are presented in Table 2-G. The conclusions analysing the values presented in Table 2-G offer similar conclusions as for the values presented in Table 2-G, from a qualitative point of view. The density of aluminium being smaller as the density for steel, the quantitative results differ.

4G.3. Conclusions

In the operation of a vibration damper, insert mode of the balls inertial in the mass damper rubber makes it vulnerable to damage. It is, of course, be very useful to detect early failures of this damper before damage. It can thus avoid significant material expenses. A periodic visual inspection requires expenses and waste of time. For this reason it can be very useful to find a method of early detection of cracks in the rubber body. In this paper we propose the use of their eigen frequencies damper measurement and comparison to baseline. If there are significant differences the damper may be replaced. As seen in the presented figures, some eigen frequencies can differ more or less, depending on the place and dimension of the fissure. For this reason, multiple frequencies should be analysed and compared simultaneously. We must not confine ourselves to the study of a single frequency of failure because there may be cases where the eigen frequency corresponding to a particular mode of vibration, not be influenced by the mechanism of destruction, but other frequencies are affected.

The analysis was carried out for a single shock absorber, attached at one end. In practice it may be more useful to consider the damper mounted in the mechanical system. This arrangement makes its eigen frequencies of the damper to change. They can be determined from a more complex calculus but the findings of this study do not change. From the results presented it can be concluded that a change of eigen frequency more than 5% can pull the alarm on the possibility of cracks in the structure while a difference of more than 10% should lead to a revision of the whole assembly to determine the cause of this change.

4G.4 References

- [1].Carotti,A., Turci,E., A tuning criterion for the inertial tuned damper. Design using phasors in the Argand–Gauss plane. *Applied Mathematical Modelling*, 23(3), 199–217, 1999.
- [2].Claeys,C. C., Pluymers,B., Sas,P., Desmet,W., Design of a resonant metamaterial based acoustic enclosure, *Proceedings of ISMA2014*, 3351–3358, 2014.
- [3].Gillich,G.-R., Praisach,Z.-I., Iavornic,C.M., Reliable method to detect and assess damages in beams based on frequency changes. *ASME 2012 International Design Engineering Technical Conferences and Computers and Information in Engineering Conference*. pp. 129-137, 2012.
- [4].Gillich,G.-R., Praisach,Z.-I., Damage-patterns-based method to locate discontinuities in beams. *SPIE Smart Structures and Materials - Nondestructive Evaluation and Health Monitoring*. 869532-8, 2013.
- [5].Neubert, V.H., Design of Damping and Control Matrices by Modification of Eigenvalues and Eigenvectors, *Shock and Vibration*, Volume 1, Issue 4, Pages 317-329, 1994.

- [6].Nobari, A.S., Ewins, D.J., On the Effectiveness of Using Only Eigenvalues in Structural Model Updating Problems, Shock and Vibration, Volume 1, Issue 4, Pages 339-348, 1994.
- [7].Praisach,Z.-I., Gillich,G.-R., Birdeanu,D.E., Considerations on natural frequency changes in damaged cantilever beams using FEM. International Conference on Engineering Mechanics, Structures, Engineering Geology, International Conference on Geography and Geology-Proceedings. pp. 214-219, 2010.
- [8].Shimkin,N., Estimation and Identification in Dynamical Systems. Israel Institute of Technology, Department of Electrical Engineering, Lecture Notes, 2009, Chapter 3, Fall 2009.
- [9].Vlase,S., Danasel,C., Scutaru,M.L., Mihalcica,M., Finite Element Analysis of a Two- Dimensional Linear Elastic Systems with a Plane "Rigid Motion", Romanian Journal of Physics; 59(5-6), 2014.
- [10]. Vlase,S., Teodorescu,P.P., Itu,C., Scutaru,M.L., Elasto-Dynamics of a Solid with a General "Rigid" Motion Using FEM Model. Part II. Analysis of a Double Cardan Joint. Romanian Journal of Physics, 58 (7-8), 2013.
- [11]. ***, "Inertial Damper for Stepper Motor" Focus, I. (2012). Dmp 20 / 29 / 37, 42. Phytron Corp. see on www.phytron.com/DMP April 2015.